CONTINUOUS FREE-FLOW ELECTROPHORESIS AND SCANNING ELECTROCHEMICAL MICROSCOPY INVESTIGATIONS OF MONOLAYER-PROTECTED NANOCLUSTERS

By

Rachel Peterson

Dissertation

Submitted to the Faculty of the

Graduate School of Vanderbilt University

in partial fulfillment of the requirements

for the degree of

DOCTOR OF PHILOSOPHY

in

Chemistry

May, 2006

Nashville, Tennessee

Approved:

David E. Cliffel

Sandra J. Rosenthal

David Wright

David M. Hercules

G. Kane Jennings

To My Family

For all of their love and support.

ACKNOWLEDGMENTS

I would like to give thanks to my advisor, Dr. David Cliffel, for opening up the world of electrochemistry to me. I would also like to thank the members of my committee for their guidance in the development of my research. This work would not have been possible without the financial support of the Graduate Assistance in Areas of National Need (GAANN) program of the U.S. Department of Education, the Vanderbilt Institute for Nanoscale Science and Engineering, and the Vanderbilt Chemistry Department. In addition, I would like to thank the Boeing Company for the donation of intellectual property and financial support.

I am grateful for all those with whom I have had the opportunity to work with; Dr. Sven Eklund for his patience in answering my innumerable questions and for helping to develop my understanding of analytical chemistry; Dr. Madalina Ciobanu for her invaluable advice and patience both in the world of chemistry and life; and the rest of the Cliffel group for giving me the experience of working with them. I would like to give a special thanks to David Richman, recently retired from the Boeing Company, whose help made the construction of the novel electrophoresis instrument possible; to John Fellenstein and Robert Patchin who not only gave much needed advice during the construction of the instrument, but also brightened my day during each visit; and to Wes Hymer and Jill Welsh of Alpha Two for the use of their CFE instrument which made the fractionation of MPCs a reality.

TABLE OF CONTENTS

Page

LIST OF FIGURES

LIST OF TABLES

LIST OF SYMBOLS

Roman Symbols

Symbol	Meaning	Usual Units	Section
A	Area of an electrode	cm^2	4.2.1
a	Tip or UME radius	cm	4.3.2
C	Capacitance	F	3.3.1
C_O^*	Bulk concentration of the oxidized species	M, mol cm^{-3}	4.2.1
$C_O(0,t)$	Concentration of oxidized species at the surface of an electrode at time t	M, mol cm^{-3}	4.2.2
C_R^*	Bulk concentration of the reduced species	M, mol cm^{-3}	4.2.2
$C_R(0,t)$	Concentration of reduced species at the surface of an electrode at time t	M, mol cm^{-3}	4.2.2
d	Thiol chain length	nm	3.3.1
E	Energy	J	3.3.1
E	Electrode potential	V, mV	4.2.2
$E^{0'}$	Formal potential of the system	V, mV	4.2.2
E_{eq}	Equilibrium potential of an electrode	V, mV	4.2.4
e	Electronic Charge	C	3.3.1
F	Faraday's constant (9.65×10^4)	C	*4.2.1*
f	F/RT (38.92)	V^{-1}	4.2.3
$\Delta G_f^\dagger$	Activation energy for reduction of the oxidized species	kJ mol^{-1}	4.2.5
I_T	Normalized tip current (i_l/i_{ss})	-	4.3.2

Symbol	Meaning	Usual Units	Section
$I_T(L)$	Diffusion-limited tip current at a normalized tip/substrate separation (L)	-	4.3.2
$I_{T(ll)}$	Dimensionless current from mass transfer and kinetically limited current	-	4.3.3
i	Current	A	4.2.1
i_0	Exchange current	A	4.2.4
i_a	Anodic current	A	4.2.2
i_c	Cathodic current	A	4.2.2
i_{exp}	Parallel combination of mass transfer and kinetically limited current	A	4.3.3
i_k	Kinetically limited current	A	4.3.2
i_l	Limiting current	A	4.2.1
$i_{l(ll)}$	Limiting current from mass transfer and kinetically limited current	A	4.3.3
i_{ss}	Steady state current	A	4.3.2
$i_{ss(ll)}$	Steady state current from mass transfer and kinetically limited current	A	4.3.3
$K_{P,O}$	Precursor equilibrium constant for the oxidized species	-	4.2.5
k^0	Standard heterogeneous rate constant	s^{-1}	4.2.3
k_B	Boltzmann's Constant (1.38×10^{-23})	$J\ K^{-1}$	3.3.1
k_b	Backward heterogeneous rate constant	$cm\ s^{-1}$	4.2.2
k_f	Forward heterogeneous rate constant	$cm\ s^{-1}$	4.2.2
L	Normalized distance (d/a)	-	4.3.2
m_O	Mass transfer coefficient for the oxidized species	$cm\ s^{-1}$	4.2.1

Symbol	Meaning	Usual Units	Section
m_{ss}	Mass transfer coefficient for steady state	cm s^{-1}	4.3.2
n	Number of electrons transferred	-	3.3.1
O	Oxidized species	-	4.2.2
Q	Total charge	C	3.3.1
Q_0	Charge of an electron	C	6.1
R	Reduced species	-	4.2.2
R	Gas constant	J mol^{-1} K^{-1}	4.2.2
r	Inner metal radius of an MPC	cm	3.3.1
T	Temperature	K	3.3.1
t	Time	s	4.4.1
V	Voltage	V, mV	3.3.1
v_n	Nuclear frequency factor	-	4.2.5
	Greek Symbols		
α	Transfer coefficient	-	4.2.3
β	Distance factor for extended charge transfer	$Å^{-1}$	4.2.5
δ	Diffusion layer thickness	cm	4.4.1
ε	Dielectric constant	-	3.3.1
ε_0	Permittivity of free space	C^2 N^{-1} m^{-2}	3.3.1
κ_{el}	Transmission coefficient	-	4.2.5
κ_{el}^0	Standard transmission coefficient	-	4.2.5
η	Overpotential, E-E_{eq}	V	4.2.4

Symbol	Meaning	Usual Units	Section
μ_{ep}	Electrophoretic mobility	$cm^2\ V^{-1}\ s^{-1}$	6.1
υ_f	Forward rate	$mol\ cm^{-2}\ s^{-1}$	4.2.2
υ_b	Backward rate	$mol\ cm^{-2}\ s^{-1}$	4.2.2
υ_{net}	Net rate	$mol\ cm^{-2}\ s^{-1}$	4.2.2

CHAPTER I

INTRODUCTION

1.1 Purpose of Research

The purpose of this research is to characterize monolayer-protected clusters (MPCs) for possible use in nanoelectronics or nanoelectrochemistry. The limits of conventional silicon-based electronics have spurred researchers to work on developing alternatives such as nano- or molecular electronics for use in nanodevices. MPCs, whose kinetically controlled synthesis always results in a distribution of particle sizes, were isolated into more monodisperse samples and their electron transfer characteristics were investigated for use in nanoelectronics.

1.2 Nanotechnology

Recently, a concentrated focus on the development of nanotechnology has arisen due to their many potential applications including biosensors, drug delivery agents, and electronics. Nanomaterials are unique in that they are between molecules and bulk materials in size endowing them with distinctive properties. The nanomaterials used in nanotechnology need to have at least one dimension between one and 100 nanometers, be designed via a process which controls the chemical and physical properties of the structures, and be combined to form larger structures.[1,2] This dissertation investigates the fractionation and characterization of MPCs for the future use in nanotechnology.

1.2.1 Nanobiotechnology

Nanobiotechnology is one focus for the use of nanomaterials. The development of a method of molecular detection using reconfigurable arrays and label-less molecular recognition via several different nanomaterials including nanowires, nanocapacitors, and quantum dots are a few of the objectives of nanobiotechnology. A long-term goal of nanobiotechnology is the construction of *in vivo* nano-sized biosenors that could be used to continuously monitor a specific analyte such as hydrogen peroxide, glucose, or DNA in the body. Eventually, nanobiotechnology also may allow the realization of a synthetic biological cell. In fact, nanomaterials are currently finding a real use in biological applications. The Quantum Dot Corporation currently employs Qdot nanocrystals, which have unique optical properties, as bio-labels for a variety of applications such as multiprotien analysis, protein and DNA labeling, and live cell labeling. Nanomaterials such as nano-scale zinc oxide have also been used as additives to improve the basic properties of products such as sunscreen.[1-4]

1.2.2 Nanoelectronics

The emerging field of nanoelectronics is believed to be a natural replacement for silicon electronics when their limit is realized. The use of molecules and nanomaterials as electronics elements is particularly promising due to their size, which are 2-3 orders of magnitude smaller than the current state of the art for silicon-based electronics allowing a theoretical data density of 10^4 to 10^6 times what is currently possible. In order to realize nanoelectronics, the methods must be developed to fabricate the nanostructures and to construct electrical contacts.[5,6]

1.2.2.1 Top-Down Fabrication of Nanostructures

One of the major limitations to the development of nanoelectronics is the ability to fabricate structures as small as 10 nm. Researchers have investigated several top-down methods to fabricate nanostructures in which a pattern or structure is first generated and then reduced in size to form nanostructures.[7] Photolithography, which is currently used to mass manufacture transistors for electronics, is currently limited to ~100 nm features. Technical problems make this technique very expensive. The use of electron beam lithography, shown to be successful in writing lines only a few nanometers thick in photoresist on a silicon substrate, requires the fabrication of each structure a line at a time making it a very slow and costly process.[7,8]

The use of mechanical processes rather than light and electrons has also been investigated to build the nanostructures. Microcontact printing and micromolding in capillaries, two promising methods that employ a polydimethylsiloxane (PDMS) stamp formed using soft lithography, have been shown to form structures as small as 50 nm. While these methods require no special handling and can be performed on a bench top, any distortion of the PDMS stamp leads to a misalignment of the layers and renders the structure useless.[7,8]

Nanoimprint lithography, a fast method that is suited for large-scale fabrication, has resulted in structures as small as 20 nm. Some difficulties have been observed in forming structures with both micro- and nanoscale features. Dip pen lithography, which uses an atomic force microscope (AFM) "inked" with a thiol monolayer, has been developed in order to write nanometer-sized lines. While this technique is relatively slow, it is very versatile due to the wide variety of "inks" that can be used.[7,8]

1.2.2.2 Bottom-Up Fabrication of Nanostructures

Researchers have also investigated bottom-up methods that employ individual atoms and molecules as the building blocks of nanostructures. The goal of the bottom-up methodology is to develop nanostructures employing components such as quantum dots, nanoparticles, and nanotubes.[7] The bottom-up method has resulted in the fabrication of magnetic recording materials, interconnects in ultra large-scale integrated devices, energy storage devices, and chip based biosensors via alloys.[9] Biotin functionalized nanotubes have been linked to streptavidin-coated gold nanoparticles, demonstrating their ability to form hybridized structures suitable for nanoelectronics.[10]

Transistors, a basic building block of electronics, are switches that can turn on or off an electric current and amplify signals.[11] It has been shown that clusters of molecules approximately 0.5 nm wide are capable of behaving as on/off switches that can stay "on" for up to 10 mins. Regrettably, the conductivity difference between the on and off positions of these clustered molecules is only a fraction of that achieved in transistors currently used in electronics.[12] Organically passivated nanoparticles (3 to 23 atoms) have been demonstrated to be capable of functioning as a single-electron transistor at room temperature when applied as a Langmuir-Blodgett film on highly oriented pyrolytic graphite.[13] Carbon nanotubes have been shown to operate as transistors, transistor interconnections, and can be used to form diodes. Unfortunately, it is difficult to produce uniformly sized nanotubes and a small change in the size of a nanotubes can be the difference between forming a conductor or semi-conductor. A semiconductor nanowire, whose size can be directly controlled and is similar in size to a carbon nanotube, has been used to construct transistors, inverters, light-emitting diodes, and memory devices.[11]

It is currently impossible to scale traditional charge storage devices to the dimensions required for nanoelectronics. A proprietary prototype molecular-silicon hybrid DRAM device has been developed which has a memory storage capacity of 1 Mbit. The construction of the molecular-silicon hybrid device uses less than 10% of the number of steps required in commercial DRAM devices.[14] The Langmuir-Blodgett deposition of organically passivated nanoparticles (10 nm) incorporated into a charge storage device was reported. The formation of the metal-nanoparticle-semiconductor device, via silicon/silicon oxide and cadmium arachidate, resulted in voltage dependent hysteresis attributed to the storage of charge by the device.[15]

A novel molecular rectifier, which converts alternating current to direct current, has been constructed using hexadecylquinolinium tricyanoquinodimethyanide, 2,6-di[dibutylamino phenylvinyl-1-butylpyridinium iodide, and dimethylanilinoaza[C_{60}]fullerene sandwiched between the same two metal electrodes (aluminum and gold) on both sides. These rectifiers showed a decrease in rectification upon repeated voltage scans. The optimum rectification ratio observed was 27.53 at 2.2 V via hexadecylquinolinium tricyanoquinodimethyanide sandwiched between two gold electrodes.[16]

1.2.2.3 Molecular Electrical Contacts

While the construction of the individual devices required for nanoelectronics is challenging, the integration and interconnection of the devices has proven even more difficult. Additionally, leads or interconnections to establish electrical contact must be attached to each end of the components of nanoelectronics in order to study their

characteristics. There have been several different approaches for this including the use of molecules and nanowires to form the contacts.[11,17]

Scanning tunneling microscopy (STM) and AFM have been employed to make electrical contact with a single molecule; unfortunately, it is impossible to determine the number of molecules contacted and the method of the contact.[6,17-20] Additionally, many different measurements of the same molecule using these methods have resulted in widely different results; for example, deoxyribonucleic acid has been shown to be an insulator,[21] semiconductor,[22] metal,[23] and superconductor.[24]

Recently, triphenyl phosphate passivated gold nanoparticles (1.5 nm in diameter) were used to provide a metal contact to a SAM for AFM microscopy. The study encountered problems attributed to the movement of thiols on the gold surface and the solvation of the thiols, which can carry the gold atoms from the substrate with them. Another approach to form interconnections involves the development of a nano-scale gap between two electrodes followed by the insertion of a molecule into the gap. The formation of the gap is often time consuming and requires sophisticated fabrication facilities yielding only a few functional devises.[25] Therefore, there is still much that needs to be understood and developed before nanoelectronics can be realized.

It has been shown that molecular junctions, which can act as interconnections, have exhibited current rectification, conductance switching, and bistable memory behavior.[16,26] The use of SAMs, Langmuir-Blodgett monolayers, and carbon nanotubes have been investigated as molecular electronic junctions. While the use of single molecules or groups of molecules as electronic junctions is promising, currently electron transfer characteristics are difficult to define and control over distances longer than that

of tunneling and shorter than bulk materials. It has been shown that nanowires can be assembled as two-dimensional arrays via fluid flows. This method has resulted in the formation of diodes from the nanowires.[11,16]

1.3 Monolayer-Protected Nanoclusters

The research presented in this dissertation is concerned with the fractionation and characterization of MPCs for their use in the bottom-up method of fabrication for nanotechnology. MPCs are of interest as nanostructures in nanoelectronics via bottom-up method of fabrication. MPCs have become the focus of academic and industrial interest due to their unique optical,[27-34] electronic,[35-39] and electrochemical properties.[40-46] MPCs are nanometer-sized metallic cores protected by a monolayer of passivating thiols allowing the nanoparticles to be soluble, air stable and very robust, making them facile to handle.[44,47,48] They are also easily derivatized and do not irreversibly aggregate upon repeated dissolution. Due to the distinctive architecture of the MPCs consisting of a monolayer of thiols protecting an inner metallic core as shown in Figure 1.1, MPCs act as soluble nanocapacitors and therefore have the potential to be used as capacitors in the emerging field of nano- or molecular electronics.[49] MPCs have been applied to surfaces and layered to form ordered three-dimensional superlattices which exhibit there own optical, electronic, and electrochemical characteristics.[30,40,50,51] The unique properties of MPCs lend wide variety of possible uses for the nanoparticles in areas other than nanoelectronics such as fuel cell catalysts, thin films, drug delivery agents, and molecular markers.[47,49,52-54]

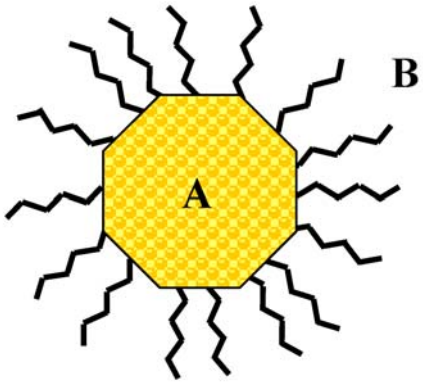

Figure 1.1 Diagram of a gold MPC. A) Inner gold core. B) Outer passivating thiol monolayer which electrically insulates the inner core.

The combination of self-assembly techniques with classic metal colloid chemistry produces the thiol covered metallic MPCs. The ability of thiols to form self assembled monolayers (SAMs) on gold surfaces was well known when Brust *et al.* first demonstrated the reduction of $HAuCl_4$ by dodecanethiol and $NaBH_4$ to produce polydisperse thiol protected gold MPCs as follows:[42,47]

$$AuCl_4^-{}_{(tol)} + 3RSH_{(tol)} \rightarrow (-Au^+SR-)_{n(tol)} + 4HCl_{(tol)} + RS\text{-}SR_{(tol)} \quad (1.1)$$

$$(-Au^+SR-)_{n(tol)} + BH_4^-{}_{(aq)} \rightarrow Au_x(SR)_{y(tol)}. \quad (1.2)$$

While there were other successful attempts at producing nanometer-sized particles, the method developed by Brust was very easy and resulted in stable particles of 1-5 nm in diameter.

The initial nanoparticle synthesis was quickly followed by the utilization of other metals such as copper,[55] silver,[34] palladium,[37] platinum,[56] and alloys[57] to form the MPC's inner core. Additionally, a variety of thiols were investigated to passivate the nanoparticles.[47,58-60] It was found that the terminating functional group of the thiol monolayer dictated the solubility and functionality of the MPC formed. The use of

organic soluble thiols result in organic soluble MPCs, while the use of thiols terminated in polar groups result in water soluble MPCs. Additionally, it was shown that the functionality of the nanoparticles can be easily manipulated through a place exchange reaction with a free thiol.[61]

1.4 Electron Transfer Properties of MPCs

1.4.1 Thermodynamic Electron Transfer Properties

As stated previously, MPCs have several unique properties that permit them many possible applications including nanoelectronics. It was predicted by Alivisatos in 1996 that metal nanoparticles with a diameter of 1-10 nm would have physical properties that were not that of bulk metals or of small molecules but instead dependent upon the particles size, shape, and protecting group.[62] The ability of MPCs to transfer electrons into and out of the inner metallic core and to store charge has proven valuable.

The capacity of MPCs to store charge was demonstrated in Murray's group by observing quantized double layer (QDL) charging peaks.[43] QDL charging is used to describe the double layer charging of the MPC nanocapacitors resulting from the passage of one electron at a time into or out of the core of the nanoparticle. QDL charging is observed as distinct charging peaks in voltammograms, analogous to the reduction and oxidation of single molecules. Therefore, simple electrochemical techniques such as cyclic voltammetry and square wave voltammetry can be used to probe the electronic properties of these nanoparticles as shown in Figure 1.2. (Note: A more detailed explanation of QDL charging can be found in Chapter 3.4). While the observance of

QDL peaks allows the investigation of the thermodynamic properties of the MPC such as charging potentials and particle capacitance, the next avenue of investigation required before they can be implemented in any potential applications involves the determination of the kinetic properties of the MPC such as electron transfer rate.[63,64]

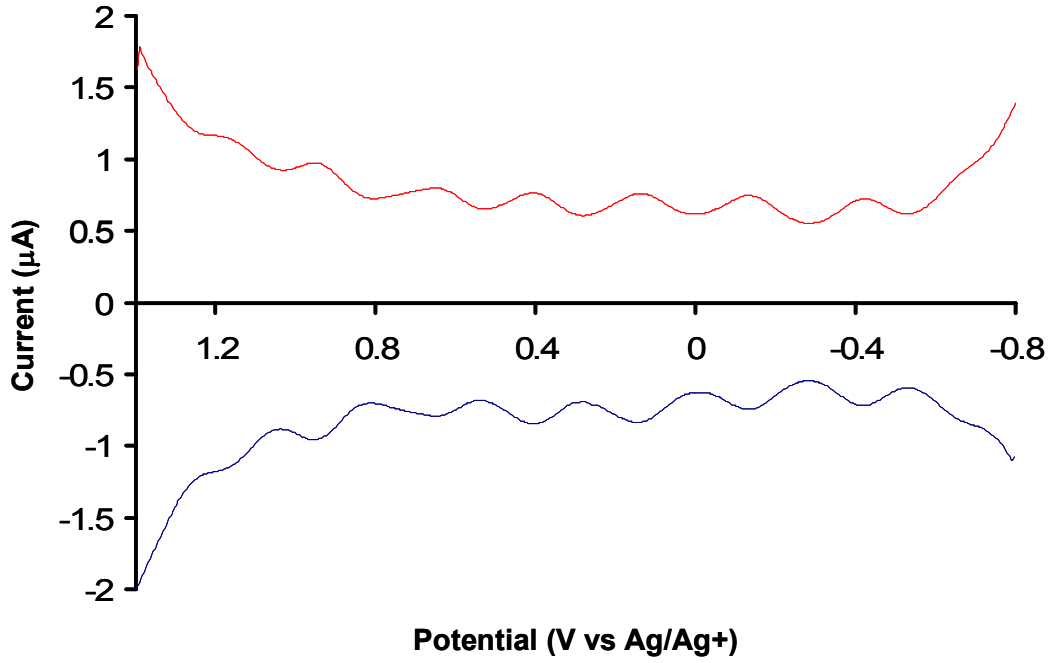

Figure 1.2 Example sweep wave voltammogram showing QDL charging. The peaks indicate the charging states or redox states of the MPC.

1.4.2 Electron Transfer Rate of Films of MPCs

The most successful methods used to measure the kinetic rate of electron transfer involve the formation of MPC films. The biomolecular electron transfer rate for various alkanethiol Au MPCs was found to be on the order of 10^8 to 10^{11} M^{-1} s^{-1}. This study was conducted by first drying MPC films on an interdigitated array (IDA). An example of an IDA is shown in Figure 1.3. Potential sweeps were conducted with the IDA fingers

acting as parallel plate working electrodes. This forced the electrons to travel through the nanoparticles in order to transfer the charge from one IDA finger to the next. The report also investigated the conductivity of MPCs protected with various thiol chain lengths and showed that the conductivity decreased exponentially as the chain length increased. This indicated that the electron transfer through the thiol monolayer of MPC occurred via tunneling.[39] This method was also employed to measure the electron hopping rate through arenethiolate (benzylthiolate, phenylethylthiolate, phenylbutanethiolate and cresolthiolate) MPC films. The electron hopping rate constants was found to range from 10^8 to 10^{11} s^{-1}. Once again the shorter thiols exhibited faster electron hopping. It was also observed that the arenethiolate MPCs had a slightly faster electron transfer rate than the alkanethiol nanoparticle with a passivating monolayer of similar length. While this technique for measuring MPC electron transfer rates is promising, it was found that the thickness of the nanoparticle film (~10-15 μm) was much more than the IDA finger height (0.1 μm) guaranteeing that then MPCs where not only positioned between but also above the fingers. At this time it is impossible to determine the effect of the MPCs above the gold IDA fingers on the measured rates.[65]

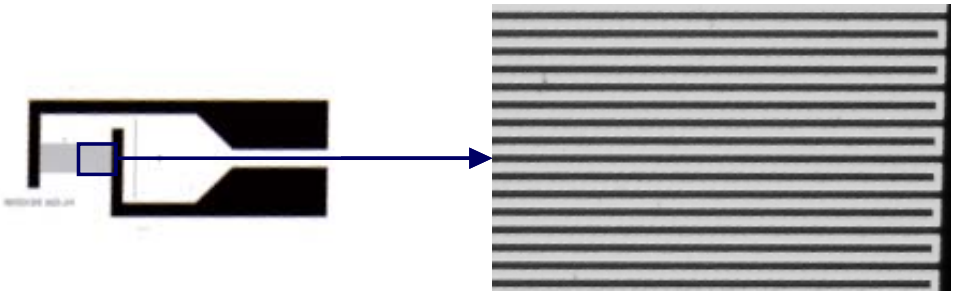

Figure 1.3 Picture of an interdigitized array (IDA) used in many MPC electron transfer studies.

The first order rate constant between MPCs, composed of mixed monolayers of hexanethiol and mercaptoundecanoic acid, in a multilayer film was investigated using potential step chronoamperometry and found to be on the order of 10^6 s^{-1}.[66] This method used a metal ion carboxylate linkage to form the MPC films. According to the authors, this rate is much larger than that previously shown. This rate corresponds better with an electron transfer through the 13 methylene units rather than the 22 present for the mercaptoundecanoic acid ligand. The mercaptoundecanoic acid group is not only long but also flexible. It is believed that the linking mercaptoundecanoic acid did not greatly contribute to the electron transfer due to the flexibility of the ligand. Therefore, at this time, it is not possible to determine the effect of this long linker chain on the rate of electron transfer. Additionally, it is also not possible to determine the effect of the metal ion linker on the rate of electron transfer.

MPC films were constructed by combining the use of metal ion carboxylate linkers and IDA electrodes to investigate the role of the length of the linking carboxylic acid terminated thiols and the non-linking alkane thiols on film conductivity.[67] The report demonstrated that the conductivity of the MPC film decreased as the length of the non-linking thiols increased. It also showed that the conductivity of the MPC film was influenced to a lesser degree by the length of the linking carboxylic acid terminated thiols. Therefore it was determined that the electron transfer is dominated by the non-linking thiols. The conductivity of the films was found to range from 10^{-7} to 10^{-4} Ω^{-1} cm^{-1}. The formation of the MPC films used in the previous studies was difficult to control. Once again, it is impossible to determine the effect of the MPCs oriented above

the gold IDA fingers on the measured rates. Therefore, a simpler method to determine the rate of electron transfer for the nanoparticles would be valuable.

Recently, the rate of electron hopping of MPC films, composed of MPCs with mixed monolayers of alkanethiol and mercaptoundecanoic acid or MPCs linked with dithiols, was investigated using steady state rotated disk electrode voltammetry.[68] The rate of electron hopping was found to be on the order of 10^5 s^{-1} which is much slower than previously demonstrated. Contrary to previous studies, faster electron transfer rates were not observed for shorter thiols. It was also found that thinner films exhibited slower kinetics. While this report was successful in showing that rotated disk electrode voltammetry could be used to measure MPC film kinetics, the degree of divergence of these results from previous studies indicates that the method requires optimizing. Again, the formation of the MPC films proved problematic; therefore, a simpler method of measuring MPC kinetics would be valuable.

1.4.3 Electron Transfer Rate of Single MPCs

It would be beneficial if the exact electron transfer rate could be determined for a single MPC. One method of accomplishing this could be scanning tunneling microscopy (STM). While STM has been used extensively to measure the electron transfer or tunneling through two dimensional self assembled monolayers (SAMs) of thiols, there has been little success with three dimensional MPCs due to the difficulty in depositing the MPCs and isolating a single nanoparticle for measurement.[69-72] Due to the wide variety in kinetic information available for MPCs, additional studies into their kinetics are required before they can be implemented into commercial applications. This

dissertation presents a better method of determining the MPC kinetic information using the scanning electrochemical microscope (SECM). The electron transfer rates were measured while in solution allowing a simpler experimental setup which is more easily controlled. Additionally, measuring the MPC kinetics in solution will avoid any possible effects of the film formation.

1.5 Scanning Electrochemical Microscopy

1.5.1 Brief Overview of the SECM

The SECM, developed by Bard in 1989, is an electrochemcial scanning probe microscopy technique that makes use of a four-electrode system controlled by a bipotentiostat. The SECM employs an ultramicroelectrode (UME) controlled by three piezoelectric motors, which move the tip in three dimensions enabling a raster scan of the tip across the substrate. This allows it to be a very versatile electrochemical tool that has been used extensively to measure the heterogeneous kinetic electron transfer properties at various interfaces.[73-76] More information on the SECM is given in Chapter 4.2.

1.5.2 SECM Studies of Liquid/Liquid Interfaces

SECM has been used extensively to investigate the kinetics of heterogenous electron transfer at the liquid/liquid interface of two immiscible electrolyte solutions. The heterogeneous electron transfer rate between neutral zinc porphyrin molecules in various organic solvents and aqueous redox species such as the negatively charged hexacyanoruthenate was measured at the liquid/liquid interface using SECM. It was

found that the rate constant was independent of the liquid/liquid interfacial potential difference when organic redox species was neutral. It was also found that the organic solvent used in the experiment affected the electron transfer rates they measured. The rate was three times faster with use of 1,2-dichlorethane instead of nitrobenzene due to a difference in dielectric constants and solvent relaxation effects.[77]

The rate of electron transfer between ferrocene in 1,2-dichloroethane and potassium ferricyanide in water across the liquid/liquid interface was determined to be between 0.23 cm/s and 0.00092 cm/s depending upon the potential applied to the UME and the ferrocene concentration.[78]

1.5.3 SECM Studies of Monolayers

SECM has also been used to measure the electron transfer properties of various monolayers. SECM was used to investigate the lateral diffusion and the kinetic electron transfer rate in Langmuir-Blodgett monolayers at an air/water interface through a triple potential step measurement. It was found that the 1:1 mixed monolayer of N-octadecylferrocenecarboxamide/1-octadecanol exhibited an electron transfer of 0.6 - 0.35 cm/s with the lateral diffusion of 10^{-1} x 10^{-7} cm^2/s depending upon the mean area per molecule. The electron transfer rate was inversely proportional to the lateral diffusion rate.[79]

The electron transfer properties of self-assembled monolayers (SAM) of ferrocene/alkanethiols on gold electrodes were measured using SECM under steady state conditions. The monolayers were formed by soaking gold substrate electrodes in a mixture of ferrocenyl-thiols and alkanethiols from 24 to 48 hours. The rate of electron

transfer between the underlying gold substrate and the ferrocene redox centers of the SAM was investigated. The contribution of the electron transfer from direct tunneling and electron transfer through defects (such as pinholes) was found to be 4.1 x 10^{-4} cm/s and 1.7 x 10^{-3} cm/s for SAMs composed of $FcCONH(CH_2)_{15}SH$/ $CH_3(CH_2)_{15}SH$ and $FcCONH(CH_2)_7SH/CH_3(CH_2)_8SH$, respectively, with the electrochemical mediators of $Ru(NH_3)_6Cl_3$ and $IrCl_6^{-3}$, respectively.[76] These rates are very close to the effective rate constants of 3.7 x 10^{-4} cm/s and 1.0 x 10^{-3} cm/s for the non-electroactive pentadecanethiol monolayer using $Ru(NH_3)_6Cl_3$ and $IrCl_6^{-3}$, respectively, as the electrochemical mediator. This indicates that the contributions of the direct electron tunneling and electron transfer through defects to the measured rate constant can be evaluated though analysis of the effective electron transfer rate at the corresponding non-active SAM. Additionally, the electron transfer between the redox active site of the SAM and the redox species in solution were evaluated. The bimolecular rate constant between bound ferrocene and $IrCl_6^{-3}$ was found to be 1.6 x 10^{10} mol^{-1} cm^3 s^{-1}. This report shows the versatility of the SECM in measuring electron transfer rates.

1.5.4 SECM Studies of Surfaces

The SECM was used to successfully investigate the heterogeneous electron transfer properties of a poly-(3,3”-didodecyl-2,2’:5’,2”-terthiophene) (poly (33”DDTT)) film. It was found that the electron exchange was localized to the polymer/solution interface rather than inside the polymer film. It was also determined that the electron transfer rate between the polymer film and the electrochemical mediator, methyl

viologen, is between 10^{-5} and 10^{-1} cm/s. This rate is dependent upon the film thickness, mediator concentration, and redox potential.[80]

The heterogeneous electron transfer at a nonconductive surface containing glucose oxidase was investigated using SECM. This method measured the current produced when the working electrode was at specific distance from the nonconductive surface to determine the kinetic information. Unfortunately, it is very difficult to calibrate the distance between the working and substrate electrodes. This difficulty resulted in uncertainty in the accuracy in the kinetic measurements.[81]

The platinum surface catalyzed electron-transfer hydrogen reduction from reduced N,N'-dimethyl-4,4'-bipyridinum, methyl viologen radical cation ($MV^{\bullet+}$) was analyzed using SECM. The solid/liquid interfacial analysis resulted in a rate of 3.7×10^{-5} cm/s.[82] Each of the SECM studies presented above prove that it is an excellent technique for measuring electron transfer rates and therefore could be used to measure the rate of electron transfer for MPCs.

1.5.5 Previous SECM Studies of Nanoparticles

The SECM has been used to investigate the electron transfer properties of nanoparticles at traditional metal-electrolyte and electrified liquid-liquid interfaces. Quinn *et al*. found that the traditional electron transfer rate, for the metal-electrolyte system, of hexanethiol passivated MPCs was very fast ($k > 0.1$ cm s^{-1}) with no difference in the response for different MPC charge states using a 10 μm UME.[83] In the liquid/liquid system it was expected that positively charged MPCs would exhibit an increase in current upon SECM approach to a reducing electrolyte in the aqueous phase

typical of an approach to a conductive substrate resulting from the interfacial reduction of the MPCs. Alternatively, the same was expected of negatively charged MPCs with an oxidizing electrolyte in the aqueous phase. The SECM approach in these systems did show an initial positive response followed by a decrease when the tip was close to the interface. It was determined that the liquid/liquid electron transfer is remarkably slow for hexanethiol MPCs ($k < 10^{-4}$ cm s^{-1}). It was rationalized that the slow heterogeneous rate is due to the large size and hydrophobicity of the MPCs, which resulted in a large separation between the MPCs and the aqueous electrolyte across the liquid/liquid interface.

The heterogeneous electron transfer rate of phenylethylthiol passivated MPCs was measured across a liquid/liquid interface. A commercial simulation package called FEMLAB was used in this analysis. The apparent biomolecular rate constant was found to be 76 M^{-1} cm s^{-1} using a 25 μm UME.[84]

1.5.6 Novel SECM Analysis of MPCs

Most of the SECM methods that have been employed to measure electron transfer rates involve the standard potential of the analyte,[76,78,82,84] concentration of the analyte,[76-79,82,84-88] complicated models,[84,85] multiple steps analyses,[79] or measurement at an interface.[76-79,82,84-87] MPCs typically have multiple oxidation states (~10) making the use of analysis techniques which rely upon the standard potential of the analyte impossible. As previously described, MPCs are polydisperse. The average diameter of MPCs is measured by transmission electron microscopy (TEM) while the ratio of metal to organic components is determined by thermogravimetric analysis (TGA). Due to difficulties in

measuring the average diameter accurately, the exact concentration of the MPCs cannot be completely relied on. Therefore, a method measuring the electron transfer rates of MPCs that does not rely on concentration would be invaluable. Additionally, the development of a simple method to measure the rate of electron transfer for MPCs which does not involve complicated models or multiple step analyses would be a very useful tool to researchers.

In this dissertation, a novel method to measure the rate of electron transfer through the thiol monolayer of MPCs using the feedback mode of SECM is described which does not involve standard potentials, concentration, the number of electrons transferred, complicated models, or multiple step analyses. The SECM electron transfer analysis involves only a solution of MPCs with a corresponding electrolyte eliminating the need for an interfacial measurement and therefore result in a simple and easy method to measure the electron transfer rates of MPCs.

1.6 SECM Mediated Imaging

1.6.1 Brief Overview of the SECM Imaging

The SECM has also found recent use in non-contact imaging of materials that have both conductive and nonconductive areas. For use in surface imaging, the SECM tip electrode approaches the substrate electrode along the z-axis while cycling a mediating redox species, as in the earlier ET studies. The tip electrode is then rastered across the surface of the substrate electrode in the x and y axes where the change in current is analyzed. An increase in the current is observed when a conductive area is

encountered while a decrease in current is observed when an insulating area is encountered.[73]

1.6.2 SECM Imaging of Surfaces

The SECM has been employed to image a variety of surfaces using a variety of redox mediators. The SECM was used to form well-defined patterns on a 2-dimensional monolayer of alkanethiols through electrochemical desorption. The pattern was then backfilled with a cystamine forming a pattern of amino-terminated molecules in the monolayer. Functional horseradish peroxidase enzyme was then covalently coupled to the cystamine molecules forming a pattern which was them imaged with the SECM using hydroxymethylferrocene as the redox mediator.[89]

Photolithography was used to attach photobiotin in micron-sized stripes on the surface of a carbon electrode. This was followed by the attachment of flourophore-tagged avidin to the biotin sites. The SECM was used to differentiate between the derivatized and underivatized stripes on the carbon electrode using potassium ferricyanide as the redox mediator.[90]

More recently, SECM was used to image immobilized enzyme microstructures and their localized biochemical activity.[91] Quinohemoprotien alcohol dehydrogenase and PQQ-dependent glucose dehydrogenase were immobilized in the presence of poly(1-vinylimidazole) complexed with $[Os(4,4'\text{-dimethylbipyridine})_2Cl]^{+/2+}$. It was found that SECM, using potassium ferricyanide as the redox mediator, was an excellent tool to investigate and optimize the enzyme architectures for biosensor formation. It was also

found that the signal was proportional to the amount of enzyme immobilized indicating the technique could be used to quantitatively measure the response of the sensors.

The SECM has been used to image the directed adsorption of Photosystem I on to patterned surfaces on to self assembled monolayers on a gold electrode using (ferrocenylmethyl)trimethylammonium as the redox mediator.[92] Alternating methyl and hydroxyl terminated monolayers formed the pattern. The protein blocked electron transfer and therefore caused a decrease in current. It was proved that the methyl terminated monolayers inhibited adsorption while the hydroxyl terminated monolayers enabled adsorption through SECM imaging.

The localized corrosion and electron transfer characteristics of native oxide layers of type 304 stainless steel was studied using SECM.[93] The redox couple I^-/I_3^- was used as a mediator and allowed the sensitive detection of oxide breakdown events. In order to obtain temporal information on these events, a stationary microelectrode array was employed for the imaging. The microelectrode array used 100 microelectrodes spaced 400 μm apart in a square 10 X 10 array forming an array with the effective area of 16 mm^2. It was found that the SECM microelectode array successfully detected localized corrosion processes on the stainless steel surface.

1.6.3 SECM Imaging using MPCs as Novel Electrochemical Mediators

The mediating redox species used for SECM imaging typically must have a rapid, heterogeneous one-electron transfer at the tip electrode.[73,94] For homogenous electron transfer reactions the electron transfer rates must be fast. Because this is the only requirement, there appears to be no advantage in using MPCs rather than typical redox

mediators for SECM imaging. MPCs in fact do have the advantage of being electrochemically active over a wide range of potentials (~-1 to 1.5 V vs. Ag/AgCl). In addition, MPCs can be synthesized to be soluble in either organic or aqueous solvents that will allow them to be able to used to image almost any type of material. Additionally, Williams *et al*. has used various metal complexes with a wide variety of sizes to image meso- and microporous materials.[95] MPCs are ideally suited to this type of imaging because MPCs have similar electron transfer rates and can range from 1 to 10 nm which is a much larger range than the mesoporous complexes used.

Current SECM imaging requires the selection of a mediator based on its potential and solubility. Therefore, the use of MPCs as redox mediators for SECM imaging allows the user more freedom and would be perfectly suited to use when the selection of a mediator is difficult due to the potential or solubility required. This dissertation proves the use of MPCs as novel electrochemical mediators for SECM imaging.

1.7 MPC Particle Dispersity

As stated previously, MPCs have several unique properties, resulting from the quantum mechanical effects of their limited size (2-5 nm), which permit them to have many potential applications. Before MPCs can be applied in technology, their properties must be thoroughly understood. Unfortunately, the kinetically controlled self-assembly always results in a distribution of MPC sizes instead of well-defined molecular compositions.[33,39] As a result, the synthesis and isolation of monodisperse nanoparticles is required for tuning their quantum-confined properties. The ultimate synthetic challenge is the creation of nanoparticles such as MPCs that have an exact molecular

formula, *i.e.*, they are completely monodisperse. The monodisperse particles are expected to have exactly the same optical absorbance, electrical capacitance, and electron transfer properties. Thus, the isolation of monodisperse MPCs would allow a better understanding of the properties of the particles. After these properties are rationally controlled, the MPCs can be applied to their various potential applications.

There have been several attempts to obtain monodisperse MPCs. Some general trends have been observed by varying the thiol to gold molar ratio, temperature, and rate of the addition of the reductant.[33,96,97] Thiol to gold ratios greater than 2:1 produced MPCs core diameters smaller than ~1.6 nm. Cooling the reactants before addition of the reducing agent causes slightly smaller MPC particle diameters and smaller particle dispersity. Smaller reducing agent to gold ratios result in increased MPC particle size. Finally, addition of the reducing agent quickly produced MPCs that are smaller and more monodisperse. Other methods such as heating,[98] etching,[99] and annealing[100] have yielded specific monodisperse samples, but have not demonstrated a wide range of size control of monodisperse MPCs.

Various isolation methods have also been tested to separate polydisperse nanoparticles into smaller size distributions. These isolation methods include solvent fractionation,[43,101] size exclusion liquid chromatography,[102] high-performance liquid chromatography (HPLC),[103,104] capillary electrophoresis (CE),[42] and gel electrophoresis.[105] Unfortunately, the methods that provide the greatest amount of isolated nanoparticles, namely solvent fractionation and column chromatography, have the least separation resolution, while those methods with the best fractionation into monodisperse sizes typically yield only small amounts of material. HPLC resulted in the

fractionation micrograms of MPCs per run while CE resulted in the fractionation of only nanograms of MPCs per run.[42,103,104] Larger quantities of a wider range of monodisperse MPCs would enable a direct correlation between MPC size and properties. This correlation must be elucidated before MPCs can be used effectively in the emerging fields of nano- or molecular electronics. This dissertation presents a better method of isolating monodisperse samples of MPCs.

CHAPTER II

EXPERIMENTAL PROCEDURES

2.1 Reagents

Dodecanethiol (C_{12}S-H, 98.5%+), hexanethiol (C_6S-H, 96%) were purchased from Acros, octanethiol (C_8S-H, 98.5+%), decanethiol (C_{10}S-H, 96%), 2-phenylethyl thiol ($Ph(CH_2)_2$S-H, 98%), N-(2-mercaptopropionyl)-glycine (tiopronin), L-γ-glutamyl-L-cysteinyl-glycine (glutathione), acetone, ethyl ether (ACS grade), toluene (ACS grade), and dithranol (97%) from Sigma®, acetonitrile (MeCN, 99%), methylene chloride (CH_2Cl_2, ACS grade), sodium nitrate ($NaNO_3$), sodium phosphate (monobasic NaH_2PO_4), sodium phosphate (dibasic, Na_2HPO_4), sodium borate (NaH_2BO_3), boric acid (H_3BO_3), sodium chloride (NaCl), and sodium borohydride ($NaBH_4$, 98+%) from Fisher, tetrabutyl ammonium hexafluorophosphate ($TBAPF_6$, ≥99%) and tetraoctylammonium bromide (TOABr, ≥98%) from Fluka, potassium hexafluorophosphate (KPF_6, 99%) from Aldrich, hexane (HPLC grade) from Burdick and Jackson, ferrocenylmethyltrimethylammonium iodide ($FcTMA^+I^-$) from Strem Chemicals, sulfuric acid (H_2SO_4, 95.0-98.0%) from EM Science, ethyl alcohol (200 proof) from AAPER Alcohol, and tris (crystallized free base, molecular biology grade) from Fisher Biotech. Tetrachloroauric acid ($HAuCl_4*3H_2O$) was prepared according to literature.[106] Ferrocenylmethyltrimethylammonium hexafluorophosphate ($FcTMA^+PF_6^-$) was prepared from ($FcTMA^+I^-$) according to the procedure given by Mirkin *et al*. using KPF_6 and N,N,N-Trimethyl(11-mercaptoundeceyl) ammonium chloride ([HSC11N+Me3][Cl-])

was prepared by the method described by Tien and coworkers.[107,108] Water was deionized using a Solution 2000^{TM} Water Purification system (≥ 18 MΩ). All chemicals were used as purchased unless otherwise specified.

2.2 MPC Synthesis

All MPCs were synthesized following previously published procedures.[33,48,58] A 3:1 ratio of thiol to $HAuCl_4$ and a 10:1 ratio of $NaBH_4$ to $HAuCl_4$ were used in the synthesis of all the MPCs. During the synthesis of alkanethiol MPCs, a phase transfer agent, tetraoctylammonium bromide (TOABr), was used to introduce the toluene insoluble $AuCl_4^-$ into the organic phase for reaction with protecting thiol. This gold-TOABr solution was typically stirred for up to 1 hour to ensure the complete transfer of $HAuCl_4$ to the toluene phase. Upon introduction of the thiol to the organic phase, the dark red solution became white to colorless. This reaction was thought to result from the reduction of the Au^{3+} to Au^+ with the formation of a polymer consisting of $[-Au^ISR-]_n$. This polymer solution was stirred up to 1 hour and then the solution was placed in an ice bath. The MPC solution was held at 0^oC during the addition of the reducing agent, $NaBH_4$, in a 10 fold excess which further reduced the Au^I to Au^0, forming the thiol protected gold MPCs. The MPC solution was stirred overnight before any impurities or unreacted thiols are removed. The synthesis of polar solvent soluble nanoparticles omitted the use of a phase transfer agent.[42,58] Each of the different water-soluble MPC syntheses resulted a different color change during the addition of the thiol.

The removal of impurities and unreacted thiol was facile.[33,58] After stirring overnight, the nanoparticle solution was rotovapped to near dryness. The organic soluble

MPCs were then sonicated in a solvent that they are not soluble in, such as acetonitrile, and allowed to sit until the MPCs settle out. The solvent was then decanted. The MPCs were placed on a glass frit filter and washing with copious amounts of solvents they were not soluble in, typically acetonitrile, acetone, and ethanol.

The polar solvent soluble MPCs were cleaned by dialysis in DI water over approximately 1 week. The water was changed at least 8 times during the dialysis of the nanoparticles. A 10,000 MWCO Spectra/Por® CE (Cellulose Ester) Membrane with a diameter of 10 mm was used for the nanoparticle dialysis.

The hexanethiol MPCs were separated into more monodisperse samples via solvent fractionation.[43] The nanoparticles were placed in acetone and allowed to sit for ~1 hr. The MPCs were then vacuum filtered using a glass frit. The MPCs which remained on the frit were completely insoluble in acetone indicating the nanoparticles were large. This fraction was named cut C. MPC solution was allowed to evaporate under the vacuum after the initial filtration. The acetone-MPC solution was then refiltered and the particles that remained on the frit, partially insoluble in acetone, were name cut B. The particles which remained in solution were named cut A and were soluble in acetone.

2.3 MPC Characterization

Proton nuclear magnetic resonance (^{1}H NMR) spectra were obtained from a Bruker Avance 300 MHz NMR to ensure the MPCs were free of impurities and unreacted thiol. The spectrometer was set to average 40 scans with a 5 second delay between

pulses. The spectra were taken at room temperature using the solvents D_2O, C_6D_6, or CD_2Cl_2 depending upon the MPC solubility.

UV-Visible spectra were obtained using on a Cary 100 Bio Spectrophotometer to determine the approximate size of the nanoparticles. The water soluble MPCs and organic soluble MPCs (in hexane) solutions were scanned from 200 to 800 nm using 1 cm quartz cells (Spectrocell).

Thermogravimetric analysis (TGA) was performed on a TA Instruments Hi-Res TGA2950 Thermogravimetric Analyzer using ~10 mg samples to obtain the metal to thiol ratio in the MPCs. Aluminum pans were heated from 25 to 550^{o}C at a rate of 15 ^{o}C/min under N_2.

A Philips CM20 200kV TEM was used to obtain TEM using a 300 mesh Formvar supported copper grid (Electron Microscopy Sciences) to determine the diameter of the MPCs. Dr. James Wittig of the Vanderbilt University School of Engineering calibrated the Philips CM20 TEM upon receiving the instrument and determined that it has maximum resolution of 0.29 nm. Samples were prepared by placing a drop of ~1 mg/mL water or toluene solution of the MPC onto copper grid. Water samples were then dried over night while toluene samples were dried for about 1 hr before the analysis was conducted. Images of at least 390K magnification were obtained. The TEM negatives were developed in house. The images were then scanned into Adobe Photoshop 5.5 using an Epson Perfection 1240u equipped with a film adapter. The images were then analyzed for the particle size distribution using Scion Image Beta Release 4.0.2 (www.scioncorp.com).

Matrix assisted laser desorption ionization mass spectrometry time of flight

(MALDI-TOF) spectra were obtained on a Voyager DE-STR (Perceptive Biosystems) to mass of the MPCs. The MALDI was set in positive and linear mode equipped with 337 nm nitrogen emitting laser with a 3 ns pulse width set at an intensity of 2700 while the pressure was kept to ~8 x 10^{-8} torr. An acceleration voltage of 25000 V was used with a grid voltage of 91.5%, a guide wire voltage of 0.20%, a delay time of 400 s, and a low mass gate of 5000.0 Da. The final spectrum obtained was an average of 200 separate scans with 300 point Savitsky-Golay smoothing. MPC samples used for MALDI were prepared by mixing a 5:2 solution of 30 mg/mL of Dithranol in CH_2Cl_2 and 10 mg/mL MPC. Samples were placed on a gold plated MALDI plate in 2 μL increments and allowed to evaporate for 2 hrs for CH_2Cl_2 samples and over night for water samples.

Multiple accelerating voltages, grid voltages, guide wire voltages, laser intensities were investigated. The low mass gate was also adjusted and both positive and negative modes were used. There was no difference in any of the spectra above the mass (m/z) of 20000. The water-soluble samples were also analyzed with a variety of matrices. 4-hydroxyazobenzene-2-carboxylic acid, αcyano-4-hydroxy cinnamic acid, 2′,4′,6′-trihydroxy acetophenone, 3-hydroxypicolinic acid and 9-aminoacridine were each tested. With the exception of 9-aminoacridin the matrices were dissolved in ethanol (~5 mg/mL and ~30 mg/mL). The sample (as stated previously) was spotted first and allowed to dry overnight. The matrix was then spotted and allowed to dry overnight. 9-aminoacridine (15 mg/mL) was mixed in a 2:5 ratio of the sample to matrix in methanol. The sample was also cospotted with 9-aminoacridine.

2.4 Electrochemical Analysis

2.4.1 Electrode Preparation

The tip electrodes used in this research were prepared in house following the instructions given previously for disk-in-glass UMEs.[109] A borosilicate glass capillary (2mm) was sealed on one end by heating it with a Bunsen burner. The micron-sized wire was then placed in the sealed capillary. The capillary was then placed under vacuum (Edwards, model RV8) and heated using an electric current across a coiled 22 gauge solid nichrome wire. Heating the capillary under vacuum caused the glass to collapse around the wire. A conductive silver epoxy (EPO-TEK® H2OE) was used to electrically connect the micron sized wire to a 24 gauge stranded wire. Dexter Hysol® Epoxi-Patch® Structural Adhesive was used to seal the glass capillary to the stranded wire. The UME was checked for electrical connection and then shaped, as shown in Figure 2.1, using 240 and 400 grit Carbimet® Paper Disks.

The UME and the substrate electrode where prepared by using successively 600 and 1200 grit Carbimet® Paper Disks. Solutions of 0.1 and 0.05 μm Micropolish II with 8" Microcloth on a Metaserv 2000 Grinder/Polisher (Buehler®) were used to polish the electrodes before use. Each electrode was examined for defects using an Olympus BX41 optical microscope. The electrodes were electrochemically cleaned using 0.5 M sulfuric acid following the procedure given by Bard and Faulkner before they were employed in the SECM studies.[110]

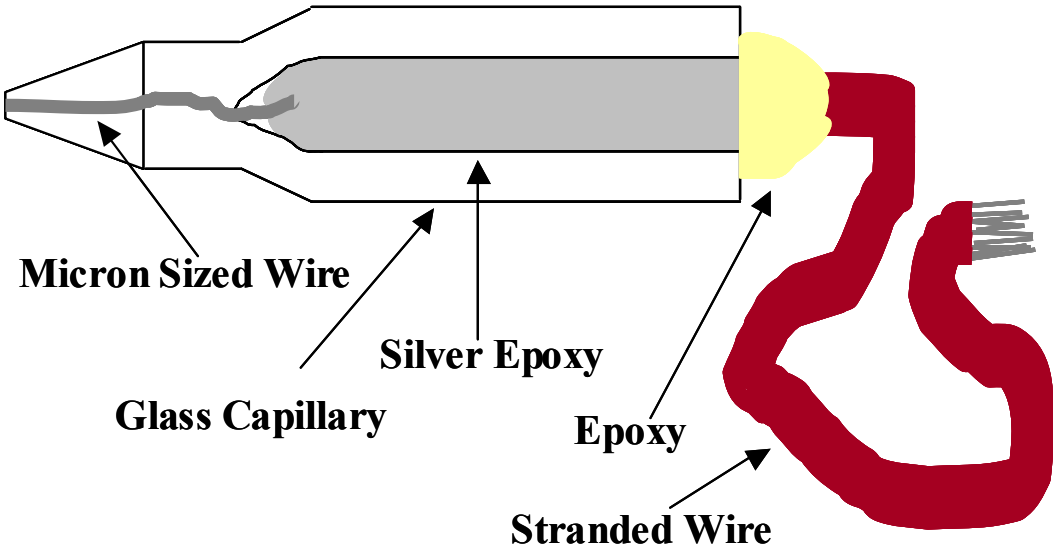

Figure 2.1 Diagram of a UME electrode constructed in house. The micron-sized wire enclosed in a glass capillary is connected to a stranded 24 gauge wire through the use of a conductive epoxy.

2.4.2 Electrochemcial Workstation

A CH Instruments 660a Electrochemical Workstation was used to conduct cyclic voltammograms and square wave voltammograms of the MPCs. The electrochemical cell consisted of a 2 mm diameter Pt working electrode with a Ag/AgCl aqueous or Ag/Ag^+ non-aqueous reference electrode and a Pt wire counter electrode. Samples were prepared by dissolving 20 mg of sample in 5 mL of 0.1 M $NaNO_3$ in 18 MΩ DI water, 5 mL of 0.1 M $TBAPF_6$ in CH_2Cl_2 depending on MPC solubility unless otherwise stated. The maximum scanning window for the cyclic voltammograms was 1.7 to –0.9 V with a scan rate of 100 mV/s or less. Sweep waves were conducted using the same scanning window as that given for the cyclic voltammograms with an increment of 0.004 V, amplitude of 50 mV, and a frequency 15 Hz.

2.4.3 SECM Workstation

A CH Instruments 900 Scanning Electrochemical Microscope (SECM) was used to complete the MPC approach curves. The electrochemical cell was made up of a 5 or 10 μm UME, a 2 mm Pt substrate electrode, a Ag/AgCl aqueous or Ag/Ag^+ non-aqueous reference electrode, and a Pt wire counter electrode. All approach curves were conducted inside a faraday cage (constructed in house).

Test approach curves were conducted on each of the UMEs using a solution of 1 mM $FcTMA^+PF_6^-$ in aqueous 0.1 M KCl to ensure they can achieve the required feedback currents for the MPC analysis. Each of the electrodes obtained 800% positive feedback current during the test approach curves. A cyclic voltamogram was also conducted in the previous solution to again ensure the tip was clean and free of contaminates.

The MPC solutions used in this analysis were prepared as described above. The approach curves of the MPCs the substrate electrode was approached using a step size of 0.5 μm or less, a withdraw distance of 20 μm or more, and a quiet time of 100 s or more. During the tiopronin studies, which employed a 5 μm UME, the solutions were filtered via a wadded kimwipe in a pasture pipette to remove any of the MPCs which fell out of solution. The pH dependent electron transfer studies were completed in buffered solutions. The typical 0.1 M $NaNO_3$ solution was used for pH 3, 0.1 M $NaCH_3CO_2$ buffer was used for pH 5, 0.1 M NaH_2PO_4 buffer was used for pH7, and 0.1 M NaH_2BO_3 buffer was used for pH 9. The electron transfer rate of each of the MPCs was calculated using the diffusion coefficient, D, of $(3.6 \pm 0.1) \times 10^{-6}$ cm^2/s.[39]

2.5 Continuous Free-Flow Electrophoresis

2.5.1 Fractionation

The continuous free-flow electrophoresis of tiopronin Au MPCs into monodisperse samples was conducted with a DeSaga CFE instrument at Alpha Two, a small analytical service company with experience in CFE methodologies for proteins. In the initial experiment (Method 1), the CFE was used to separate about 50 mg of tiopronin MPCs into 48 different outlet vials in ~1.5 hours. A 50 mM phosphate buffer of pH 7.0 which had a conductivity of 2660 μS was used with a flow of 3 mL/min. 50 mg/mL MPC sample was used at a flow rate of 0.75 mL/hour. The electrophoretic voltage was 120 V at a current of 250 mA. Of the 48 vials, 6 vials collected from the initial fractionation showed significantly colored samples indicating the presence of MPCs. In order to achieve a better fractionation of the MPC sample, some of the parameters were optimized (Method 2). The buffer was changed to 7.3 mM tris-borate of pH 8.7 which had a conductivity of 78 μS. The concentration of the tiopronin MPC sample was changed to 40 mg/ml. The electrophoresis voltage was 300 V at a current of 9 mA.

2.5.2 CFE Fractionated MPC Characterization

In order to determine the recovery of the fractionated MPCs, the collected vials of MPCs were dried and weighed. The mass of the salts from the buffer and the vials were then subtracted from this weight. The above-mentioned UV-visible spectrophotometer (scanned from 300 to 900 nm) was used to determine the approximate size of the nanoparticles. TEM was used again to determine the diameter of the fractionated MPCs.

While TEM is a very useful technique for measuring the sizes of larger particles, there was difficulty focusing on the MPCs that led to several blurred images that were not used in the analysis of the MPC particle diameter. The MPC samples examined by TEM were dialyzed for ~1 week before the analysis in order to limit aggregation of the MPCs. Even with dialysis, there was some agglomeration of the MPCs samples. These aggregates were not included in analysis for MPC particle diameter. The images were again developed in house, but the negatives were scanned in to the computer at 400% the original size, printed out, and measured with a ruler.

2.6 Novel CFE Instrument

306 stainless steel (purchased locally) was used for the construction of the novel CFE. The instrument was machined at the local Vanderbilt machine shop. Acrylic was used for the flow separator and as the bottom to the inner SS cone. Polycarbonate was used for the outlet box. Nalgene 180 PVC tubing with an inner diameter of 1/32″, outer diameter of 3/32″, and wall of 1/32″ was used for the sample inlet and outlets. Nalgene PVC tubing was also used for the buffer inlet. Falcon collection tubes were used to hold the outlet volume. Double sided adhesive (3M) placed between each of the rings to stick them together and to electrically insulate them. More details of the novel CFE construction can be found in Chapter 7.5.

A gear pump (model A-74014-00, Cole Parmer) was used to pump the buffer solution. A Kd Scientific Model 100 and a Harvard Apparatus PHD 2000 syringe pumps were used to inject the sample. A Sorensen DCS 33-33 power supply will be used. A Denver Instruments (model 250) pH, ISE, and conductivity meter equipped with a

Beckman Electrode pH probe (model 511052) and a Denver Instruments Conductivity/ATC probe with a 1 cm^{-1} cell constant was used to measure the pH and conductivity of the carrier and sample buffer. The pH probe was calibrated with standard buffer solutions of pH 4, 7, and 10 (Fisher Scientific) while the conductivity probe was calibrated with Traceable Conductivity Calibration Standards of 10.5, 100.1, and 1004 μS (Fisher Scientific).

An 8.9 mM tris-borate buffer was used as the carrier buffer in all the flow tests. The conductivity and pH of the buffer was measured before each flow test. A 25 mM 1,10 phenanthroline ferrous sulfate solution was used for all of the flow tests.

CHAPTER III

MPC SYNTHESIS AND CHARACTERIZATION

3.1 Introduction

The Cliffel group is investigating the use of multiple types of MPCs for a variety of purposes. Water-soluble platinum MPCs are being explored as chiral catalysts, while water-souble tiopronin passivated gold MPCs are being examined for the detection of the specific binding of an antibody to a synthetic peptide epitope, the active portion of an antigen. Additionally, the patterning of nanoparticles using capillary electrophoresis integrated with scanning electrochemical microscope is being investigated.

The research contained in this dissertation concerns the fractionation of tiopronin gold MPCs using the CFE and investigation of the electron transfer properties of both organic and water-soluble MPCs. Before the MPCs were used in this research they were characterized in order to determine their purity, particle size, and particle size distribution. Proton nuclear magnetic resonance spectroscopy (^{1}H NMR), UV-visible spectrophotometry, thermal gravimetric analysis (TGA), transmission electron microscopy (TEM), and matrix assisted laser desorption ionization mass spectrometry (MALDI-MS) were used to characterize the MPCs before any further research was conducted.[33,37,43,53,55,58,59,111,112]

3.2 MPC Characterization

3.2.1 Nuclear Magnetic Resonance Analysis

^{1}H NMR analysis was conducted on each MPC to insure that the sample was free of unreacted thiols, dithiols, and phase transfer agents and had a particle like structure.[33,37,38,43,53-55,58,59,112,113] Due to the large number of MPCs synthesized, only examples for each of the characterization methods will be provided. Typically, the ^{1}H NMR spectra of clean MPCs exhibit broad peaks that indicate the nanoparticles have very little or no remaining unreacted thiol, as shown in Figure 3.1. The peak broadening of MPC nanoparticles is a result of spin-spin T_2 broadening, surface defects, and inconsistencies such as vertices and holes in the metal core. Remaining unreacted thiols and impurities produce sharp NMR peaks, superimposed on the broad peaks, as shown in Figure 3.2. Each of the MPCs used in this research were shown to be free of unreacted thiol and impurities by demonstrating an NMR spectra similar to Figure 3.1.

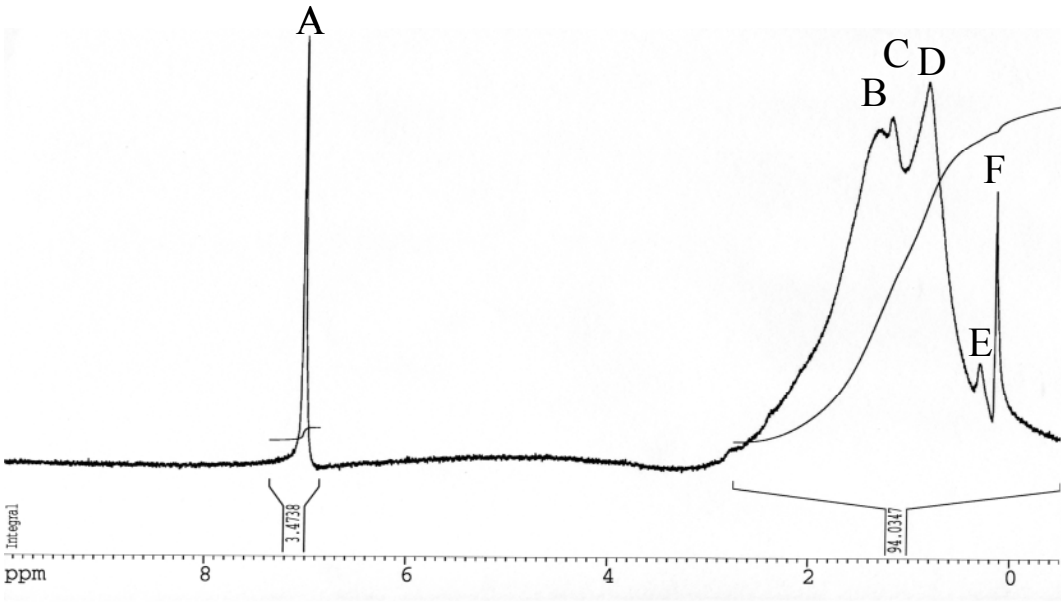

Figure 3.1 Proton NMR of clean hexanethiol Au MPCs (Cut C). The broad peaks indicate the nanoparticle is free of unreacted thiol. The peaks are labeled as follows A) C_6D_6, B), C), and D) CH_2 of hexanethiol E) CH_3 of hexanethiol and F) TMS.

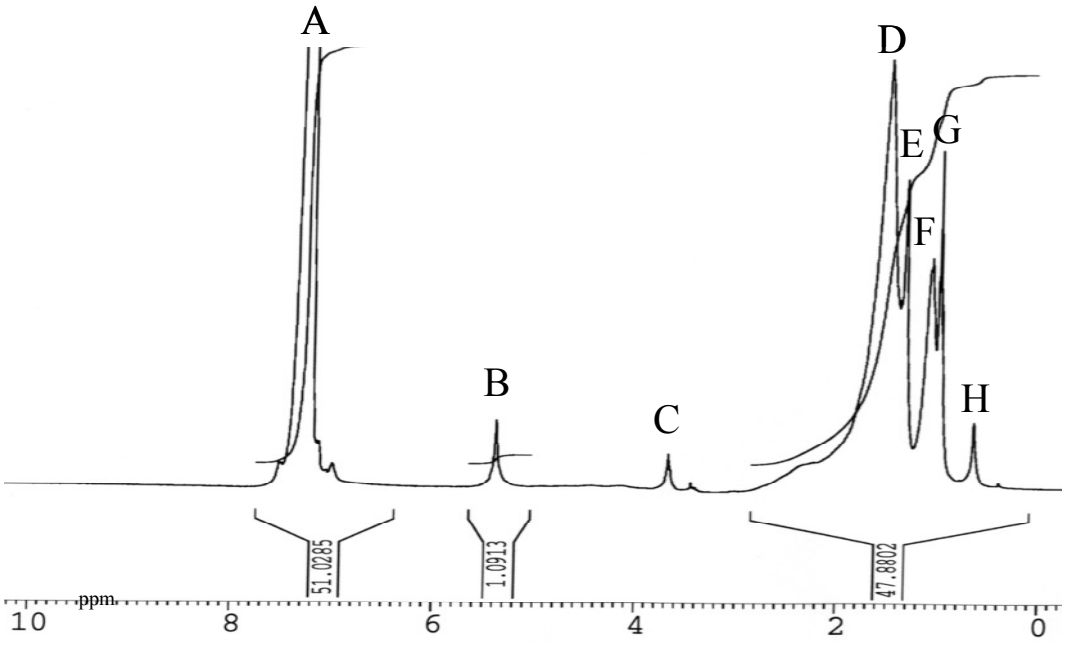

Figure 3.2 Proton NMR of unclean decanethiol Au MPCs. The sharp peaks indicate remaining unreacted thiol. The peaks are labeled as follows: A) C_6D_6, B) impurity from methylene chloride, C), E), and G) impurities from the phase transfer agent, D) and F) CH_2 of hexanethiol, E) also SH of unreacted hexanethiol, H) CH_3 of hexanethiol.

3.2.2 UV-visible Sepectrophotometry

The surface plasmon resonance (SPR) of nanoparticles, often examined with UV-vis spectrophotometry, is routinely used to determine the approximate diameter of the MPCs.[27,28,31,33,37,48,49,52,53,55,58,59,97,110-113] Mulvaney was one of the first and principal investigators into the surface plasmon resonance (SPR) of nanoscale materials.[114] In gold MPCs, the detection of an SPR absorbance peak at ~530 nm indicates a particle diameter larger than 2.5 nm. As the size of the MPCs decreases, the absorbance of the SPR band decreases with no visible SPR band for particles less than 2.5 nm. The electronic structure changes dramatically for the smaller MPCs and therefore the quantum size effect eliminates the SPR band.[27,33] Therefore, the observance of an SPR band indicates MPCs with a larger particle diameter, while the absence of an SPR band specifies MPCs with a smaller diameter.

As shown in Figure 3.3, the UV-Vis spectrum of N,N,N-Trimethyl(11-mercaptoundeceyl) ammonium thiol (TMA) MPC indicates that the MPC was larger than the other MPCs by its large peak at ~530 nm. The small peaks observed for hexanethiol cut C and octanethiol MPCs reveal that they are much smaller than the TMA MPC. The absence of any peak for the remaining MPCs indicates it had no surface plasmon absorbance and therefore had very small particle diameters. Hexanethiol MPCs (cut A and B) exhibited almost identical UV-vis spectra indicating that they are roughly the same size.

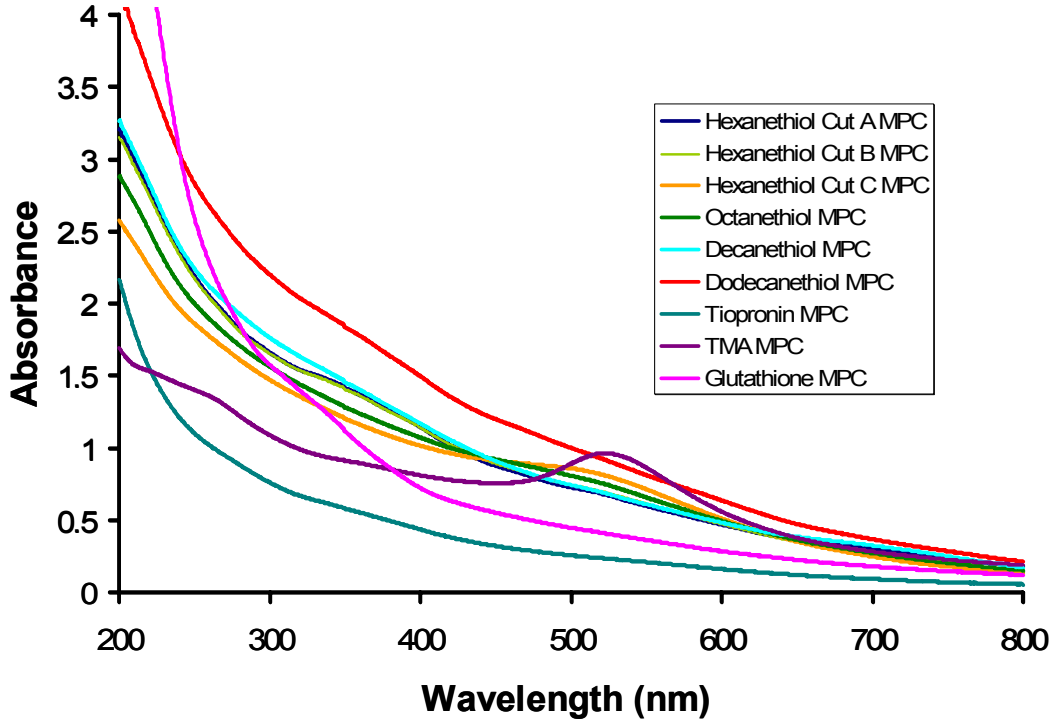

Figure 3.3 UV-visible spectra of the MPCs synthesized during this research. The peak at ~530 nm for the TMA MPC indicates it is a large nanoparticle.

3.2.3 Thermogravametric Analysis

The metal to thiol ratio is often determined using TGA which is needed to determine the approximate molecular mass of the MPC.[33,37,53,58,59] In TGA, the sample is heated while the mass of the sample is constantly monitored. The heat volatilizes the organic component of the MPCs and allows the percent of the MPC metal component to be determined as shown in Table 3.1. The metal to thiol ratio is then determine as follows

$$\text{Au} : \text{Thiol} = \frac{\text{GMW Thiol} * \% \text{ Gold}}{\text{GMW Gold} * \% \text{Thiol}}_{33} \qquad (3.1)$$

where GMW is gram molecular weight. This gold to thiol ratio was then used to determine the approximate number of gold atoms and thiol molecules via a chart given by

Hostetler *et al*. which has shown that MPCs cores form truncated octahedrons with preferred "magic number" populations. Higher gold to thiol ratios indicated a larger MPC particle.[33]

Table 3.1 TGA results for each of the MPCs synthesized. The percent ligand and gold was used to determine the approximate number of thiol chains and gold atoms. This allowed the approximate molecular weight to be found.

MPC	Ligand GMW	Weight %		Au:Ligand	# Thiol Chains (Approx.)*	# Gold Atoms (Approx.)*	MPC mass (Approx.) (kg/mol)
		Ligand	Gold				
C_6 – SAu Cut A	117.24	22.8	77.2	2.02	38	79	20.0
C_6 – SAu Cut B	117.24	20.7	79.3	2.28	53	116	29.1
C_6 – SAu Cut C	117.24	13.8	86.2	3.72	100	400	90.5
C_8 – SAu	145.38	20.4	79.6	2.88	71	201	49.9
C_{10} – SAu	173.35	25.3	74.7	2.60	53	140	36.8
C_{12} – SAu	201.4	29.8	70.2	2.41	53	140	38.2
PhC_2 – SAu	137.32	20.5	79.5	2.70	53	140	34.9
Tiopronin – SAu	162.2	24.9	75.1	2.48	53	140	36.2
Glutathione – SAu	306.33	32.7	67.3	3.20	92	225	72.5
$N^+(Me)_3(CH_2)_{11}$ – SAu	280.6	17.5	82.5	6.72	221	1289	315.9

The TGA of dodecanethiol MPCs, shown in Figure 3.4, gave a gold to thiol ratio of 2.41. This indicates the MPCs should have approximately 53 ligands and 140 gold atoms and a molecular weight of 38.2 kDa. The TGA of the TMA Au MPC gave a gold to thiol ratio of 6.72 demonstrating that the MPC is very large which is consistent with the UV-Vis data given above. This indicates that the TMA MPC should have approximately 221 TMA ligands and 1289 gold atoms for this MPC and results in an estimated molecular weight of 315.9 kDa which is consistent with the higher than average (1-2 nm) TEM diameter of 4.4 ± 1.6 nm reported by Cliffel *et al*. for the MPC.[52] The TGA analysis clearly shows a difference in the thiol to gold ratio for each of the different cuts of the hexanethiol MPC indicating that the MPCs were successfully

fractionated. It must be kept in mind that the TGA analysis only provides the MPCs average number of thiol and gold molecules. While it can indicate a general size for the MPC it does not specify the extent polydispersity. Before a better estimate of the molecular mass of the nanoparticle can be made, the diameter of the MPC must be found.

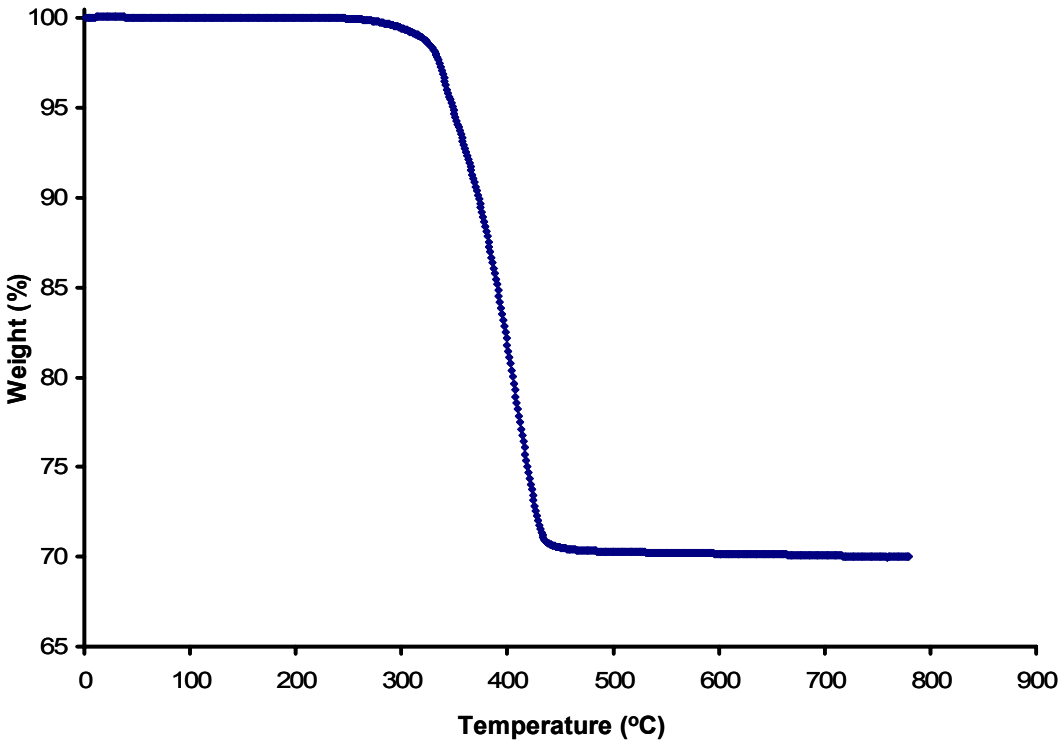

Figure 3.4 TGA analysis of dodecanethiol MPC in which the thiol percentage was found to be 29.8 %.

3.2.4 Transmission Electron Microscopy

TEM is commonly used to determine the diameter of MPCs.[33,37,43,48,53,55,58,59,111,115] In TEM, a focused beam of electrons is used to view and record the sample. While TEM is a very powerful tool for measuring sizes as small as 1 nm, its resolving power is ~0.3 nm.[116] Therefore, the direct measurement of the MPC

diameter is limited by the resolving power of the TEM. Once the diameter of the MPC and the percent metal and thiol is determined, the molecular mass of the particle can be found. The TEM images, such as that shown in Figure 3.5A, were used to determine the inner metallic core diameter of the nanoparticle as shown in the histogram in Figure 3.5B.

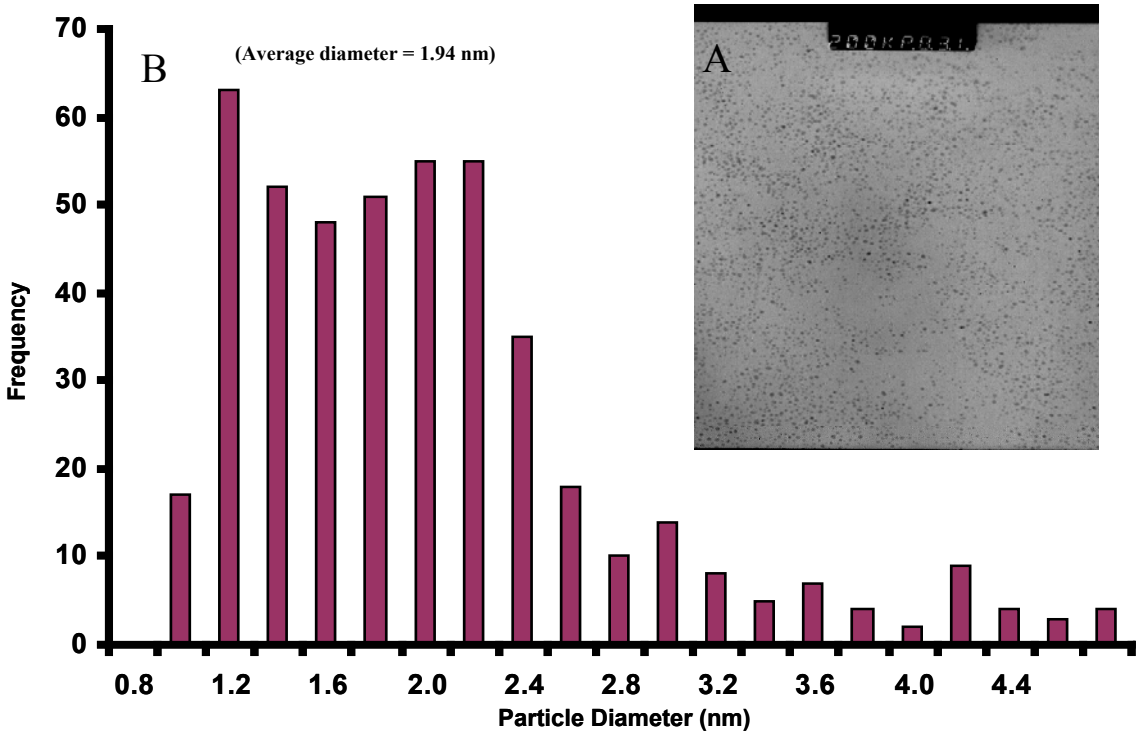

Figure 3.5 A) TEM image of hexanethiol Au MPCs. B) TEM histogram of hexanethiol Au MPCs with an average diamter of 1.94 ± 0.82 nm.

3.2.5 Matrix Assisted Laser Desorption Ionization Mass Spectrometry

MALDI-MS in the positive mode was used to determine the molecular weight of the gold MPCs synthesized.[29,43,111-113] While the TGA exhibited different thiol to gold ratios for the hexanethiol cut A and B MPCs, the MALDI spectra showed that the samples were not completely fractionated into two separate mass ranges as shown in Figure 3.6. The TGA analysis gave an expected molecular weight of 20 kDa for cut A

and an expected molecular weight of 29 k Da for cut B. The largest peak was around 30 kDa for the MALDI analysis. It was observed that cut A does have a higher concentration of the smaller particles as was expected from the TGA analysis. Therefore the TGA analysis cannot be relied upon for the determination of the molecular weight. The TEM analysis of the hexanethiol cut B MPCs had an average diameter of 1.94 nm which corresponds to an average molecular weight of 56 kDa which corresponds well with the peak at 60 kDa. This indicates that the peak at 30 kDa is the doubly charged particle. The MALDI spectra of hexanethiol cut C MPC only exhibited a single very small peak at a mass much lower than expected from the TGA analysis. The peak observed is believed to indicate a triply charged particle. Additionally, this signified that MALDI was unsuccessful at identifying the higher mass of the MPC.

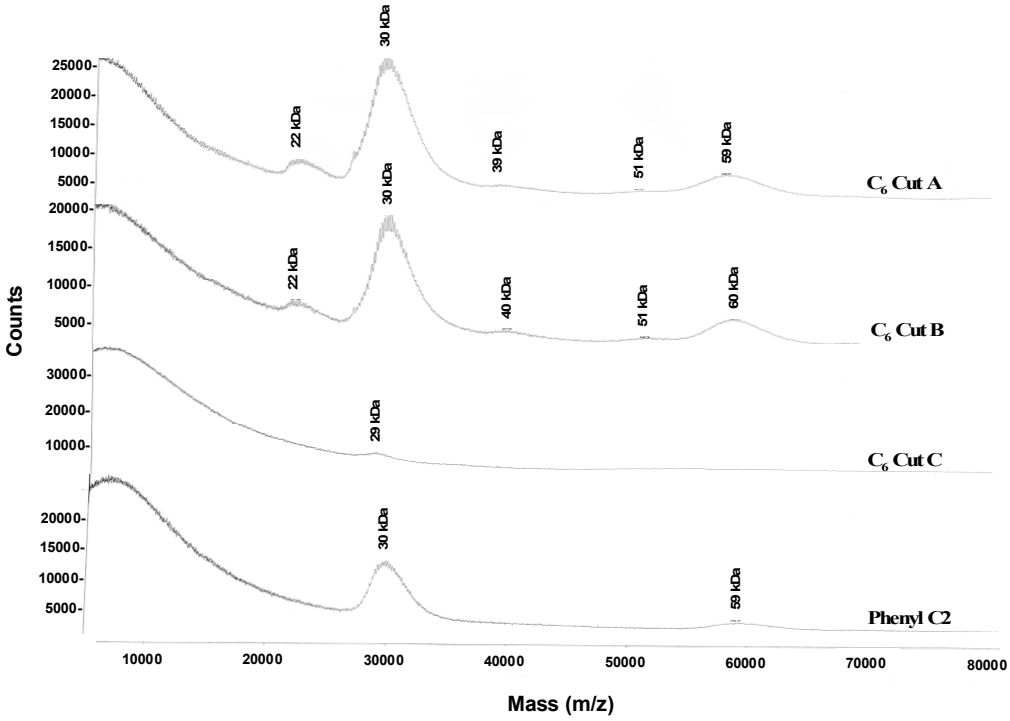

Figure 3.6 Smoothed MALDI spectra of the hexanethiol (Cut A), hexanethiol (Cut B), hexanethiol (Cut C), and 2-phenylethane thiol MPCs.

The spectra shown in Figure 3.6 were smoothed to remove the noise from the original spectra. Figure 3.7 shows an example of a hexanethiol cut A spectra. Peak A represents the singly charged particles, C the doubly charged particles, D triply charged particles, and B the paired triply charged particles. While isotopic peaks were observed in the spectra, there was no observed correlation to mass of the MPC components for the particles. The isotopic spacings are expected to be 117 mass units for the hexanethiol ligands, 197 mass units for the gold atoms, or 314 mass units for the combined thiol ligands and gold atoms. These values would be halved for the doubly charged particles and reduced to a third for the triply charged particles. The major peak spacings were not able to be determined for the singly charged particles. The spacings were found to be ~208 mass units for the doubly charged particles and ~200 mass units for the singly charged particles which does not correspond to the expected peak spacings and indicates essentially no difference for the doubly and triply charged particles. There were numerous minor isotopic peaks that could not be differentiated. This is due to the nature of the MPCs which are polydisperse in nature. Each particle contains a slightly different number of thiol ligands and gold atoms resulting in a very complicated isotopic pattern that cannot be elucidated. This was found to be true for all of the MPCs which gave MALDI specta.

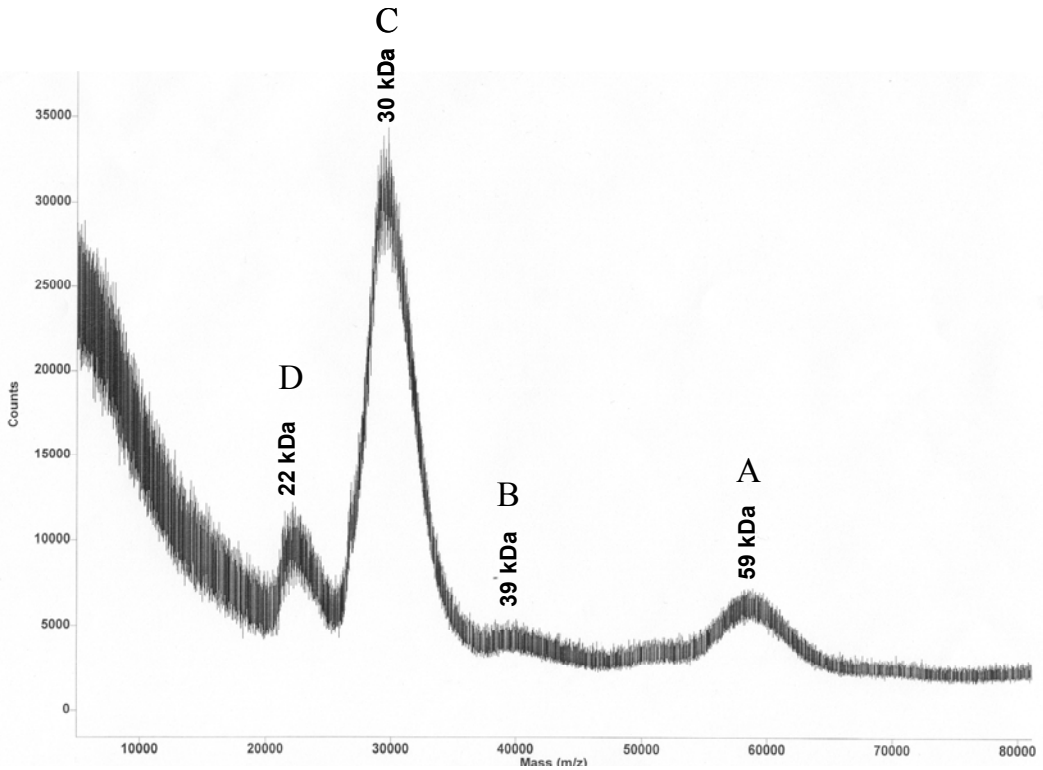

Figure 3.7 MALDI spectra of hexanethiol cut A MPCs without smoothing. A) Singly charged particles, B) paired triply charged particles C) doubly charged particles, and D) triply charged particles. Dithranol was used as the matrix in a 2:5 ratio of sample to matrix.

While the MALDI analysis was successful for investigating the molecular weight of the organic solvent soluble MPCs, it has been unsuccessful for the water-soluble MPCs. Electrospray mass spectrometry has been successfully used to analyzed water soluble glutathione MPCs and thus it is quite puzzling as to why MALDI was unsuccessful in our analyses.[113,117] Many different matrices and instrumental parameters were used in the investigation as shown in Chapter 2.3. Because of the terminating charge on the passivating thiol, it is unlikely that the MPCs were not ionized and thus not accelerated down the time of flight pathway. It was also considered that the higher mass particles are too dense rendering them unable to remain in flight during the analysis.

While this could be true for the higher mass particles like cut C of the hexanethiol MPC, this is unlikely in the case of the tiopronin MPC whose expected mass is the similar to that of cut B of the hexanethiol MPC. It is possible that the water-soluble MPCs coupled or agglomerated, forming particles of high mass, while drying. This would make them too heavy to desorb from the surface plate. The use of electrospray mass spectrometry to study water-soluble MPCs deserves more exploration in the future.

3.3 Quantized Double Layer Charging

3.3.1 Quantized Double Layer Charging Theory

It is also essential that the thermodynamic properties of the MPC such as charging potentials and particle capacitance be understood before they can be employed in their potential applications. MPCs have been shown to exhibit QDL charging peaks while in solution due the ability of the nanoparticles to store electrons in their metallic core while the thiol layer acts as a dielectric spacer, protecting the metallic core from the electrolyte solution as shown in Figure 3.8.[31,45] As a result of the dielectric layer, the electronic behavior of MPCs can be modeled as a spherical capacitor with capacitance, C, equal to

$$C = 4\pi\varepsilon\varepsilon_{\mathrm{o}}\left(\frac{r}{d}\right)\left(r+d\right)^{47} \tag{3.2}$$

where ε is the dielectric constant, ε_o is the permittivity of free space, r is the inner metallic core radius, and d is the length of the ligand.[43,47] Given that the capacitance is dependent upon the dielectric constant and the length of the protecting thiol, the capacitance of MPCs with different protecting thiols will vary. Additionally, it can be

seen from the concentric sphere model that the capacitance of nanoparticles depends upon the radius of the inner metallic core.[47]

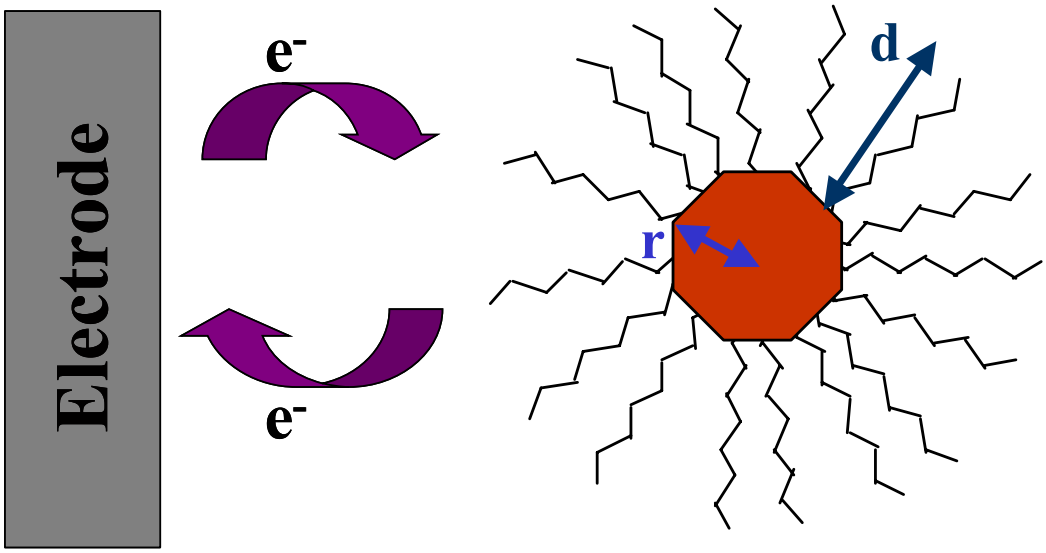

Figure 3.8 The thiol monolayer acts as a dielectric spacer and therefore the capacitance of the MPC can be modeled as a spherical capacitor where r is the radius of the inner metallic core of the nanoparticle and d is the length of the thiol monolayer.

The kinetically controlled self-assembly synthesis of MPCs always results in a distribution of MPC sizes instead of well-defined molecular compositions.[33,39] Therefore, the value of r is not constant but varies between nanoparticles. This variation in the size of the MPC then causes the capacitance values to fluctuate from one particle to another. Consequently, an MPC sample with a large range in the particle radii will not exhibit the distinct QDL charging peaks while a sample with a narrower range in particle radii will.

When the capacitance of a MPC is on the order of the fundamental charge of an electron, quantized voltage steps of electrons moving into the metallic core are observed and follow

$$Q = C * V \quad [43,45] \qquad (3.3)$$

where Q is the total charge,

$$Q = n * e \tag{3.4}$$

where n is the number of electrons, e is the charge of the electron, and V is voltage. The term quantized double layer (QDL) charging is used to describe the double layer charging resulting from the passage of one electron at a time into or out of the MPC core (n=1).[37,39-41,43,45-47,97] QDL charging is observed as distinct charging peaks in voltammograms. Capacitances observed for monodisperse MPCs are close to a single value; thus their voltammograms show distinct charging waves separated by a potential equal to Q/C as observed in Figure 3.9. Polydisperse MPCs have a broad range of capacitances which results in a washed out appearance in voltammograms as shown in Figure 3.10.

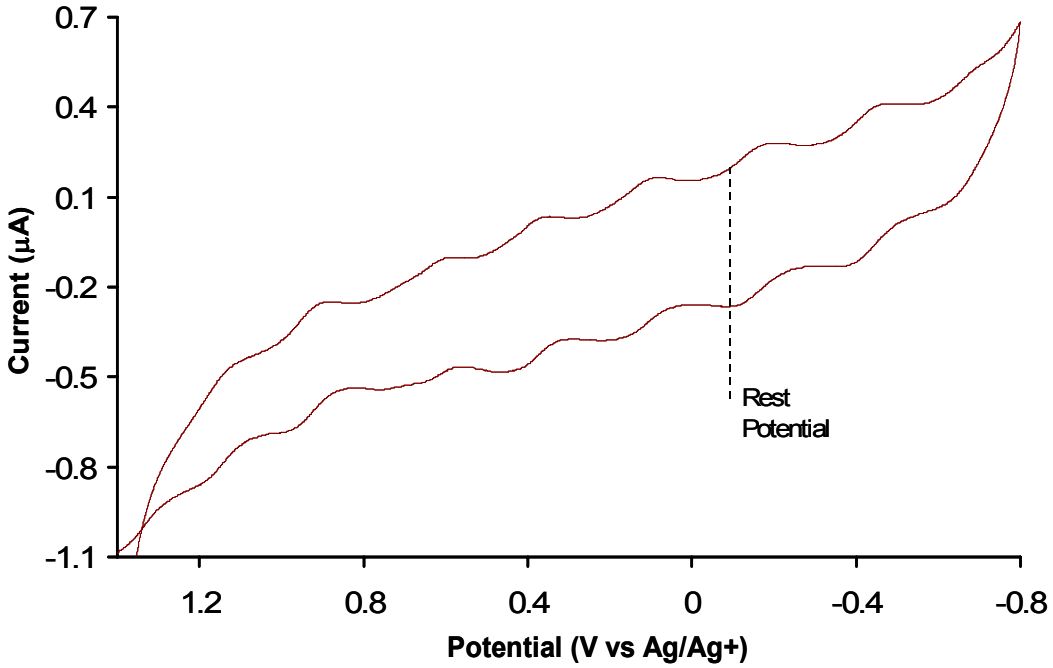

Figure 3.9 Cyclic voltammogram of hexanethiol MPCs (Cut B) which exhibits QDL charging peaks, 50 mV/s, 20 mg in 5 mL 0.1 M $TBAPF_6/CH_2Cl_2$.

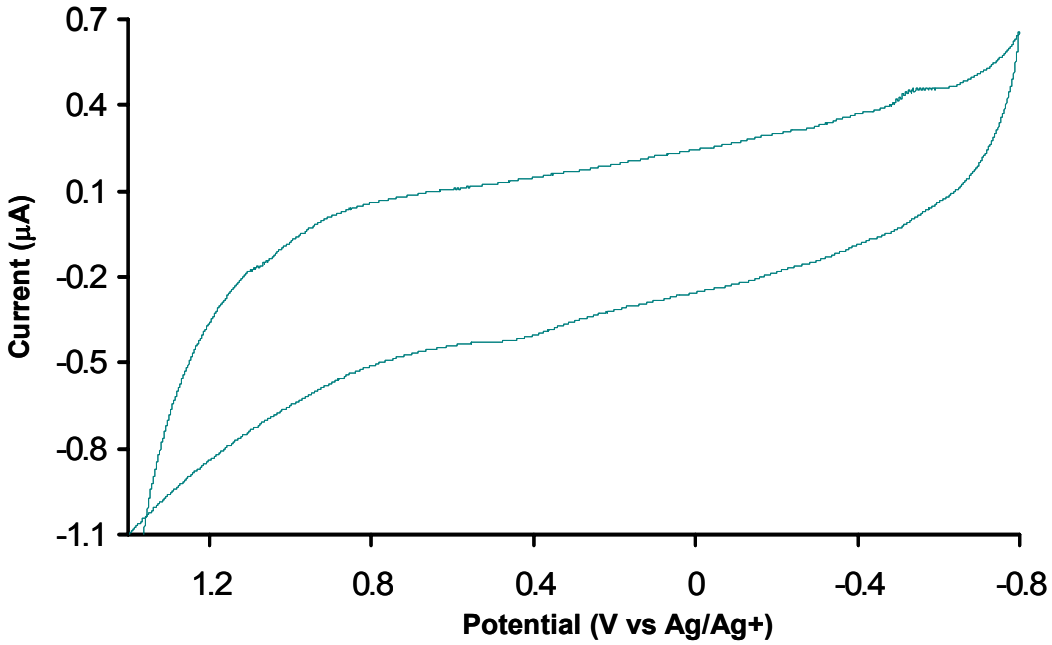

Figure 3.10 Cyclic voltammogram of hexanethiol MPCs (Cut C) which does not exhibit QDL charging peaks, 50 mV/s, 20 mg in 5 mL 0.1 M $TBAPF_6/CH_2Cl_2$.

In order to observe the transfer of an electron into and out of the inner metallic core, the energy applied, $e^2/2C$ where e is the charge of an electron, must be larger than the ambient thermal energy (k_BT), where k_B is the Boltzmann's constant which is 1.38 x 10^{-23} J/K and T is the temperature which is 298.15 K.[118-120] Therefore, the ambient thermal energy is 4.117 x 10^{-21} J and the capacitance required to observe the quantized charging is less than 3.109 x 10^{-18} F. Thus, following the standard equation for charge,

$$E = Q * V \tag{3.5}$$

where E is energy, the voltage required for the transfer of a single electron to be observable using typical electrochemical techniques is 51.46 mV.[47]

3.3.2 QDL Charging of MPCs

Gold hexanethiol MPCs have previously been observed to store charge upon bulk electrolysis and have revealed QDL capacitances, indicating multiple stable and reversible oxidation states.[41,43,47] Hexanethiol Au MPCs with a narrow size distribution were isolated and shown to have eleven QDL peaks signifying eleven stable oxidation states as shown in Figure 3.11. Graphing the potential of these oxidation states versus charge results in a linear relationship for seven charge states with a slope of 0.264 ± 0.003 as shown in Figure 3.12. This slope was the voltage required to transfer one electron and was used to calculate the capacitance of the particle. It was found that the hexanethiol Au MPCs required 264 ± 3 mV for each charging step and the capacitance of the nanoparticle was found to be 0.607 ± 0.018 aF. This is comparable to the charging voltage of 270 mV and capacitance of 0.72 aF observed by Hicks *et al.* for hexanethiol Au MPCs with a 1.0 nm radius in 2:1 toluene/acetonitrile.[43] This capacitance was determined using Equation 3.2, which makes many assumptions such as the dielectric coefficient and length of the thiol ligand, accounting for the difference in the values calculated.

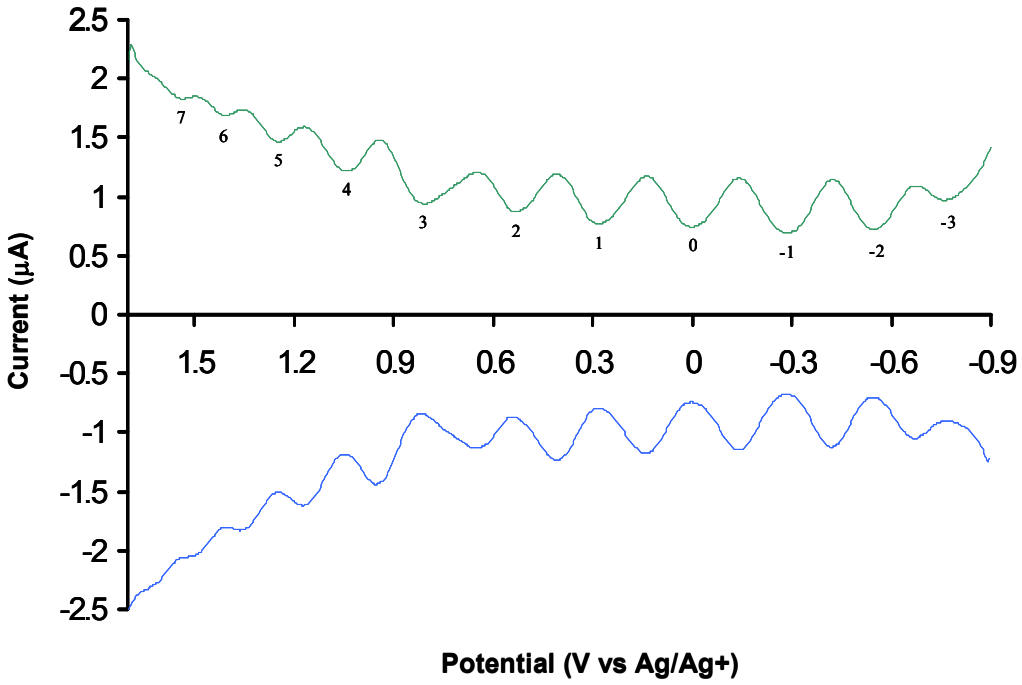

Figure 3.11 Square wave voltammogram of hexanethiol MPCs (Cut B) which exhibits QDL charging peaks, 50 mV/s, 20 mg in 5 mL 0.1 M $TBAPF_6/CH_2Cl_2$.

There is a change in slope for charge states 5-7 as shown in Figure 3.12. It was found that only 144 ± 9 mV was required for each charge step in this region which gave a capacitance of 1.11 ± 0.006 aF. This indicates that the thiol monolayer may reorder at the higher charge states. In order to verify if this is true, it would need to be observed for more charge states. Unfortunately any additional positive charge states are outside the potential window for this system and impossible to observe at this time. If the change in voltage and capacitance is a true artifact it is possibly due to a change in the configuration of the MPC. The electrolyte molecule, $TBAPF_6$, is approximately one half the size of the nanocluster. At higher charge states the cluster of electrolyte molecules could press against the cluster and cause a shrinkage or compression of the thiol ligands therefore decreasing the distance between the inner metallic core and the electrolyte solution. As

shown in Equation 3.2, a decrease in the ligand length will result in an increase in the capacitance and therefore a decrease in the potential required for each charge state.

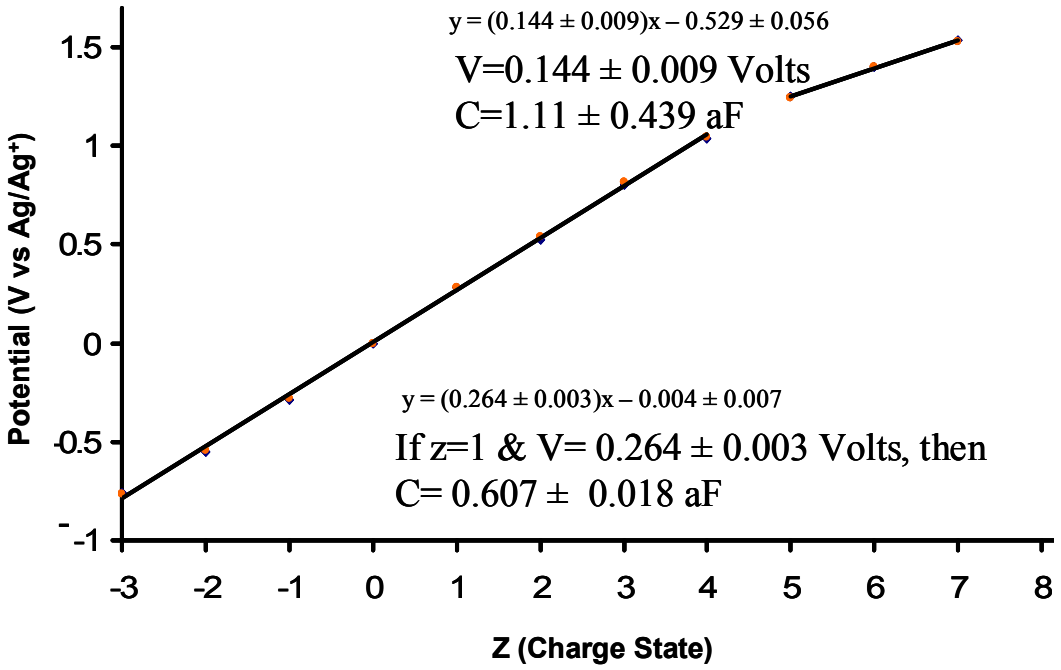

Figure 3.12 Plot of potential versus charge state for hexanethiol MPCs (Cut B) allowing the voltage required to charge the MPC and the capacitance of the MPC to be determined.

All attempts to date have been unable to produce QDL charging peaks for the other MPCs synthesized with the exception of 2-phenylethane thiol MPCs. The 2-phenylethane thiol MPC charging peaks were less distinctive due to a higher degree of particle dispersity for the MPC. Figure 3.13 shows that the capacitance of the 2-phenylethane thiol was 0.756 ± 0.050 aF while the voltage was 212 ± 5 mV which was higher than the thermal voltage and therefore discernable. The charging peaks observed for the hexanethiol and 2-phenylethane thiol MPCs show that the particles hold charge similar to capacitors and therefore have great potential for use as nanocapacitors for

molecular electronics. The absence of QDL peaks for the remaining MPCs indicates that they are either too polydisperse or their fundamental capacitance is too high which results in the voltage of the system to being too low to be observable. Further work on the 2-phenylethane thiol MPC has identified a very small set of particles (1.1 nm) that exhibited molecule-like properties. These particles revealed distinct oxidation and reduction peaks similar to a large molecule rather than the QDL charging peaks which were observed for the larger particles (1.6 nm).[96,121]

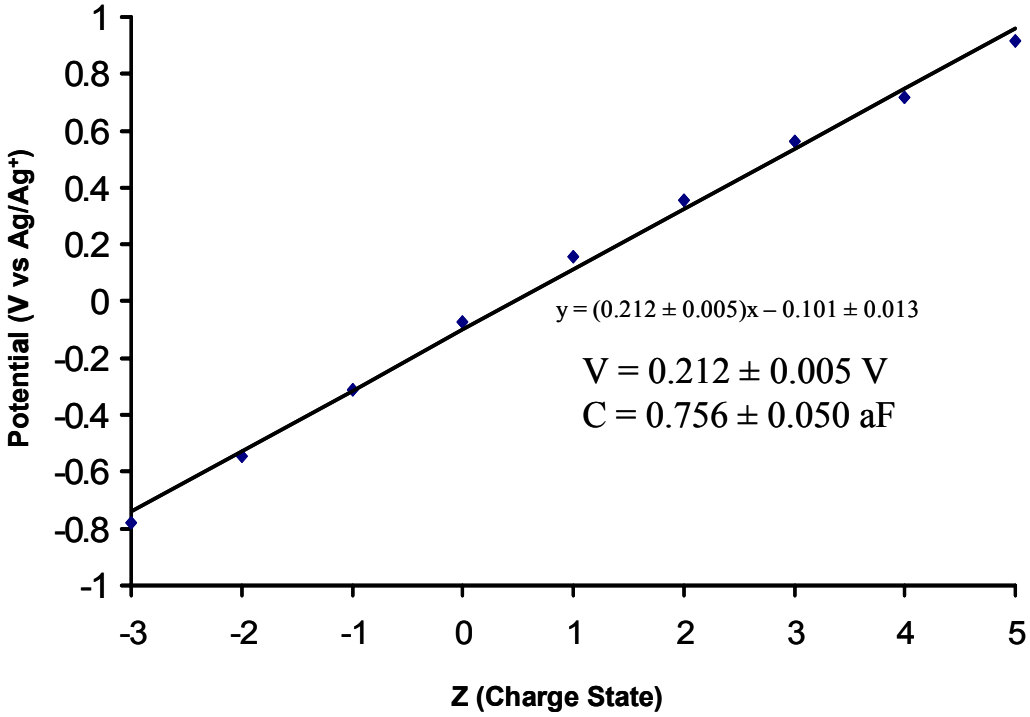

Figure 3.13 Plot of potential versus charge state for 2-phenylethane thiol allowing the voltage required to charge the MPC and the capacitance of the MPC to be determined.

3.4 Conclusions

In conclusion, several different MPCs, including organic and water-soluble varieties, were synthesized according to previously established methods. These MPCs

were characterized for their purity, size, and dispersity using ^{1}H NMR, TGA, TEM, and MALDI-MS. QDL charging peaks were only observed for hexanethiol and 2-phenylethane thiol MPCs indicating the remaining MPCs were either too polydisperse or too large to exhibit the charging peaks. With the knowledge of the capacitance values obtained above and reported in the literature, the MPCs can possibly be applied as capacitors in the developing field of molecular electronics. The regular potential intervals observed for the hexanethiol and 2-phenylethane MPC indicates that the electron transfers into or out of the MPC were actually single electron events as hypothesized by Equation 3.2. While the observance of QDL peaks allows the investigation of the thermodynamic properties of the MPC such as charging potentials and particle capacitance, the next avenue of investigation involves the determination of the kinetic properties such as electron transfer rate.

CHAPTER IV

SCANNING ELECTROCHEMICAL MICROSCOPY DETERMINATION OF ORGANIC SOLUBLE MPC ELECTRON TRANSFER RATES

4.1 Introduction

While it has been shown that MPCs store charge, it is essential that the electron transfer properties of the nanoparticles be understood before they can be used in nanotechnology. There have been numerous studies on the electron transfer properties of MPCs in films while there have been very few studies on the electron transfer properties MPCs free in solution. A wide variance in the measured electron transfer rates was observed for the different studies due to the different methods employed and difficulties in the formation of MPC films. Additionally, it is impossible to determine the effects the linkers, used to make MPC films, have on the electron transfer rates measured.[39,50,65-72] Therefore, another method is needed to measure the rate of electron transfer through the thiol monolayer of the MPCs that is simple and straightforward.

In this study the measurement of the electron transfer rate of MPCs free in solution is described using a novel method employing the SECM. As stated previously, MPCs exhibit either multiple charging peaks or none at all. Thus, previous SECM methods developed to measure the electron transfer rate of molecules in solution using standard redox potential cannot be used when investigating MPCs.

4.2 Kinetic Theory

4.2.1 Mass Transfer Limited Electron Transfer

In order to determine the rate of electron transfer of MPCs it is important to start with basic electrode kinetics. The rate of an electrode reaction is often more complex than a solution or gas phase reaction which is also known as a homogeneous reaction. An electrode reaction is known as a heterogeneous reaction because it only occurs at the interface between the electrode and electrolyte. A heterogeneous reaction rate is dependent upon many factors including mass transfer and kinetic transfer as shown in Figure 4.1. Mass transfer is defined as the diffusion of the species through the bulk solution to the electrode while kinetic transfer is defined as the transfer between the electrode and the species at the electrode surface. Electrode reaction rates are typically defined as

$$\text{Rate} = \frac{i}{nFA} \tag{4.1}$$

where i is current, n is the number of electrons transferred, F is Faraday's constant, and A is the area of the electrode. For most reversible electrochemical reactions the mass transfer aspect of electron transfer is the limiting process resulting in the following relationship

$$i_l = nFAm_{\mathrm{O}}C_{\mathrm{O}}^{*} \tag{4.2}$$

where i_l is the limiting current, m_{O} is the mass transfer coefficient of the oxidized species, and C_{O}^{*} is the bulk concentration of the oxidized species,.[110]

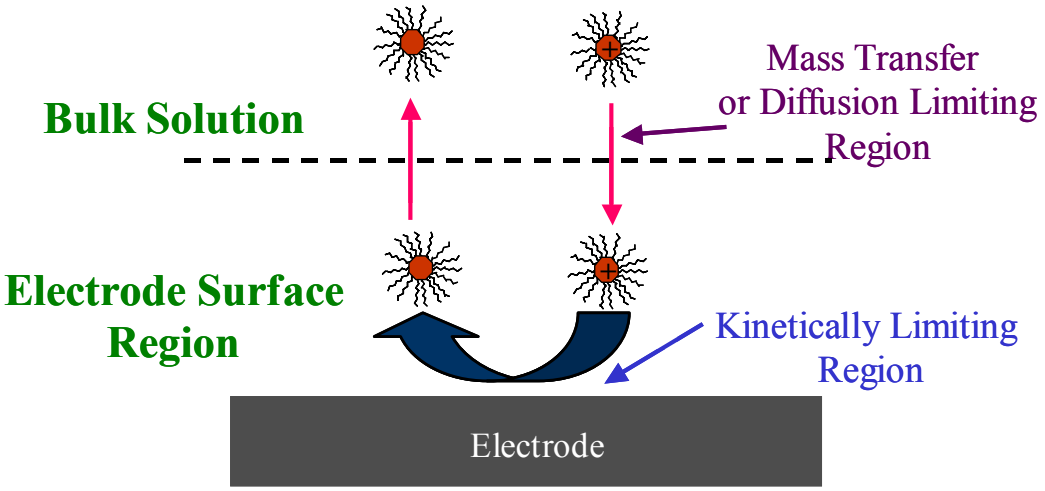

Figure 4.1 Mass transfer and kinetic transfer limiting electron transfer pathways. The diffusion of the species through the bulk solution to the electrode is the mass transfer limited pathway while the movement of the electron from the electrode to species is the kinetically limited pathway.

4.2.2 Electrode Kinetics

Electrochemically, a reaction at an electrode is characterized as

$$\mathrm{O} + ne \underset{k_b}{\overset{k_f}{\rightleftarrows}} \mathrm{R} \tag{4.3}$$

where O is the oxidized species, R is the reduced species, n is the number of electron transferred, e is the electronic charge, k_f is the heterogeneous rate constant for reduction, and k_b is the heterogeneous rate constant for oxidation. This equilibrium expression is characterized by the Nernst equation

$$E = E^{0'} + \frac{RT}{nF} \ln \frac{C_O^*}{C_R^*} \tag{4.4}$$

where E is the electrode potential relative to a reference, $E^{0'}$ is the formal potential of the system, R is the gas constant, T is the temperature, and C_R^* is the bulk concentration of the reduced species.[110]

In the simplest form the forward rate, υ_f, of the electrode reaction can be defined as

$$\upsilon_f = k_f C_O(0,t) \tag{4.5}$$

where $C_O(0,t)$ is the concentration of the oxidized species at the surface of the electrode at time t. The forward reaction is a reduction and therefore results in a cathodic current, i_c, which is related to the forward rate as follows

$$\upsilon_f = \frac{i_c}{nFA}. \tag{4.6}$$

The reverse rate υ_b, of the electrode reaction and the anodic current can be defined as

$$\upsilon_b = k_b C_R(0,t) = \frac{i_a}{nFA}. \tag{4.7}$$

The overall reaction rate, υ_{net}, can be defined as

$$\upsilon_{net} = \upsilon_f - \upsilon_b \tag{4.8}$$

and the overall current, i, as

$$i = i_c - i_a = nFA\left[k_f C_O(0,t) - k_b C_R(0,t)\right]. \tag{4.9}$$

Heterogeneous rate constants typically have the units of cm/s.[110]

4.2.3 Butler-Volmer Model of Electrode Kinetics

It has been shown that the kinetics of a reaction is affected by the potential on the electrode. For example, hydrogen has been shown to evolve at some potentials but not at others. Therefore, it is valuable to be able to predict the way the rate depends upon potential. In order to determine this relationship it was found to be convenient to express

the electrode potential relative to the equilibrium potential, E_{eq}, or the standard (or formal) potential of the system, $E^{0'}$.[110]

Assuming a one-electron process Equation 4.1 can be redefined as

$$O + e \underset{k_b}{\overset{k_f}{\rightleftarrows}} R . \tag{4.10}$$

When the electrode interface is at equilibrium, $E^{0'}$ is the potential at which the rates constants have the same value, $k_f = k_b$. This value is known as the standard rate constant, $k^0[s^{-1}]$. The rate constants at electrode potentials other than the standard potential can be defined as

$$k_f = k^0 \, e^{-\alpha f(E-E^{0'})} \tag{4.11}$$

and

$$k_b = k^0 \, e^{(1-\alpha) f(E-E^{0'})} . \tag{4.12}$$

where α is the transfer coefficient which must be between 0 and 1 and typically ranges from 0.3 to 0.7 and $f = F/RT$. Combining equations 4.10 and 4.11 with 4.8 results in the complete current-potential characteristic,

$$i = FAk^0[C_O(0,t)\, e^{-\alpha f(E-E^{0'})} - C_R(0,t)\, e^{(1-\alpha) f(E-E^{0'})}] . \tag{4.13}$$

This relationship is valuable because it, or a variation, is used in almost every issue relating to heterogeneous kinetics and therefore it is known as the Butler-Volmer model.[110]

The standard rate constant shows the ability of a system to reach equilibrium. A large k^0 indicates the system will reach equilibrium quickly while a small k^0 indicates the system will be slow. The Butler-Volmer model also demonstrates that the rate of reduction and oxidation is dependent upon both the electrode potential and the standard

redox potential of the system, ($E - E^{0'}$). Therefore, even if k^0 is quite small, k_f and k_b can be made very large by applying a sufficient electrode potential relative to the standard potential of the system. The electrode potential provides the activation energy and can, in effect, drive the reaction and result in a fast electron transfer rate.[110]

4.2.4 Tafel Realationship

While at equilibrium the net current is zero, the faradaic activity can be expressed as the exchange current, i_0, which is equal to either the anodic or the cathodic currents, can be expressed as

$$i_0 = FAk^0 C_O^{*(1-\alpha)} C_R^{*\alpha}. \tag{4.14}$$

This shows that the exchange current is proportional to and therefore is often substituted for the standard rate constant. When the concentration of both the oxidized and reduced species are equal, the exchange current follows

$$i_0 = FAk^0 C. \tag{4.15}$$

The advantage of using the exchange current, i_0, rather than the standard rate constant, k^0, is the use of overpotential, η, rather than the standard potential, $E^{0'}$. Overpotential is the difference between the electrode potential and the equilibrium potential. Using overpotential, the current can be defined as

$$i = i_0 \left[\frac{C_O(0,t)}{C_O^*} e^{-\alpha f \eta} - \frac{C_R(0,t)}{C_R^*} e^{(1-\alpha) f \eta} \right].^{110} \tag{4.16}$$

The surface concentration does not significantly differ from bulk concentrations when there is no mass transfer component to the electron transfer rate or the currents are kept very low. In this case, Equation 4.16 becomes

$$i = i_0 \left[e^{-\alpha f \eta} - e^{(1-\alpha) f \eta} \right]. \tag{4.17}$$

At small overpotentials Equation 4.17 can be expressed as

$$i = -i_0 f \eta \tag{4.18}$$

while for large overpotentials Equation 4.17 can be expressed as

$$i = i_0 e^{-\alpha f \eta} \tag{4.19}$$

or

$$\eta = \frac{2.3RT}{\alpha F} \log i_0 - \frac{2.3RT}{\alpha F} \log i . \tag{4.20}$$

Equation 4.20 is similar to the Tafel relationship, resulting from early studies, which follows

$$\eta = a + b \log i . \tag{4.21}$$

A Tafel plot, log *i vs.* η, is used to determine the exchange current, i_0, and transfer coefficient, α.[110]

4.2.5 Electron Transfer via Tunneling

The probability of tunneling is used to evaluate to likelihood an electron will tunnel through a material. The probability of an electron tunneling follows

$$\text{Probability of Tunneling} \propto e^{(-\beta x)} \tag{4.22}$$

where x is the distance of the electron transfer and β ($Å^{-1}$) is a factor which depends upon the height of the energy barrier and the nature of the medium between the states (a large β results in a slow electron transfer rate). When considering electron transfer kinetics the tunneling effects can be incorporated into the electronic transmission coefficient, κ_{el}, as follows

$$\kappa_{el} = \kappa_{el}^{\ 0}\, e^{(-\beta x)} \tag{4.23}$$

where $\kappa_{el}^{\ 0}$ is the standard transmission coefficient. The transmission coefficient also was used to create Marcus' Theory model for k_f from first principles as follows

$$k_f = K_{P,O} \nu_n \kappa_{el} e^{\left(\frac{\Delta G_f^{\dagger}}{RT}\right)} \tag{4.24}$$

where $\Delta G_f^{\dagger}$ is the activation energy for reduction of the oxidized species, $K_{P,O}$ is a precursor equilibrium constant, and ν_n is the nuclear frequency factor. This relationship shows the transmission coefficient is proportional to the forward heterogeneous rate constant. Therefore, the heterogeneous rate constant can be used to estimate β. It has been shown for self-assembled monolayers (SAMs) that a plot of the natural log of the rate constant versus the chain length allows the determination of β. It has also been shown that the β typically ranges from 1 to 1.2 $Å^{-1}$ for saturated chains and 0.4 to 0.6 $Å^{-1}$ for π-conjugated molecules.[110] Additionally, McCreery has shown that β is approximately 2.3 $Å^{-1}$ for a vacuum gap between two metals and 1.0 $Å^{-1}$ for a molecular junction.[122]

4.3 Scanning Electrochemical Microscopy

4.3.1 SECM Theory

The SECM was developed by Bard and coworkers in 1989 and has been used for various applications including the measurement of the heterogeneous standard rate constant.[73,74] Figure 4.2 shows a diagram of a typical SECM which consists of a bipotentiostat and a micropositioner. In SECM, a redox mediating species, MPC in this

case, is electrochemically cycled between an ultramicroelectrode (UME) tip, with a diameter less than 25 μm, and a macro-sized substrate electrode as shown in Figure 4.3. The substrate electrode can be conductive, semiconductive, or insulating depending upon the particular study.[75] The position of the UME is controlled by a micropositioner composed of three independent piezoelectric motors, which allow independent manipulation in the x, y, and z directions. This permits the SECM to be a valuable tool in the measurement of electron transfer rates and imaging surfaces. Additionally, in SECM, measurements are made at steady state, therefore eliminating the problem of double layer charging present in many other analytical methods such as cyclic voltammetry and chronoamperometry, making it a very valuable tool for measuring electron transfer properties.[73,76] While SECM is similar to STM, the current is not tunneled between the tip and substrate but instead is carried by an electrochemical mediator. In addition, STM is often limited to 30 nm by 30 nm surface scan area while SECM can provide a lower resolution image of a larger surface area.[73-75]

There are several different modes of operation of the SECM. The tip generation-substrate collection mode, which employs the UME to generate a reactant that is then detected at the substrate, is typically used to investigate homogeneous reactions. The substrate generation-tip collection mode, which employs the substrate to generate the reactant that is then detected at the UME, is typically used to investigate reactions at the substrate surface. The most common method is the feedback mode, which employs a tip to approach the stationary substrate at an incremental rate, is used to investigate electrode transfer rates.[73,74,123]

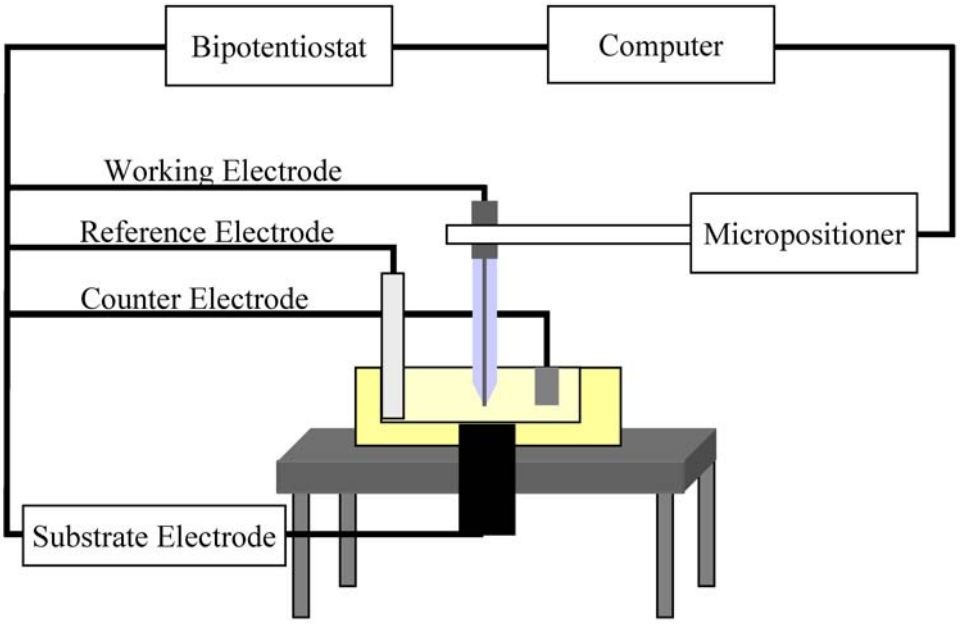

Figure 4.2 Diagram of the SECM. The SECM consists of a biopotentiostat, computer, microposistioner, and four-electrodes. The four-electrodes consist of the substrate, working, reference, and counter electrodes. The working electrode is controlled by a micropositioner to allow control in the x, y, and z axes.

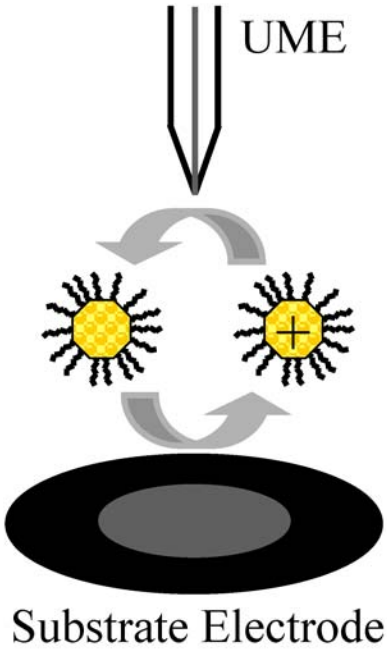

Figure 4.3 SECM redox cycling of MPCs between the UME and substrate electrode. Here the substrate oxidizes the MPC while the tip reduces the MPC.

4.3.2 SECM Determination of the Mass Transfer Limited Electron Transfer

In the feedback mode, which is used in this dissertation, an approach curve is recorded. When the tip is far from the substrate (*i.e.* several tip diameters), the current is limited by steady state diffusion. The mass transfer coefficient for steady state diffusion, m_{ss}, to a UME follows

$$m_{ss} = \frac{4D_{\mathrm{O}}}{\pi a} \tag{4.25}$$

where D_{O} is the diffusion coefficient and a is the radius of the UME. Substitution of m_{ss} for m_{O} shows that the steady state current, i_{ss}, can be defined as

$$i_{ss} = 4nFD_{\mathrm{O}}C_{\mathrm{O}}^{*}a \tag{4.26}$$

In the case of an insulating substrate, as the tip approaches the surface of the substrate the redox mediator is blocked from diffusing to the UME as shown in Figure 4.4. This results in a decrease in the tip current and is known as negative feedback. Alternatively, when a conducting substrate is used, as in this dissertation, the redox mediator is regenerated at the substrate. This results in an increase in the tip current and is known as positive feedback as shown in Figure 4.5. The positive feedback current, i_l, follows Equation 4.2 when the electron transfer is limited by mass transfer.[73,74,124,125]

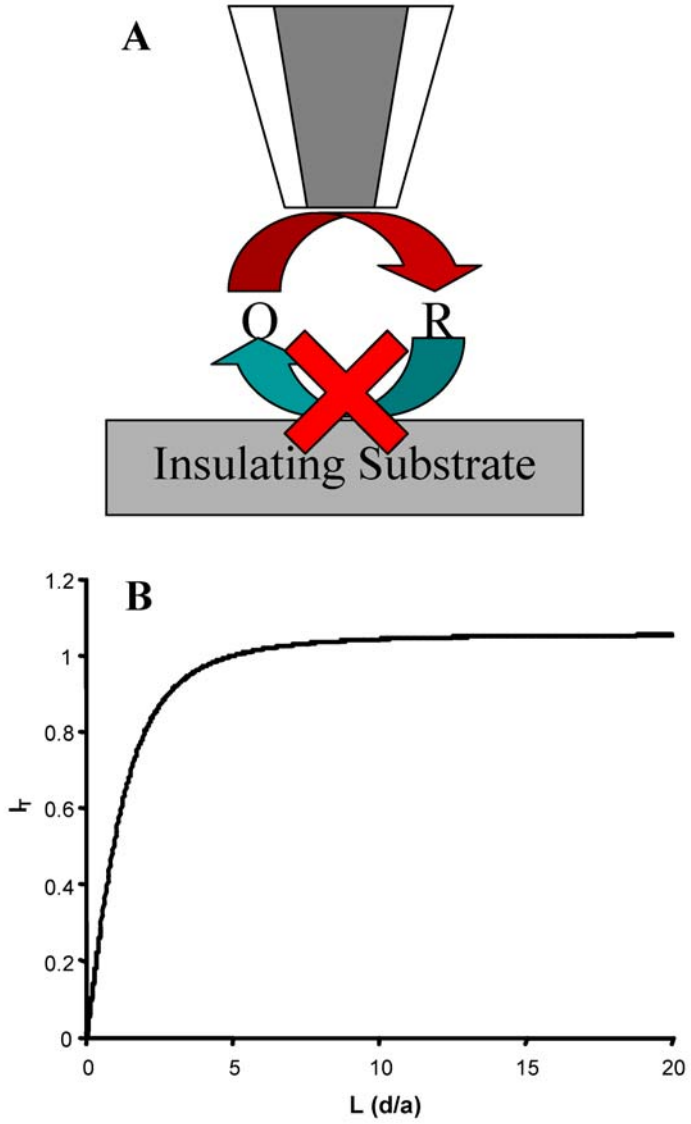

Figure 4.4 A) Diagram of a UME approaching an insulating substrate in which redox mediator is blocked. B) SECM approach curve resulting from an approach to an insulating substrate. The approach curve shows a negative feedback due to the blocking of the redox mediator.

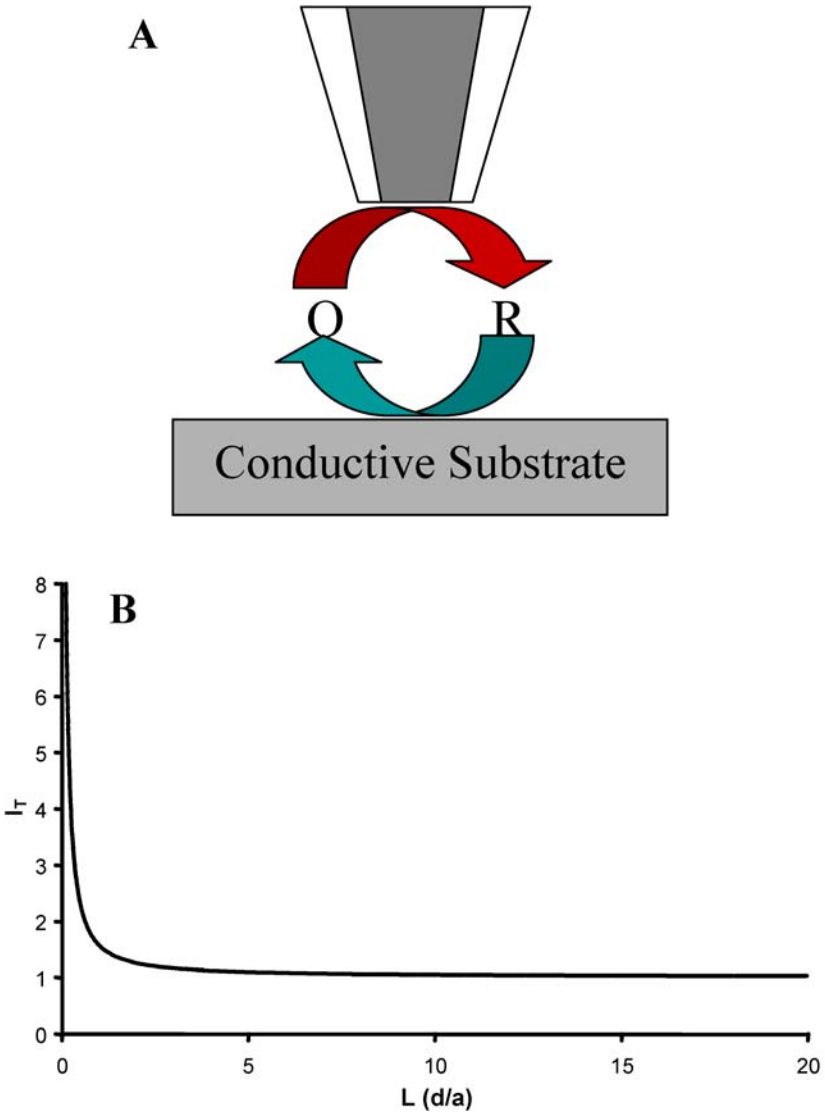

Figure 4.5 A) Diagram of a UME approaching a conductive substrate in which the redox mediator is regenerated. B) SECM approach curve resulting from an approach to a conductive substrate. The approach curve shows a positive feedback due to the regeneration of the redox mediator.

Typically, for the current from a recorded approach curve, i_l is divided by i_{ss} to obtain the dimensionless experimental current parameter, I_T, which follows

$$I_T = \frac{i_l}{i_{ss}} = \frac{Am_O}{4D_O a} = \frac{\pi a m_O}{4D_O}. \tag{4.27}$$

I_T is independent of the solution concentration, the diffusion coefficient, and the number of electrons transferred.[73,74,124] The mass transfer coefficient can be determined by rearranging Equation 4.27 as follows

$$m_O = I_T\left(\frac{4D_O}{\pi a}\right). \tag{4.28}$$

Substitution of Equation 4.25 into Equation 4.28 results in the following expression

$$m_O = I_T m_{ss}. \tag{4.29}$$

As shown in Equation 4.28, the mass transfer coefficient is dependent upon the radius of the UME. The use of smaller UME diameters will allow for a faster mass transfer coefficient to be determined. If the UME is sufficiently small, the electron transfer will not be mass transfer limited, but kinetically limited.[73,74]

In order to evaluate the limiting factor in the approach curve currents, I_T is plotted versus the dimensionless distance parameter, $L = d/a$, where d is the distance separating the electrodes. The experimental approach curves are then compared to the theoretical model of mass transfer limited processes as proposed by Bard *et al*. in the following equation

$$I_T(L) = 0.68 + \left(\frac{0.78377}{L}\right) + 0.3315\,e^{\left(\frac{-1.0672}{L}\right)}.^{29,73,74,124} \tag{4.30}$$

MPCs whose approach curves follow this model exhibit electron transfer rates that are mass transfer limited. If the approach curve deviates from model, presenting a lower

feedback current, then the electron transfer is kinetically limited and therefore its electron transfer rate can be measured. The combination of Equations 4.28 and 4.30 results in

$$m_{\mathrm{O}} = \left[0.68 + \left(\frac{0.78377}{L} \right) + 0.3315\, \mathrm{e}^{\left(\frac{-1.0672}{L} \right)} \right] \left(\frac{4D_{\mathrm{O}}}{\pi a} \right). \tag{4.31}$$

Therefore, if the approach curve follows the mass transfer theory proposed by Bard, the mass transfer coefficient can be easily calculated.

4.3.3 SECM Determination of the Kinetically Limited Electron Transfer

As stated previously, the electron transfer rate is effected by both mass transfer and kinetic transfer. The current observed for kinetically limited processes, i_{K}, follows

$$i_{\mathrm{K}} = nFAk_{\mathrm{f}}C_{\mathrm{O}}^{*}.^{73} \tag{4.32}$$

which is similar to the mass transfer limited current shown in Equation 4.2. Since the electron transfer rate is limited by both the mass transfer of the MPC and the kinetic transfer of the electron across the thiol layer, the currents can be modeled as parallel resistors in a circuit, such as

$$\frac{1}{i_{\mathrm{exp}}} = \frac{1}{i_l} + \frac{1}{i_{\mathrm{K}}} \tag{4.33}$$

where i_{exp} refers to the parallel combination of currents. This can be translated to

$$i_{\mathrm{exp}} = \frac{i_l i_K}{i_l + i_K} \tag{4.34}$$

Substituting this into relationship with the mass transfer coefficient of Equation 4.2 results in the relationship

$$i_{l(\mathrm{II})} = nFA\left(\frac{m_{\mathrm{O}}\ k_{\mathrm{f}}}{m_{\mathrm{O}}\ + k_{\mathrm{f}}} \right) C_{\mathrm{O}}^{*} \tag{4.35}$$

where $i_{l(\text{II})}$ is the current resulting from both mass transfer and kinetic transfer. This equation will be used to evaluate the approach curves which deviate from Bard's theory, Equation 4.28, to determine the kinetic component of the current. In order to evaluate the kinetic limit to electron transfer the current resulting from the steady state must also be redefined using the parallel model. Combination of Equations 4.25, 4.26, and 4.34 results in

$$i_{ss(\text{II})} = nFA\left(\frac{m_{ss}\ k_{\text{f}}}{m_{ss}\ + k_{\text{f}}}\right)C_{\text{O}}^{*} \tag{4.36}$$

where $i_{ss(\text{II})}$ steady state current resulting from both mass transfer and kinetic transfer. As previously explained, $i_{l(\text{II})}$, Equation 4.35, is divided by $i_{ss(\text{II})}$, Equation 4.36, to obtain dimensionless experimental current parameter resulting from both mass transfer and kinetic transfer, $I_{\text{T(II)}}$, which follows

$$I_{\text{T(II)}} = \frac{i_{l(\text{II})}}{i_{ss(\text{II})}} = \frac{\left(\dfrac{m_{\text{O}}k_{\text{f}}}{m_{\text{O}} + k_{\text{f}}}\right)}{\left(\dfrac{m_{ss}k_{\text{f}}}{m_{ss} + k_{\text{f}}}\right)} \tag{4.37}$$

Substituting Equation 4.29, $m_0 = I_{\text{T}}m_{ss}$ into Equation 4.37 results in

$$I_{\text{T(II)}} = \frac{\dfrac{I_{\text{T}}m_{ss}k_{\text{f}}}{I_{\text{T}}m_{ss} + k_{\text{f}}}}{\dfrac{m_{ss}\ k_{\text{f}}}{m_{ss} + k_{\text{f}}}} \tag{4.38}$$

which can be rearranged as

$$I_{\text{T(II)}} = \frac{\left(\ I_{\text{T}}\left(m_{ss} + k_{\text{f}}\right)\right)}{\left(\ I_{\text{T}}m_{ss} + k_{\text{f}}\right)}. \tag{4.39}$$

Substitution of Equation 4.25 results in

$$I_{T(II)} = \frac{\left(I_T \left(\left(\frac{4D}{\pi a} \right) + k_f \right) \right)}{\left(\left(\frac{4D}{\pi a} \right) I_T + k_f \right)}. \quad (4.40)$$

Equation 4.40, which only has one variable, k_f, will be used to determine the forward heterogeneous rate constant for the MPCs. To do this, the experimental MPC approach curves are compared to $I_{T(II)}$, where k_f will be adjusted until the best fit is achieved, resulting in the forward heterogeneous rate constant for the MPC.

As stated earlier, previous methods to determine the kinetic rate of electron transfer required the standard redox potential of the analyte, the number of electrons transferred, or the concentration of the analyte to be known. These methods do not work for MPCs which can exhibit either multiple or no QDL charging peaks. Additionally, many of the clusters have not revealed any QDL charging peaks because they are too polydisperse and therefore it is impossible to determine their standard redox potential. In the case of MPCs, the QDL charging peaks allows the number of electrons transferred to be determined. If the charging peaks cannot be observed it is impossible to determine the number of electrons transferred at any applied potential. Additionally, while it is possible to determine an approximate MPC concentration, it is impossible to determine the exact MPC concentration. A few very large particles can skew the concentration estimated and therefore introduce error into the measurement of the electron transfer rate. The use of Equation 4.40 allows the forward heterogeneous rate constant, which will be referred to as the kinetic rate of electron transfer, to be determined for MPCs that exhibit either multiple or no clearly defined oxidation and reduction states. This eliminates the need

for the standard redox potential, number of electrons transferred, and concentration making it a very easy method of measuring electron transfer rates for MPCs.

4.4 Results and Discussion

4.4.1 Biased versus Unbiased Substrate

In this research, SECM approach curves were employed to investigate the electron transfer characteristics of alkanethiol MPCs. Figure 4.3 shows a diagram of the MPC charging by SECM. As shown previously, the determination of the electron transfer properties of the MPCs is dependent upon i_l, Equation 4.2, and i_{ss}, Equation 4.26. In order obtain I_T, Equation 4.27, it is essential that the number of electrons, n, either be known for each case or cancel. In order to illustrate this, n_1 and n_2 can be substituted in to Equation 4.27 as follows

$$I_T = \frac{i_l}{i_{ss}} = \frac{n_1 FAm_O C}{4n_2 FDCa}. \tag{4.41}$$

The MPCs in solution have a native charge state before the experiment begins. The use of a biased substrate will cause local charging of the MPCs to the substrate potential resulting in a biased state rather than their native state. During an approach curve, the MPC is cycled between the tip and substrate, which causes the nanoparticle to be charged to the biased substrate potential transferring n_1 electrons. Conversely, when the tip is far from the substrate (steady state conditions), the MPC can then diffuse through the solution and return to the native charge state of the MPC solution transferring n_2 electrons. The use of an unbiased substrate electrode guarantees that the number of

electrons transferred at the substrate is the same as the number of electrons transferred far away, therefore ensuring that the two variables can be canceled ($n_1 = n_2$).

Unfortunately, many of the electron transfer characteristics studies were conducted using a biased substrate electrode. As a result, it is essential to determine if the number of electrons transferred between the MPC and UME is different when the tip is far from rather than close to the substrate. In order to do this, the time it would take for the MPCs to diffuse between the UME and substrate to become biased was determined using the diffusion layer thickness, δ, which follows

$$\delta = \sqrt{2Dt} \tag{4.42}$$

where D is 3 X 10^{-6} cm^2/s.[126] The diffusion layer thickness was considered to be 100 μm because this was the maximum distance the UME was backed away from the substrate between approach curves. From Equation 4.42 it was found that it would take 17 s for the MPCs present in the 100 μm diffusion layer to be biased to the substrate potential. Before each approach curve a quiet time of at least 100 s was employed in which the UME and substrate electrode are both held at the potentials used during the approach curve to allow the solution to equilibrate. Therefore, the quiet time was more than sufficient to allow the MPCs to be biased to that of substrate electrode within the diffusion layer and the number of electrons transferred is the same when the UME is far from the substrate or the UME is close to the substrate ($n_1 = n_2$). Consequently, the approach curves completed with the substrate electrode biased and unbiased are equally relevant in this investigation.

4.4.2 SECM Analysis of MPCs

4.4.2.1 Mass Transfer Limited Hexanethiol MPCs

A typical set of approach curves, I_T *vs*. L, obtained using hexanethiol MPCs with a 10 μm Pt UME is shown in Figure 4.6. These approach curves follow the mass transfer limited model, $I_{T,}$ as given by Bard, which indicates that the electron transfer through the hexanethiol monolayer is mass transfer limited.[73] The mass transfer rate was determined to be 0.083 cm/s using Equation 4.28 and the observed UME current, I_T, of 9. Because the hexanethiol MPCs electron transfer was shown to be mass transfer limited, the kinetic rate of the electron transfer is as fast or faster than the mass transfer coefficient ($k_f \geq$ 0.083 cm/s). As shown in Equation 4.28 a reduction in the UME size will allow for the analysis of a faster mass transfer coefficient; consequently, a smaller UME with an increased mass transfer coefficient is required to further investigate the forward heterogeneous rate constant, k_f, of the hexanethiol MPCs.

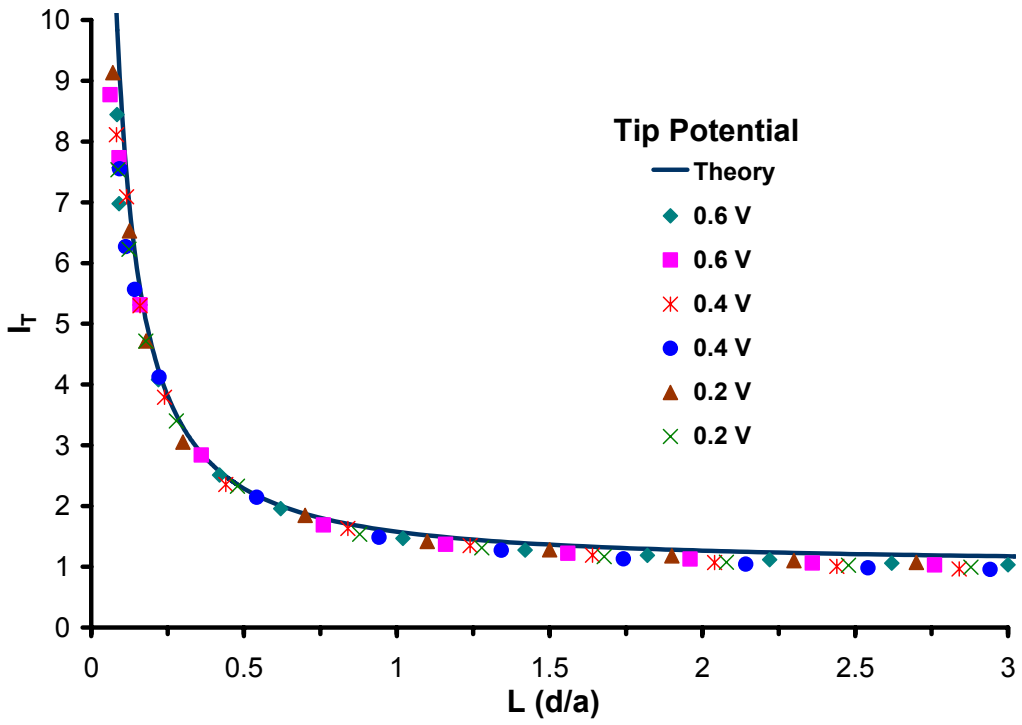

Figure 4.6 SECM approach curves of hexanethiol MPCs with a 10 µm UME at various potentials with the substrate electrode held at 0 V. The samples consisted of 20 mg of sample in 5 mL of 0.1 M $TBAPF_6$ in CH_2Cl_2.

4.4.2.2 Kinetically Limited Hexanethiol MPCs

SECM analysis of hexanethiol MPCs with a smaller UME shown in Figure 4.7 exhibited a deviation from Bard's theory of mass transfer. While the current reached an I_T as high as 8 the slope did not follow the mass transfer theory.[73] Therefore the electron transfer must be kinetically limited. The approach curve conducted with the UME at 100 mV resulted in no positive feedback because there was not enough of a potential difference between the tip and substrate to result in the charging of the nanoparticle. Additionally, the approach curves conducted with the UME at 900 mV and 800 mV vs. Ag/AgCl were not shown because the tip potential was near the edge of the potential

window and therefore resulted in a diminished feedback current resulting from an irreversible solvent oxidation.

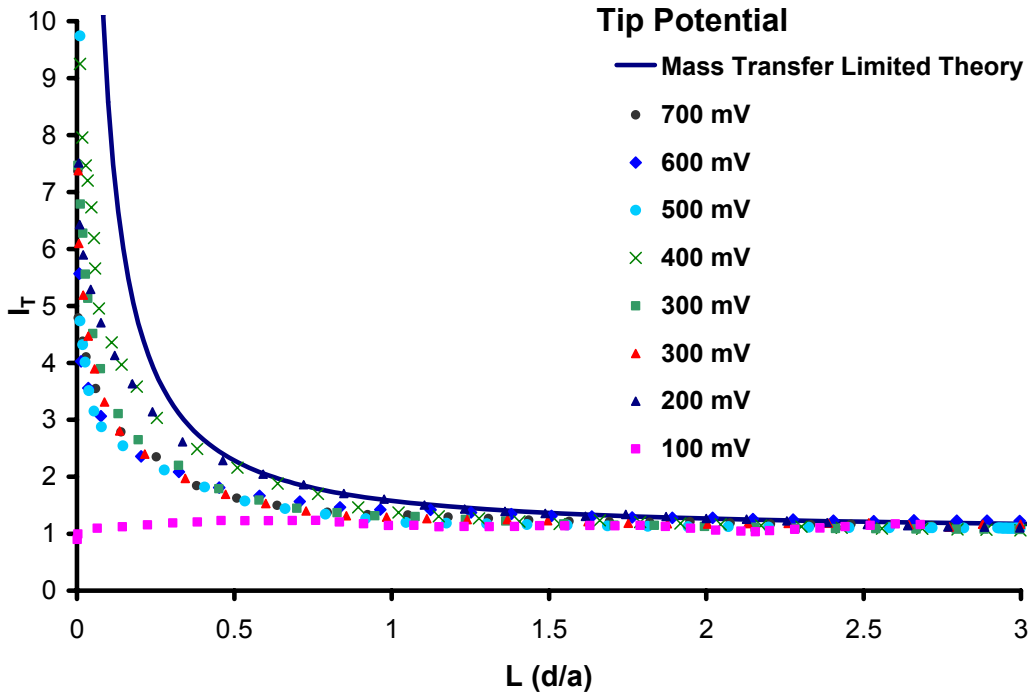

Figure 4.7 SECM approach curves of hexanethiol MPCs with a 5 μm UME at various positive potentials with an unbiased substrate electrode, Ag/Ag^+ non-aqueous reference electrode, and a Pt wire counter electrode. The samples comprised of 20 mg of sample in 5 mL of 0.1 M $TBAPF_6$ in CH_2Cl_2.

The forward heterogeneous rate constant, k_f, was found by comparison to a $I_{T(II)}$ curve. The rate of the electron transfer through the hexanethiol monolayer was found to be 0.11 ± 0.03 cm/s. As shown in Figure 4.7, the hexanethiol MPC approach curves only slightly deviate from Bard's theory of mass transfer. The mass transfer coefficient can be determined as shown previously. The measurement of I_T ranged from barely over 4 to 8 during the investigation of this MPC resulting in a mass transfer coefficient of 0.073 cm/s

and 0.15 cm/s respectively. The wide range in positive feedback accounts for the relatively high error associated with the measurement of the heterogeneous rate constant.

It was shown that the hexanethiol MPC showed a positive feedback in current for both positive and negative potentials (not shown) indicating that these particular MPCs act as conductors throughout their solvent potential window. This signifies that the hexanethiol MPC can be both positively and negatively charged which is consistent with the previously observed charging peaks from square wave voltammetry for the hexanethiol MPCs shown in Figure 4.8.

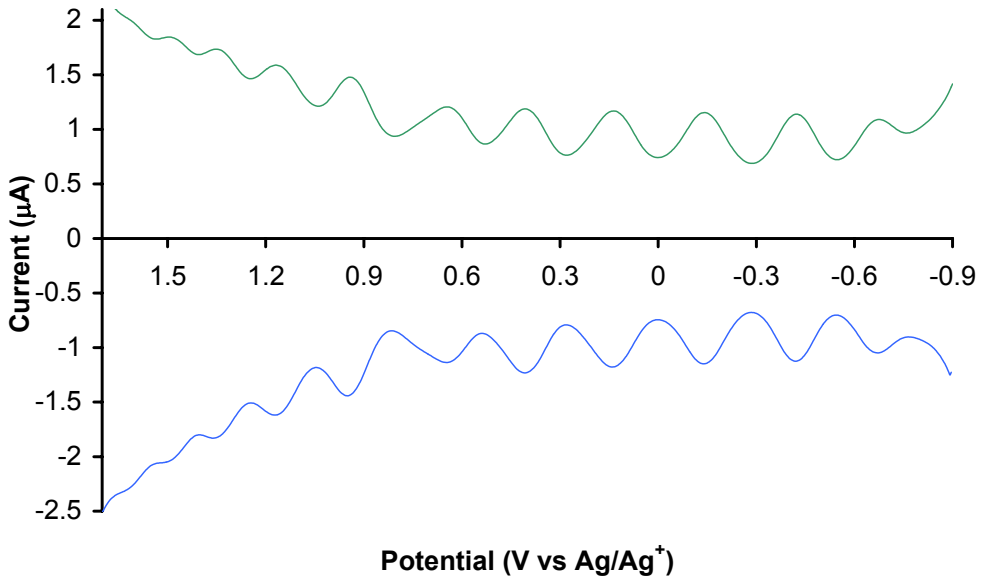

Figure 4.8 Square wave voltammogram of hexanethiol Cut B MPCs which exhibits both positive and negative charging of the nanoparticle.

4.4.2.3 Octanethiol, Decanethiol, and Dodecanethiol MPCs

A 10 μm Pt UME was used to acquire SECM approach curves of octanethiol, decanethiol, and dodecanethiol MPCs. Typical approach curves, I_T *vs*. L, for each of the alkanethiol MPCs are presented in Figure 4.9. The curve obtained from the mass transfer limited model as given by Bard *et al*. is also presented. The approach curves of the alkanethiol MPCs exhibited currents that were substantially lower than the mass transfer limited model; therefore, the transfer of electrons was kinetically limited.[73] Each curve was then fitted to a $I_{T(ll)}$ curve from Equation 4.40 to determine the kinetic rate of electron transfer, k_f, for each MPC.

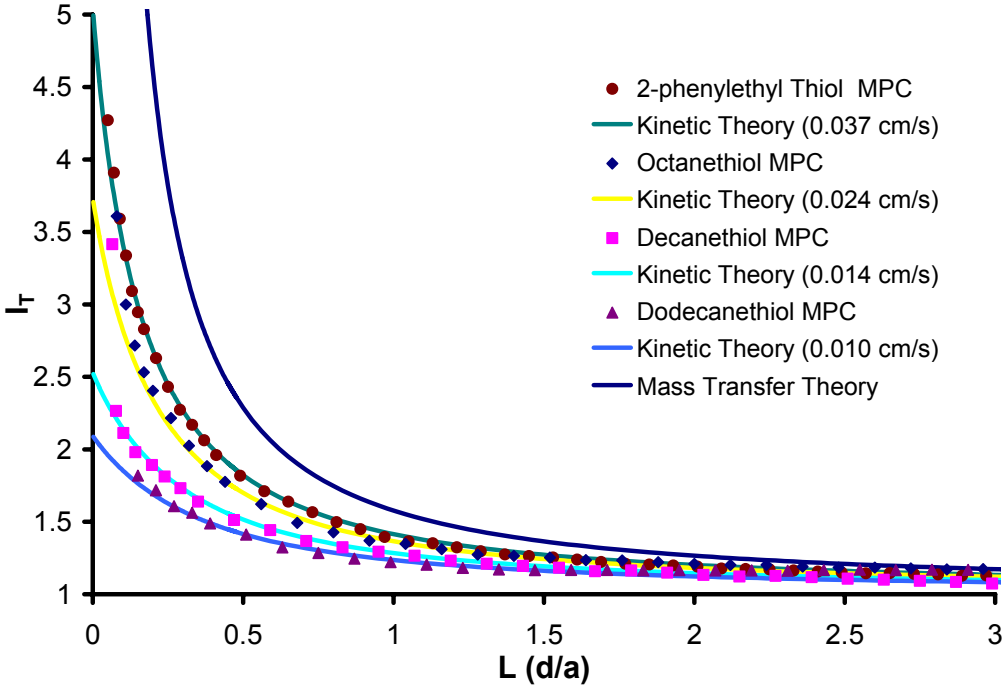

Figure 4.9 Typical SECM approach curves of octanethiol, decanethiol, dodecanethiol, and 2-phenylethyl thiol MPCs. The curves were obtained with a 10 μm Pt UME, a 2 mm Pt substrate electrode, Ag/Ag^+ non-aqueous reference electrode, and a Pt wire counter electrode. The samples consisted of 20 mg of sample in 5 mL of 0.1 M $TBAPF_6$ in CH_2Cl_2.

The fitted curves closely match the actual data until the tip approached the substrate electrode to a distance of ~100 nm ensuring a good approximation of k_f (presented in Table 4.1). It was found that the k_f decreased as the alkanethiol chain length increased, *i.e.*, the decanethiol MPCs with a chain length of 1.02 nm had a k_f of 0.024 ± 0.003 cm/s, the octanethiol MPCs with a chain length of 1.27 nm had a k_f of 0.011 ± 0.002 cm/s, and the dodecanethiol MPCs with a chain length of 1.52 nm had a k_f of 0.0048 ± 0.0008 cm/s. This indicates that the longer thiol chains insulated the metallic core better than the shorter thiol chains, therefore retarding the electron transfer. This correlates with previous studies that demonstrated a decrease in the electron transfer rate with increasing thiol lengths indicating a tunneling mechanism for the electron transfer.[39,65] The decreased k_f of the longer chain thiol monolayers indicates that the thiol had a high resistance to the electron transfer. The apparent dependence of the forward heterogeneous rate constant on the length of the alkanethiol chain could permit for the use of thiols as circuit elements in molecular electronics in which the thiol length would allow for its resistance to be directly controlled.

Table 4.1 Comparison of thiol ligand length and electron transfer rate k_f for the organic soluble MPCs showing the decrease in electron transfer rate with an increase in thiol length. The potential range of the tip was 0.2 to 1 V.

MPC	Ligand Length (nm)[33]	k_f Rate (cm/s)
Hexanethiol	0.77	0.11 ± 0.026
2-Phenylethyl Thiol	-	0.035 ± 0.001
Octanethiol	1.02	0.024 ± 0.004
Decanethiol	1.27	0.011 ± 0.002
Dodecanethiol	1.52	0.0048 ± 0.0008

The decrease in electron transfer rate for longer protecting thiol molecules correlates well with a recent SECM study which demonstrated that the rate of electron transfer through a monolayer of pentadecanethiol on a two-dimensional surface was 3.7 x 10^{-4} and 1.0 x 10^{-3} cm/s using two different electrochemical mediators.[76] While two-dimensional surfaces typically have better packed monolayers (more rigid packing leading to less pinholes), they can be used to compare to three-dimensional surfaces. The correlation between the two and three-dimensional surfaces indicates that the values given in this study are reliable. Additionally, the use of different mediators had a large impact on the electron transfer rate observed for the two-dimensional surface. The use of the SECM to determine the electron transfer properties of MPC with the nanoparticles acting as the redox mediators in this study eliminates the any possible errors resulting from an external mediator.

4.4.2.4 2-Phenylethyl Thiol MPCs

An SECM approach curve of 2-phenylethyl thiol MPCs is shown in Figure 4.9. As shown previously, it was expected that conjugated thiol MPC would exhibit a faster electron transfer rate than the alkanethiol MPCs because the probability of electron tunneling is proportional to $\exp(-\beta x)$.[110] Creager *et al*. have shown that β is smaller for conjugated molecules than for aliphatic molecules.[127] The hexanethiol molecule is similar in length to that of the 2-phenylethyl thiol, a partially conjugated thiol; therefore, it was expected that the 2-phenylethyl MPC would have a rate of electron transfer at least as fast or faster than the hexanethiol MPC. Unfortunately, the electron transfer rate for the 2-phenylethyl thiol MPCs was found to be 0.035 ± 0.001 cm/s which is much lower

than the rate of 0.11 ± 0.026 cm/s for the hexanethiol MPCs (Table 4.1) and only slightly faster than the electron transfer rate through octanethiol MPCs which is 0.024 ± 0.004 cm/s. This indicates that the phenyl ring did not enhance the electron transfer but in fact slowed the rate of electron transfer. In order to explain this, the orientation of the 2-phenylethyl thiols on the gold metallic core was considered in order to determine if it played a role in the rate of the electron transfer rate.

It is believed that the slower electron transfer rate of the 2-phenylethyl thiol is due to the difference in the orientation of the thiol on the MPC surface. It has been shown by Laibinis *et. al* that alkanethiols typically orient with a tilt angle of 26-28° from the surface normal of a gold substrate on a two dimensional SAM.[128] It follows that the alkanethiols would orient similarly on the three dimensional surface of the MPC. While there have been no reports as to the orientation of 2-phenylethyl thiol on a two or three-dimensional surface, the role of the molecular backbone was studied by comparing the orientation of 4-mercaptobenzoic acid and 4-methyl-4′-mercaptobiphenyl which are similar in length. It was found that the phenyl thiol tilt angle had an upper limit of 19° which is smaller than the tilt angle of alkanethiols. The smaller tilt angle resulted because the phenyl molecules do not need to tilt to the same degrees as alkanethiols to maximize their van der Waals interactions.[129] A smaller tilt angle would result in a slower electron transfer rate for the 2-phenylethyl thiol MPCs than for the hexanethiol MPCs of a similar length because of the longer effective distance required for electron transfer. The effect of aromatic groups on electron transfer warrants more investigation via additional phenyl terminated MPCs including completely conjugated thiols.

4.4.3 Comparison with the Butler-Volmer Model

Surprisingly, it was found that rate of electron transfer for MPCs was not dependent upon the potential of the electrode as expected from the Butler-Volmer electrochemical model which was described in Chapter 4.2.3.[73] The Butler-Volmer model states that the electron transfer rate should increase with an increased electrode potential. Figure 4.10 shows the expected linearity for the Butler-Volmer model and the hexanethiol MPC, 5 μm UME, trend of the forward heterogeneous rate constant. From this it becomes clear that the MPCs did not exhibit the expected increase in rate but rather a general decrease in rate during the application of increased electrode potentials. The remaining organic soluble MPCs showed a similar relationship to the electrode potential. This shows that the MPCs do not follow the Butler-Volmer model of electrode kinetics because of their lack of a single $E^{0\prime}$ value.

In contrast to the Butler-Volmer model in which the number of electron transferred is assumed to be one, MPCs undergo multiple electron transfer steps as apparent from the QDL charging peaks. The multiple oxidation steps of the nanoparticles result in multiple standard redox potentials, $E^{0\prime}$s, and account for the deviation from the Butler-Volmer model. In the Butler-Volmer model of a one electron processes, the application of an increased electrode potential, relative to the standard redox potential, causes the rate of the electron transfer to increase. In the case of MPCs, each redox state has a standard redox potential, $E^{0\prime}_n$. The increased electrode potential will not result in a larger value of $E - E^{0\prime}_1$, but instead will encounter another standard redox potential, $E^{0\prime}_2$, for the system. Therefore, the application of an increased electrode potential does not

result in an increase in the rate of electron transfer but must drive the transfer of multiple electrons into the metallic core of the nanoparticle.

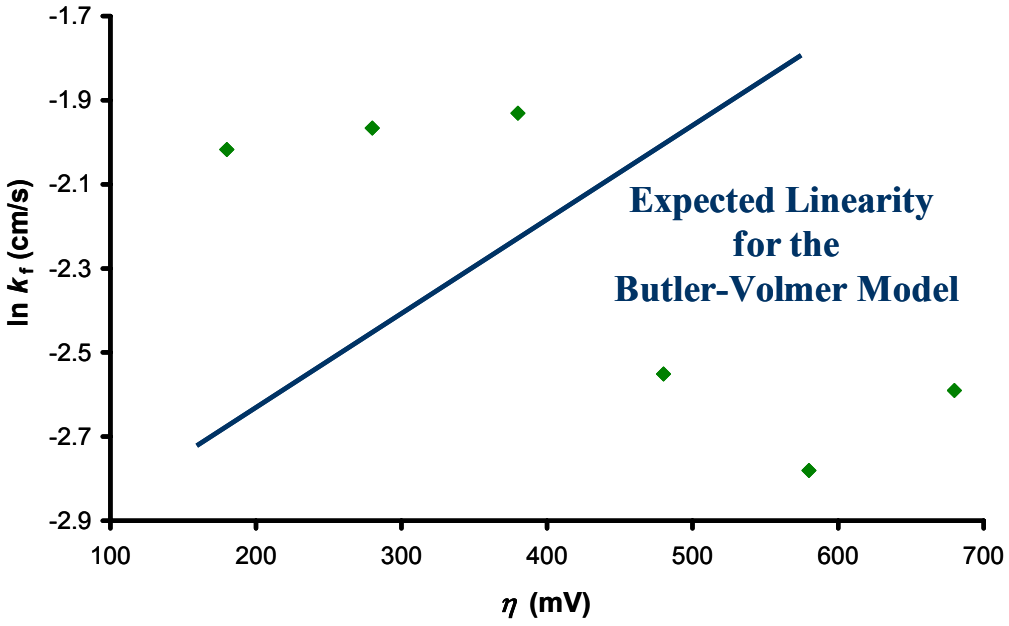

Figure 4.10 Plot of ln k_f versus overpotential for hexanethiol Cut B MPCs in order to evaluate the electrode kinetics of MPCs. The heterogeneous rate constant was obtained using Equation 4.40 via SECM approach curves of 20 mg of MPC in 5 mL of 0.1 M $TBAPF_6$ in CH_2Cl_2. The slope of the plot is not positive as expected following the Butler-Volmer model.

4.4.4 Tafel Relationship of MPC Charging

The Tafel relationship, shown in Chapter 4.2.3, allows the determination of the exchange current, i_0, and transfer coefficient, α. Figure 4.11 shows the Tafel plot, log i vs. η, for the hexanethiol MPCs. The intercept was used to determine the exchange current of 4.4 ± 1.4 pA. The slope of the curve was used to determine the transfer coefficient, α, of 0.65 ± 0.03 which is between the typical values of 0.3 and 0.7.

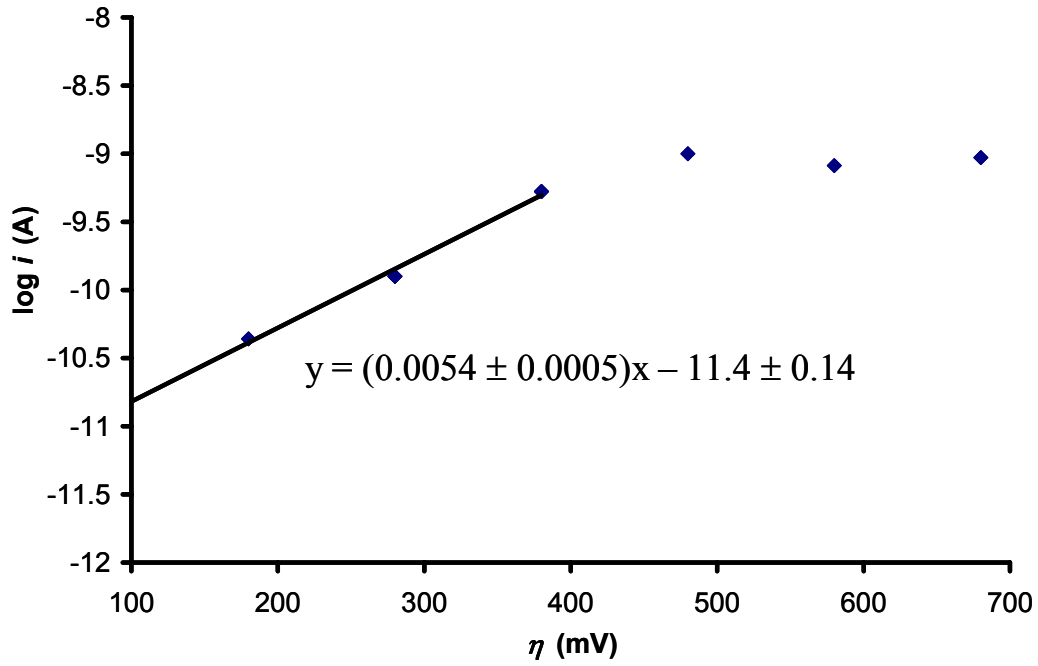

Figure 4.11 Tafel plot, log *i* versus η, for hexanethiol Cut B MPCs. The current plotted was the steady state current obtained from SECM approach curves when the tip was far from the substrate. The sample consisted of 20 mg of MPCs in 5 mL of 0.1 M $TBAPF_6$ in CH_2Cl_2.

4.4.5 Tunneling Charge Transfer

As described previously, the probability of tunneling is used to evaluate to likelihood an electron will tunnel through a material. The probability of electron tunneling is proportional to the distance of the electron transfer, *x*, and the distance factor for the extended charge transfer, β, which is dependent upon the nature of the medium and the energy barrier. It has been shown previously, the electron is transferred *via* tunneling if the conductivity decreases exponentially with an increase in chain length.[39] Therefore, the heterogeneous rate constant can be used to evaluate β as shown in Figure 4.12. For the organic soluble MPCs β was found to be 0.41 ± 0.05 $Å^{-1}$ which is lower than that shown previously for SAMs of saturated molecules indicating that the effective

tunneling length, *x*, must be shorter for the MPCs than for SAMs. The MPC is a 3-dimensional surface allowing the thiols to be more flexible than in a 2-dimensional surface. This could bring about a higher tilt angle from the surface normal of the substrate resulting in a smaller distance between the metal surface and the electrolyte solution than for 2-dimensional surfaces. This smaller distance gives rise to a higher probability for the electron transfer and thus, a faster electron transfer rate.

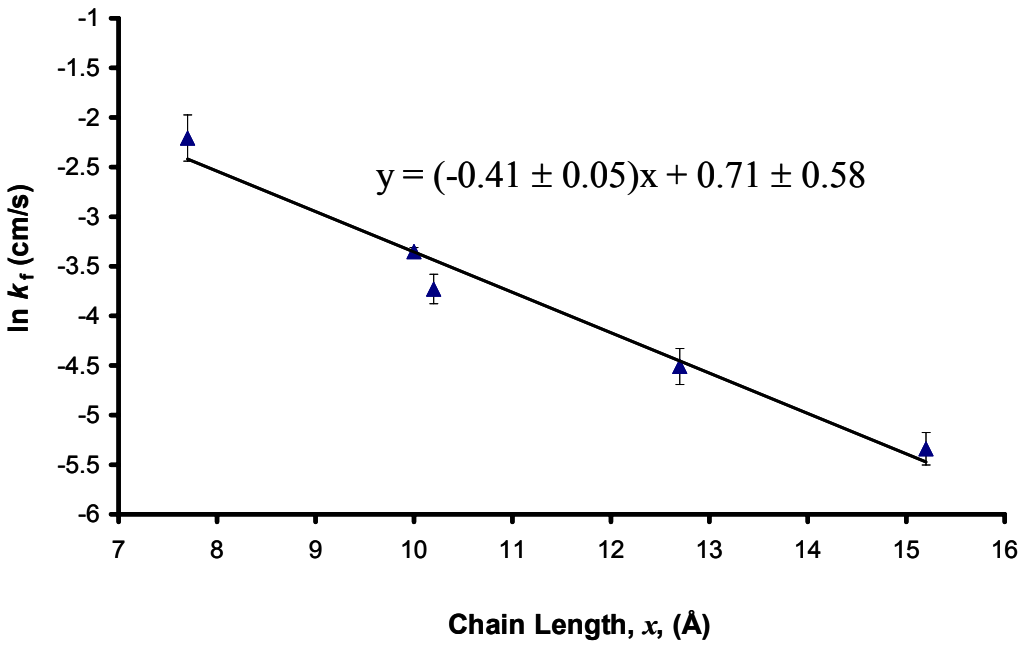

Figure 4.12 Plot of ln k_f versus chain length of each of the organic soluble MPCs to determine the probability of tunneling.

4.5 Conclusions

A novel method for measuring the electron transfer rates through the thiol monolayer of three-dimensional MPCs was developed. The alkanethiol MPCs showed positive feedback curves allowing their electron transfer properties to be investigated. The hexanethiol, octanethiol, decanethiol, dodecanethiol, and 2-phenylethyl thiol MPCs

showed kinetically limited approach curves and consequently their forward heterogeneous rate constant, k_f, was determined. The partially conjugated 2-phenylethyl thiol MPCs did not result in an increase in electron transfer rate as expected due to an increase in the actual tunneling distance of the electron. It was shown that as the alkanethiol length increases the rate of electron transfer decreases which is consistent with the tunneling mechanism for the electron transfer proposed previously.

The electron transfer rate did not increase with an increased electrode potential as expected from the Butler-Volmer model of kinetics. The MPCs deviated from the Butler-Volmer model because the model is defined for one-electron processes and MPCs are known to have multiple redox states. The exchange current of 4.4 ± 1.4 pA and transfer coefficient, α, of 0.65 ± 0.03 was found using a Tafel plot. The β, proportional to the probability of tunneling, for the alkanethiol MPCs was found to be 0.41 ± 0.049 $Å^{-1}$ which is less than shown previously for alkanethiol molecules on SAMs. This shows that the thiol molecules do not orient the same for MPCs as 2-dimensional SAMs.

CHAPTER V

WATER SOLUBLE MONOLAYER-PROTECTED GOLD CLUSTERS AS PH SENSITIVE REDOX MEDIATORS IN SCANNING ELECTROCHEMICAL MICROSCOPY

5.1 Introduction

Water-soluble MPCs are of particular interest as platforms of biological and immunological sensing.[130] Voltammetry of water-soluble MPCs has never revealed QDL charging peaks similar to those exhibited by alkanethiol MPCs which indicates they may not store charge or may charge via a different mechanism than alkanethiol MPCs.[131] SECM approach curves were used to investigate electron transfer properties of glutathione and TMA MPCs in addition to examining the effect of pH on the electron transfer properties of water-soluble N-(2-mercaptopropionyl)-glycine (tiopronin) Au MPCs.

5.2 Results and Disscusion

5.2.1 SECM Approach Curves of Water-Soluble MPCs

As stated in Chapter 4.3, the SECM approach curves are graphed as normalized current, I_T vs distance (d/a), L, and then fitted to the theoretical models of mass transfer or kinetically limited processes as established by Bard.[73] Positive feedback approach curves that follow this theory indicate a mass transfer limited electron transfer rate, while

approach curves that deviate indicate a kinetically limited electron transfer. The extent of positive feedback is a measure of electron transfer kinetics for the MPCs.

Glutathione (Au) and TMA (Au and Pd) MPC approach curves (25 μm UME and 10 μm UME respectively) revealed very little positive feedback current even with the application of high potentials (1 V tip, 0 V substrate) as shown in Figure 5.1. Therefore the oxidation of glutathione and TMA MPCs is kinetically very slow on the SECM time scale. The k_f for the glutathione MPCs was found to be 0.0021 cm/s. This correlates well with previous cyclic voltammetry studies of glutathione MPCs in which clear oxidation waves were not observable.[132] The slow electron transfer is a result of the ionically charged protecting thiol group which causes the formation of an electronic double layer as shown in Figure 5.2. The electronic double layer creates an additional barrier to electron transfer kinetics.

In contrast, the tiopronin MPC approach curves (10 μm UME) obtained using an unbiased substrate shown in Figure 5.1 were found to follow the model of a mass transfer controlled process for oxidation of the tip and oxide reduction of the core at the substrate. The positive increase in current during the approach curves confirms that tiopronin MPCs readily undergo oxidation in their gold cores as observed previously via cyclic voltametry.[132] Additional tiopronin MPC approach curve experiments (1 V UME, 0 V substrate) resulted in a similar mass transfer limited current response as shown in Figure 5.1. Repeated approach curves at a variety of potentials are shown in Figure 5.3.

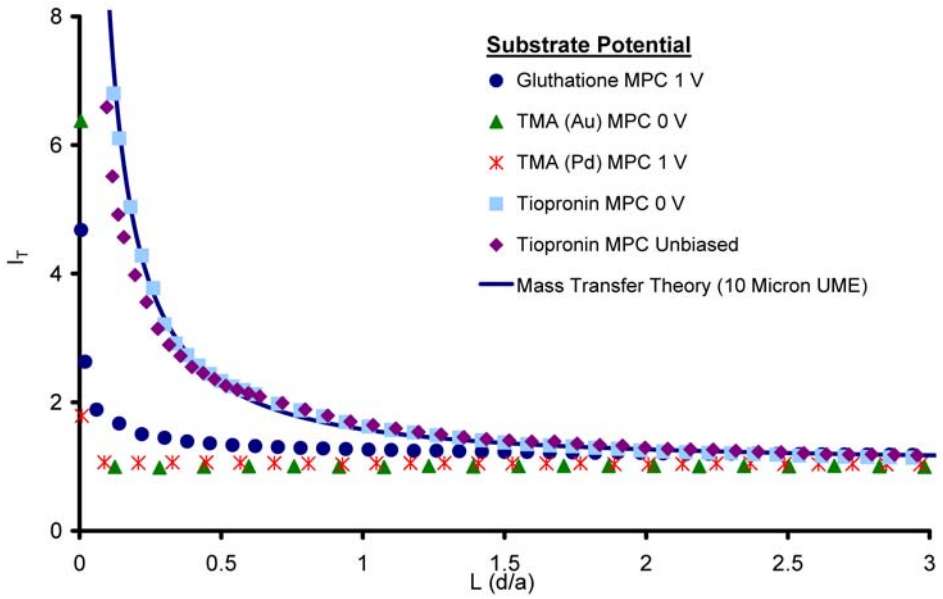

Figure 5.1 SECM (CHI 900) approach curves, Pt substrate electrode (2mm), Ag/AgCl (3M KCl) reference, 20 mg in 5 mL of 0.1 M $NaNO_3$. Glutathione MPC with 25 μm Pt UME at 1 V. TMA (Au) MPC with 10 μm Pt UME at 1 V. TMA (Pd) MPC with 10 μm Pt UME at 0 V. Tiopronin MPC with 10 μm Pt UME at 0.6 V, substrate at various potentials.

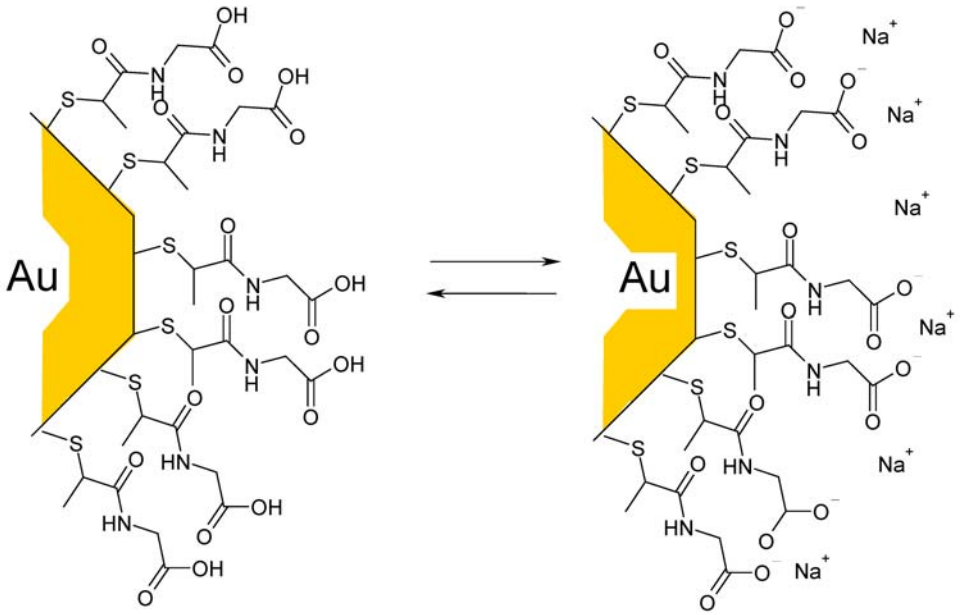

Figure 5.2 Diagram of the ionic electrical double layer of water-soluble (tiopronin) MPCs.

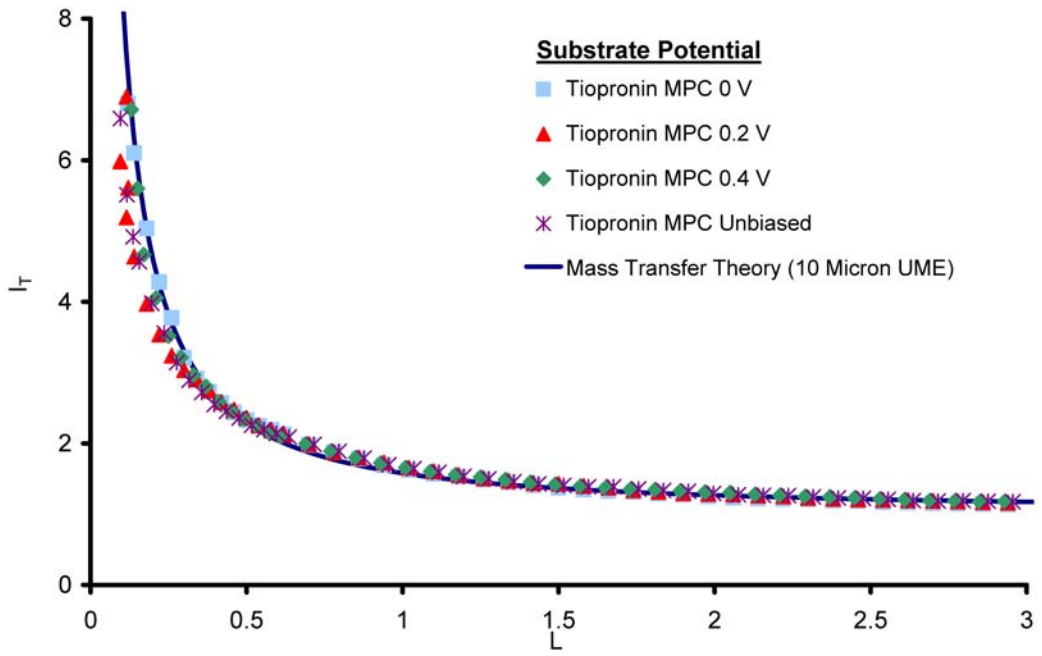

Figure 5.3 Approach curves of tiopronin MPCs at various substrate potentials with 10 µm Pt UME at 0.6 V, Pt substrate electrode (2mm), Ag/AgCl (3M KCl) reference, 20 mg in 5 mL of 0.1 M $NaNO_3$.

Tiopronin MPC approach curves obtained using a 5 µm UME, shown in Figure 5.4, allowed the kinetic rate of electron transfer to be determined. The pH dependence upon the electron transfer characteristics was also examined. The approach curves exhibited a positive increase in current when a positive potential was applied to the UME. These approach curves did not follow the theory of mass transfer which signifies a limited electron transfer rate at each of these pHs. The k_f for each of the tiopronin MPC solutions was calculated to be 0.054 ± 0.008 cm/s for pH 3 and 0.0064 ± 0.0013 cm/s for pH 9.[133] At pH 9 the pH increase resulted in an electron transfer rate decrease. This modulation of the rate is exactly opposite of that expected for the formation of gold oxide which should more easily occur in basic solutions.

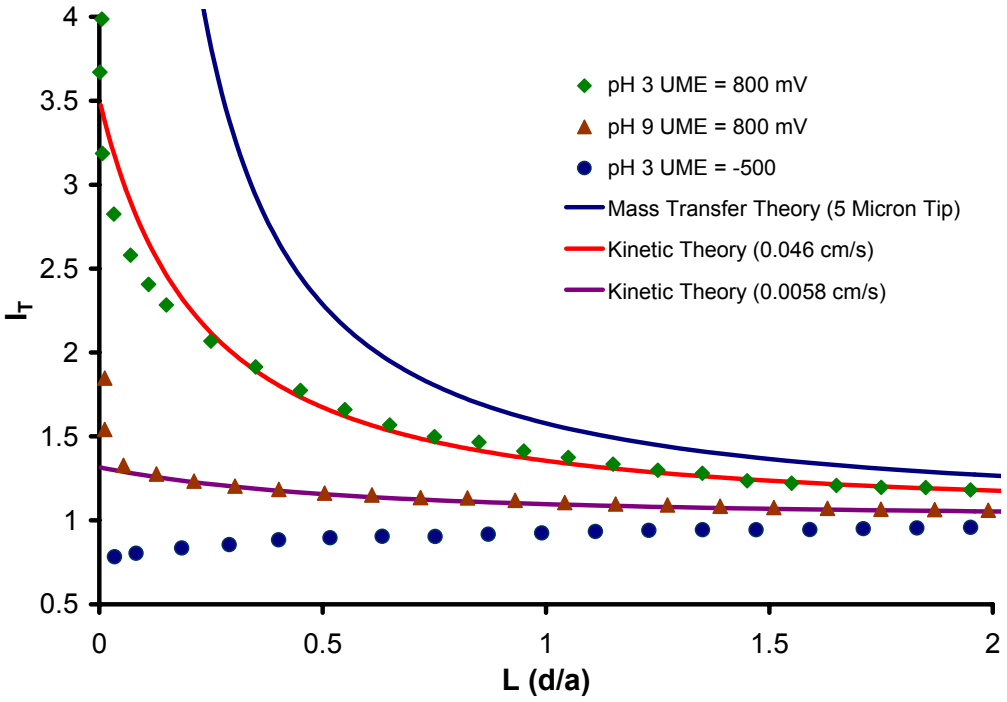

Figure 5.4 SECM tiopronin MPC approach curves, 5 μm Pt tip, an unbiased Pt substrate electrode (2mm), Ag/AgCl (3M KCl) reference, using a positively charged UME with 20 mg in 5 mL of 0.1 M $NaNO_3$ (pH 3) and 0.1 M Na_3BO_3 buffer (pH 9).

5.2.2 Gold Oxide Formation on Tiopronin MPCs

A negative feedback response in current was observed when the tip potential was below the potential required for the gold oxide formation, as shown in Figure 5.4. This is different from alkanethiol MPCs that have been shown to exhibit a positive feedback current whether a positive or negative potential has been applied to the UME.[83] Therefore, we conclude that the water-soluble MPCs do not charge in the same manner as alkanethiol MPCs. During the charging of alkanethiol MPCs, the electron is carried in the gold core of the MPC. Because tiopronin is a branched ligand, more of the inner metallic core is exposed for the tiopronin MPCs than for the alkanethiol nanoparticles. This exposed metallic core causes the tiopronin MPCs to form a metal oxide on the

surface of gold nanoparticle. The approach curves of tiopronin MPCs in sodium nitrate and sodium phosphate buffer solutions did not exhibit a positive feedback current at UME potentials less than 400 mV which corresponds with the observed gold oxide reduction at ~400 mV in these solutions. The approach curves in borate buffer showed no difference in current response over the UME 300 – 900 mV range employed which is consistent with the observed gold oxide reduction at ~200 mV for this solution. Voltammetry of tiopronin MPCs have never revealed QDL charging peaks similar to those exhibited by alkanethiol MPCs. Tiopronin MPC samples fractionated into more monodisperse samples by continuous free-flow electrophoresis have also revealed no QDL charging peaks.[131] Therefore, the formation of oxide is likely the mechanism of oxidation for other water-soluble MPCs.

5.2.3 Protonation of the Thiol Monolayer

The increase in the electron transfer rate with a lower pH is interesting as gold oxide readily forms at high pHs. This indicates that the protonation of the terminal carboxylic acid group of the tiopronin thiol monolayer is the dominant factor in the rate of electron transfer. As shown previously in Figure 5.2, the terminal carboxylic acid groups of the protecting tiopronin monolayer results in an electronic double layer. When the pH is below the pK_A (4.77 at 20 mM $NaNO_3$)[58] of the tiopronin MPCs the carboxylic acid groups are protonated and therefore the electrons can tunnel from the UME to the gold core. When the pH increases carboxylic acid groups become more deprotonated resulting in an increase in the electrical layer of negative charge around the tiopronin MPC. This inhibits the tunneling of the electron through the thiol monolayer and

therefore results in a slower electron transfer rate. Consequently, the rate of electron transfer in tiopronin MPCs can be regulated by the pH of the solution as shown in Figure 5.5. This ability to tune the rate of electron transfer should be applicable to other water-soluble MPCs that can be deprotonated and protonated, and is similar to previous STM work.[134]

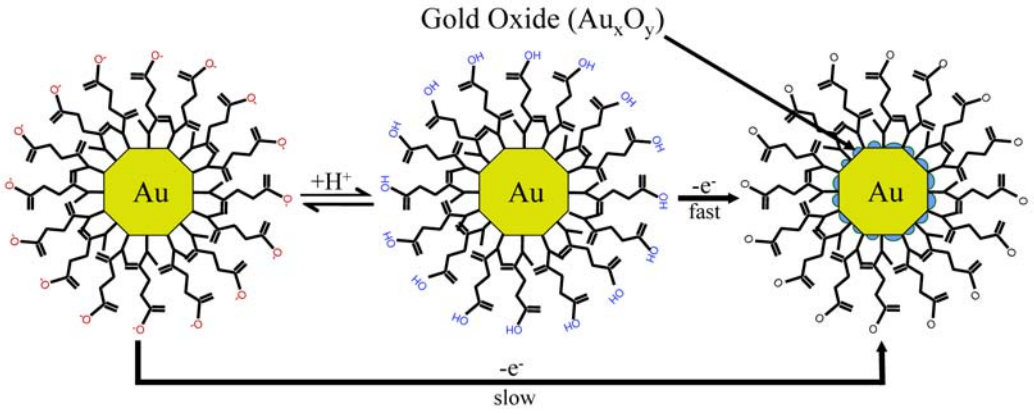

Figure 5.5 Diagram showing the electron transfer for protonated and deprotonated tiopronin MPCs.

Upon additional studies of tiopronin MPCs at pHs 5 and 7 yielded interesting results. It was expected that the electron transfer rate would decrease with the increasing pH. This was found for pH 5 as shown in Figure 5.6. The forward heterogeneous rate constant was found to 0.014 cm/s which is between that found for pH 3 and pH9 and shows a good correlation of pH to electron transfer rate. Unfortunately, the approach curve at pH 7, also shown in Figure 5.6, had almost the same positive feedback as observed for pH 3. At this point it is impossible to determine the cause of the increased positive feedback. It is possible that this result was an anomaly. Therefore, more studies

would be valuable in order to elucidate the dependence of the rate of electron transfer on pH.

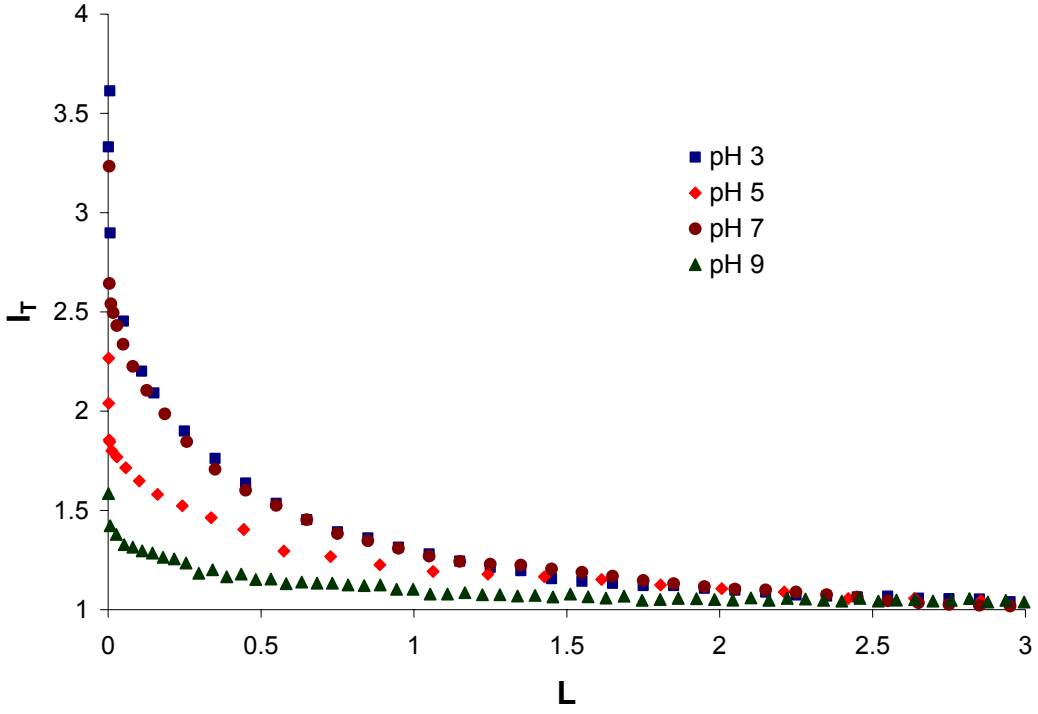

Figure 5.6 SECM tiopronin MPC approach curves, 5 μm Pt tip, an unbiased Pt substrate electrode (2mm), Ag/AgCl (3M KCl) reference, using a positively charged UME with 20 mg in 5 mL of 0.1 M $NaNO_3$ (pH 3), 0.1 M $NaCH_3CO_2$ buffer (pH 5), 0.1 M NaH_2PO_4 buffer (pH7), and 0.1 M NaH_2BO_3 buffer (pH 9).

5.2.4 MPCs as Novel Electrochemical Mediators for SECM Imaging

The use of water-soluble tiopronin MPCs was also investigated as novel electrochemical mediators for SECM imaging of a gold interdigitated array (IDA). The SECM image was conducted by using the UME to approach the IDA along the z-axis until a feedback current was 150% of i_{ss} (2.4 nA) was observed. The tip was then scanned across the IDA substrate in the x-y plane in a raster pattern that had a resolution

of 1µm. While a positive feedback of about 5.3 was observed over the conducting gold fingers, a negative feedback response of about 0.42 was observed over the insulating glass substrate as shown in Figure 5.7**.** The current for the conductive gold fingers was 11.9 times the current observed for the glass. Therefore, the tiopronin MPCs were successful electrochemical mediators for electrochemical imaging. Consequently, MPCs could be used to replace the potential specific electrochemical mediators typically used for SECM imaging. It has been shown here that pH can be used to regulate the electron transfer rates of tiopronin MPCs; therefore, SECM imaging of pH gradients on flat surfaces maybe possible using tiopronin MPCs.

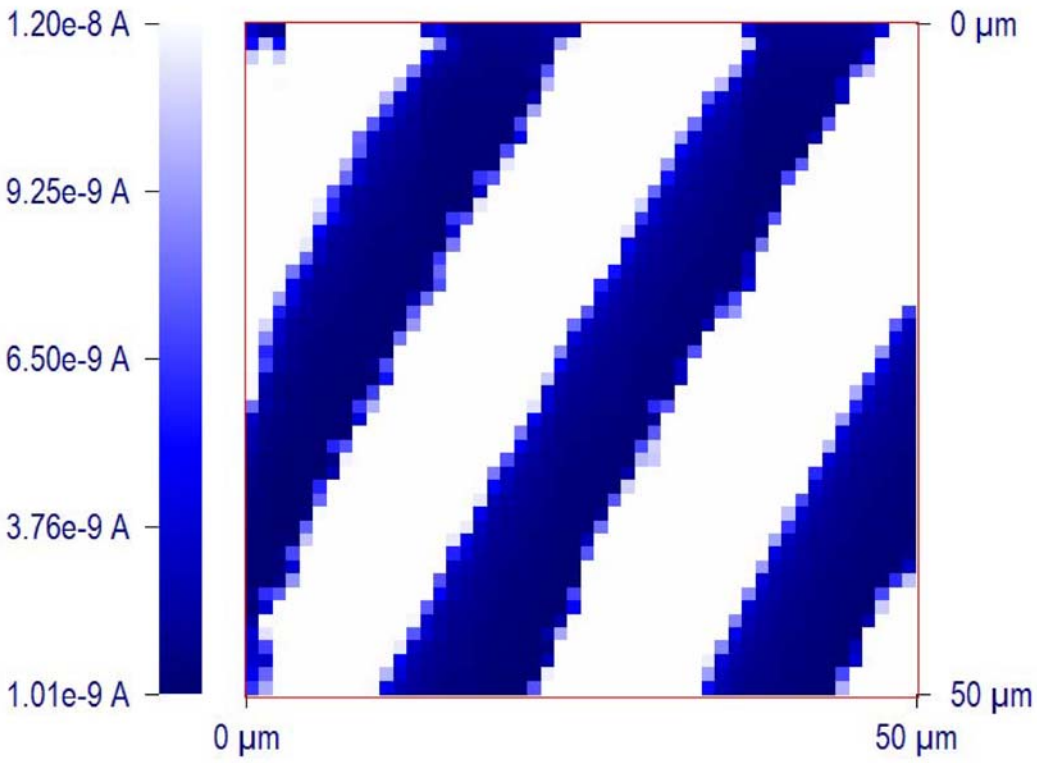

Figure 5.7 SECM image of a gold IDA substrate (0 V) using a 10 µm Pt UME (1 V vs. Ag/AgCl, 3 M KCl,) and tiopronin MPCs (20 mg in 5 mL of 0.1M $NaNO_3$) as the electrochemical mediator.

5.3 Conclusions

In conclusion, the electron transfer rate for glutathione and TMA MPCs were kinetically very slow. The electron transfer rate of the carboxylic acid terminated tiopronin MPC was found to be pH dependent in which the rate was faster when the protecting group was protonated and slower when the protecting group was deprotonated. The electron transfer rates of 0.054 ± 0.008 cm/s for tiopronin MPCs at pH 3 and 0.0064 ± 0.0013 cm/s for tiopronin MPCs at pH 9 were determined using SECM approach curves. Tiopronin MPCs were also used as a novel electrochemical mediator for SECM imaging. There was an 11.9 times difference between the current observed for the gold fingers and glass substrate indicating the use of MPCs as a novel electrochemical mediator was successful.

CHAPTER VI

CONTINUOUS FREE-FLOW ELECTROPHORESIS FRACTIONATION OF WATER-SOLUBLE MONOLAYER-PROTECTED NANOCLUSTERS

6.1 Introduction

One of the major discoveries of this research involves the use of continuous free-flow electrophoresis (CFE) as a technique to isolate monodisperse samples of water-soluble tiopronin Au MPCs. Unlike typical batch mode chromatographic processes, CFE is a continuous separation process. CFE combines the high resolving power of electrophoresis with continuous flow separations that result in large-scale quantities (0.1 g or more) of material collected into as many as 100 different fractions in less than 1 hour. A great deal of research into the development of CFE for use in isolating individual biological molecules such as proteins and cells has been reported in the literature.[135-137] NASA was especially interested in CFE as a method of separation in a low gravity environment.[138] CFE has also been used to fractionate native latex polystyrene nanoparticles on the microscale, but to date has yet to be applied to the isolation of macroscopic quantities of monodisperse nanoparticles.[139] A review of the typical CFE instrumentation is available.[140]

An instrumental schematic of fractionation of MPCs by the CFE is shown in Figure 6.1. In CFE, the sample is pumped in the presence of a buffer through an analytical column while a perpendicular electric field induces the migration of ions towards the walls of the column. As shown in Figure 6.1, the anode is on the left while the cathode is on the right. During the fractionation of the MPCs, the sample is input

near the cathode and the particles migrate towards the anode. Because CFE is a continuous process all the collected samples are obtained at the same time. CFE fractionates analytes based on their electrophoretic mobilities (μ_{ep}):

$$\mu_{ep} = \frac{|z| q_o}{6\pi\eta r} \tag{6.1}$$

where z is the ionic charge, q_o is the charge of an electron, η is the viscosity of the solution, and r is the radius of the particle, therefore the smaller the radius, the higher the electrophoretic mobility.[140] The tiopronin molecules protecting the water-soluble MPCs are terminated in a negatively charged carboxylic acid group. Therefore, it was expected that the smaller particles with the higher electrophoretic mobility would move faster and be collected closer to the anode while the larger particles would move slower and thus be collected closer to the cathode.

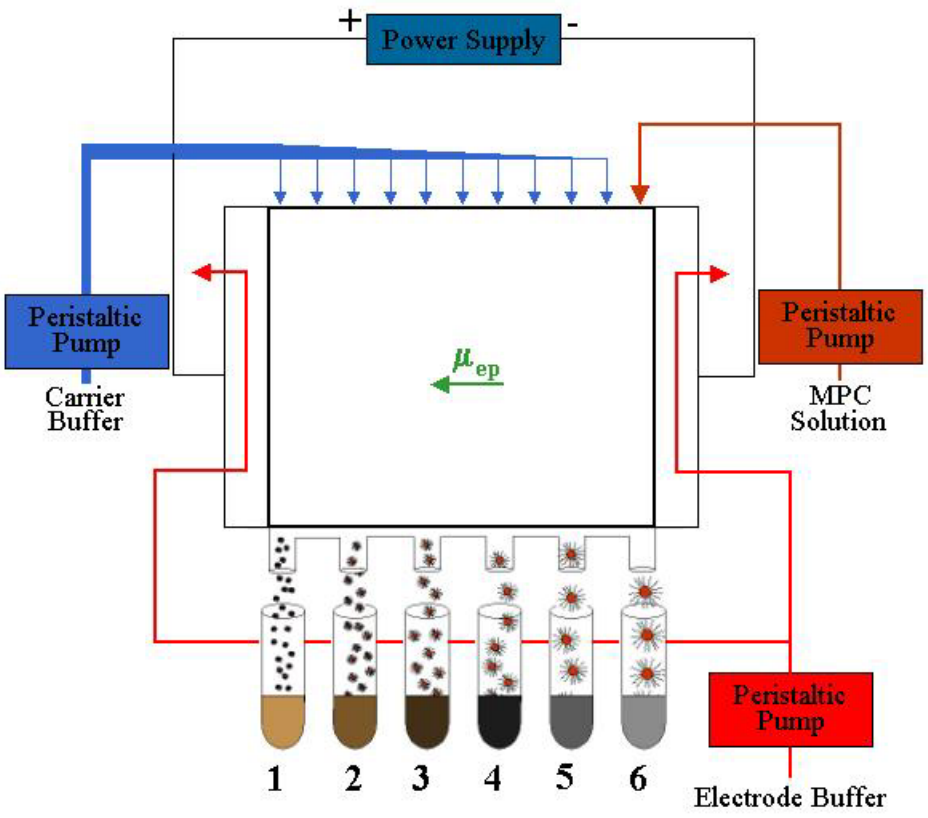

Figure 6.1 A schematic of the CFE fractionation of water-soluble MPCs.

6.2 Results and Discussion

6.2.1 CFE Fractionation Using Method 1

This initial fractionation (Method 1) demonstrated that CFE successfully isolated MPCs of differing sizes. CFE fractionates analytes based on their electrophoretic mobilities and, as previously explained, the smaller MPCs were expected to be collected near the anode while the larger MPCs would be collected near the cathode. This expected result was confirmed experimentally via the SPR bands for the fractions as shown in Figure 6.2. The 6 samples to reveal MPCs from the initial run were diluted to

have the same absorbance of 0.4 at 300 nm. Sample vials 28 (not shown) and 29 (the bottom curve) showed no SPR band indicating MPC particle diameters of 2.5 nm or less, while sample vial 33 showed a significant SPR band at ~530 nm indicating MPC particle diameters of 2.5 nm or more.[33] This demonstrates that the initial separation of the water-soluble tiopronin Au MPCs into more monodisperse fractions using CFE was successful and that CFE could be optimized in future fractionation procedures.

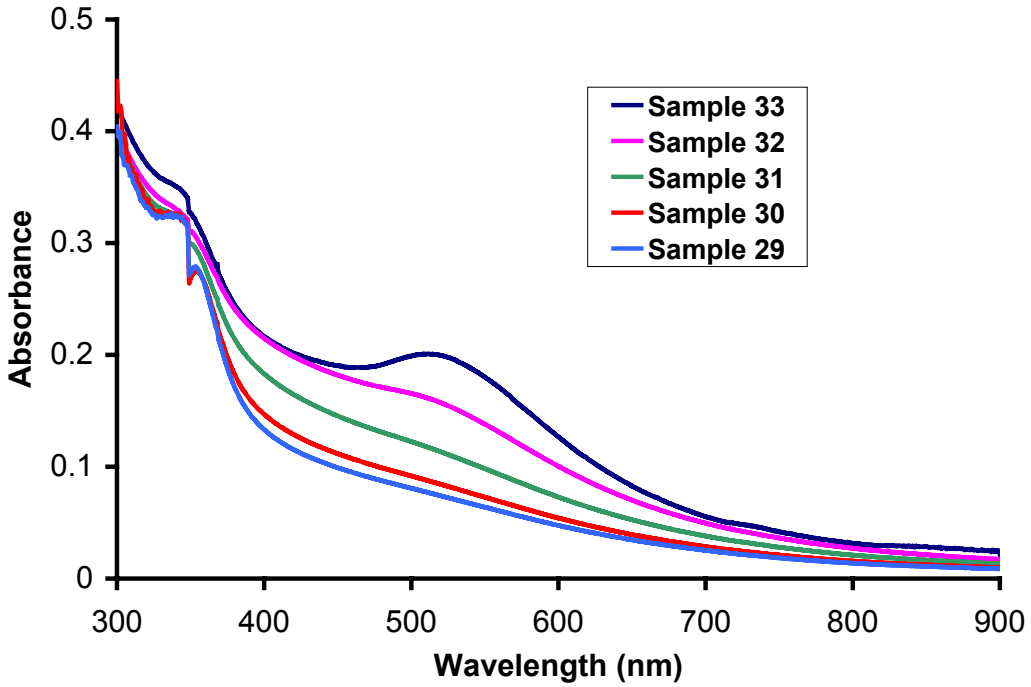

Figure 6.2 UV-visible analysis, 300 to 900 nm, of the CFE separated tiopronin protected MPCs from Method 1. The absorbance for each of the samples was normalized at 300 nm.

6.2.2 CFE Fractionation Using Method 2

In order to achieve a better fractionation of the MPC sample, some of the parameters were optimized. The new parameters resulted in a better MPC fractionation

distribution. The change in pH from 7.0 to 8.7 increased the deprotonation of the terminal carboxylic acid functional group of tiopronin. This increased the formal and effective charge states of the tiopronin MPCs and thus increased their electrophoretic mobilities. The change in electrophoretic mobility resulted in a better distribution of MPCs across the collection vials. Additionally, this tris-borate buffer had a conductivity of 78 μS compared to 2660 μS for the phosphate buffer. Reduction in the conductivity of the running buffer resulted in a smaller electrophoretic current. The smaller electrophoretic current caused less joule heating of the buffer and consequently led to a more laminar flow pattern and increased fractionation efficiency. Therefore, the control of the running buffer conditions such as pH and conductivity allowed for the optimization of CFE fractionation.

The use of the optimized parameters (Method 2) resulted in visible color in 3-36 of the 48 collected vials demonstrating the presence of MPCs. The large number of colored vials indicated a good anodal migration of the MPCs that yielded widely spread MPC fractionation. Figure 6.3, a photograph of the CFE fractionated tiopronin MPCs, showed visible color progression across the series of collection vials. The intensity of the vials only signified the amount of collected MPC particles, while the variation in shade indicated a change in the size of the MPCs collected. It was previously demonstrated that a brown colored MPC solution indicated smaller diameter particles, while a red colored MPC solution indicated larger diameter particles.[33] In Figure 6.3, the brown colored MPCs are easily observed while the red colored are more difficult to see as the digital camera image does not clearly show the faint red hue of the later vials because the MPCs

were very dilute. Therefore, the different fraction colors reflected narrower particle dispersities than in the unfractionated tiopronin MPC.

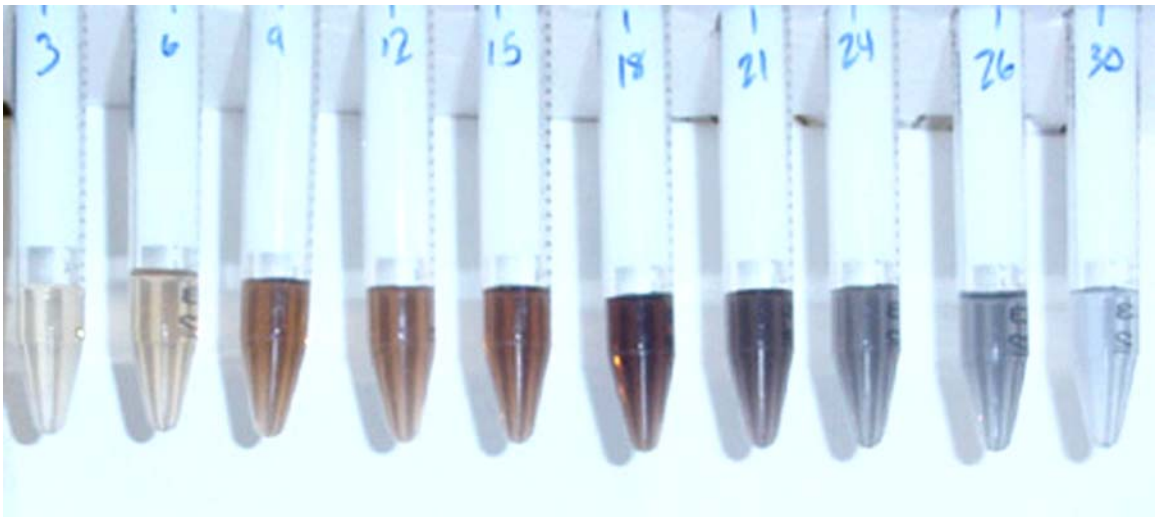

Figure 6.3 Photograph of some tiopronin MPC samples in the range from vial 3-30 from Method 2. The change in the color across the vials indicates a change in MPC size.

As stated previously, the techniques that have been utilized to isolate monodisperse MPC samples have resulted in limited quantities of collected analyte. The time needed to complete this CFE fractionation is on par with the time needed to conduct HPLC, CE, or gel electrophoresis. The major advantage of CFE over these other techniques is the large amount of MPCs that can be fractionated. During the optimized experiment, 40 mg of tiopronin MPCs were fractionated during only 1.5 hours. While we only ran the separation 1.5 hours, it could be run for longer periods as a continuous process resulting in even greater amounts of separated MPCs. To our knowledge, this method has produced the largest quantities of fractionated MPCs in this time frame. Therefore, CFE is a very fast fractionation method resulting in large quantities of MPCs for further analysis from a single run, making it a good method for isolating samples of

more monodisperse MPCs in order to determine the correlation between MPC size and their properties.

It is also very important for a fractionation technique to result in a high recovery of the nanoparticles. The mass distribution of the collected MPCs is shown in Figure 6.4. In general, there was a larger mass of particles collected per vial in the earlier vials (5-20). CFE fractionation of tiopronin MPCs resulted in the complete recovery of all of the injected MPCs. Previous fractionation methods, such as column chromatography and HPLC, resulted in a loss of sample due to the MPCs becoming trapped in the column stationary phase.[102-104] Additionally, the use of gel electrophoresis resulted in MPCs bound to a matrix from which it was difficult to extract the MPCs.[105] As CFE uses no column matrix, the MPCs were not trapped during the fractionation procedure. The recovered fractions were dissolved in a buffer solution and could be used as collected from the CFE technique. This indicates that the CFE technique is a very efficient method to fractionate MPCs on a milligram scale.

6.2.3 TEM Analysis of Fractionated MPCs

The TEM analysis, as shown in Figure 6.5, demonstrated a smaller dispersity in inner core diameters for the fractionated MPCs indicating that the CFE technique was successful in the isolation of more monodisperse samples of MPCs. The histogram of the unfractionated MPCs (Figure 6.6) clearly demonstrates the large particle size dispersity. The average inner metallic core diameter and particle dispersion for the CFE fractionated MPCs is shown in Table 4.1. It was found that the unfractionated tiopronin MPCs exhibited particle dispersion of ± 0.98 nm while the fractionated MPC samples exhibited

a particle dispersion of ± 0.36 nm. Also the standard error for the unfractionated MPCs was 0.10 nm while the standard error for each of the fractionated MPCs was 0.03 nm. The particle dispersions and standard errors indicate that CFE was successful in isolating MPCs samples with a smaller dispersity. It was also shown that sample 5 had an average core diameter of 1.90 nm while sample 10 had an increased average core diameter of 2.09 nm. This trend was observed for all of the fractionated samples analyzed with TEM. This increase in the average inner metallic core indicates the fractionation technique was successful as CFE separated the MPCs based on their electrophoretic mobilities.

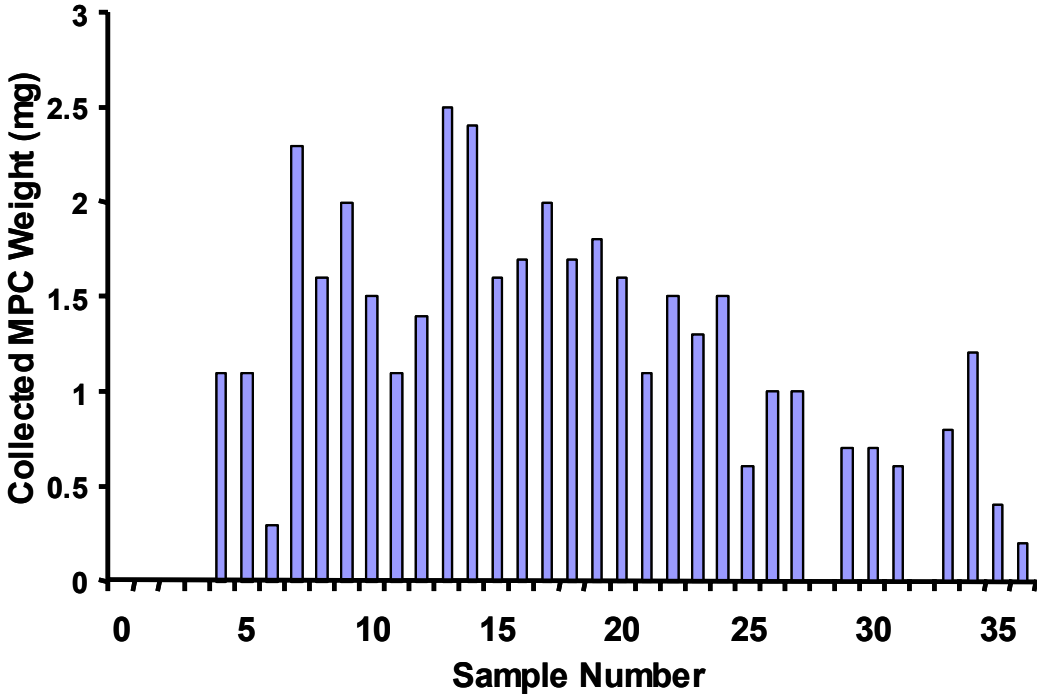

Figure 6.4 Recovery distribution of tiopronin MPCs collected from CFE fractionation. The recovery was determined by weighing the dried sample. The buffer component was subtracted from the mass of each vial. CFE demonstrated complete recovery of the MPC particles injected for fractionation.

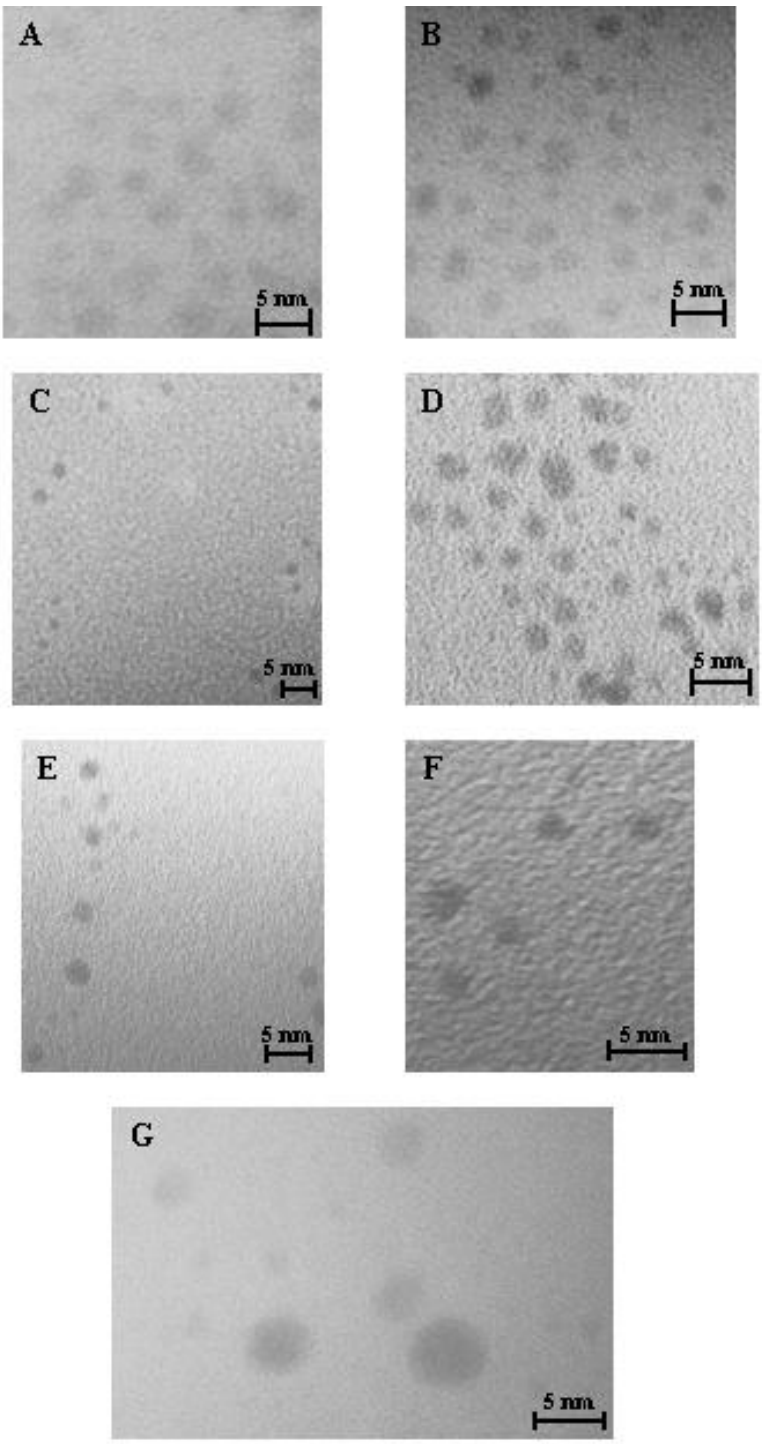

Figure 6.5 TEMs of A) Sample 30, B) Sample 25, C) Sample 20, D) Sample 15, E) Sample 10, F) Sample 5, and G) Unfractionated Sample. Large MPCs suspected of being aggregates were not included in the analysis of the MPCs.

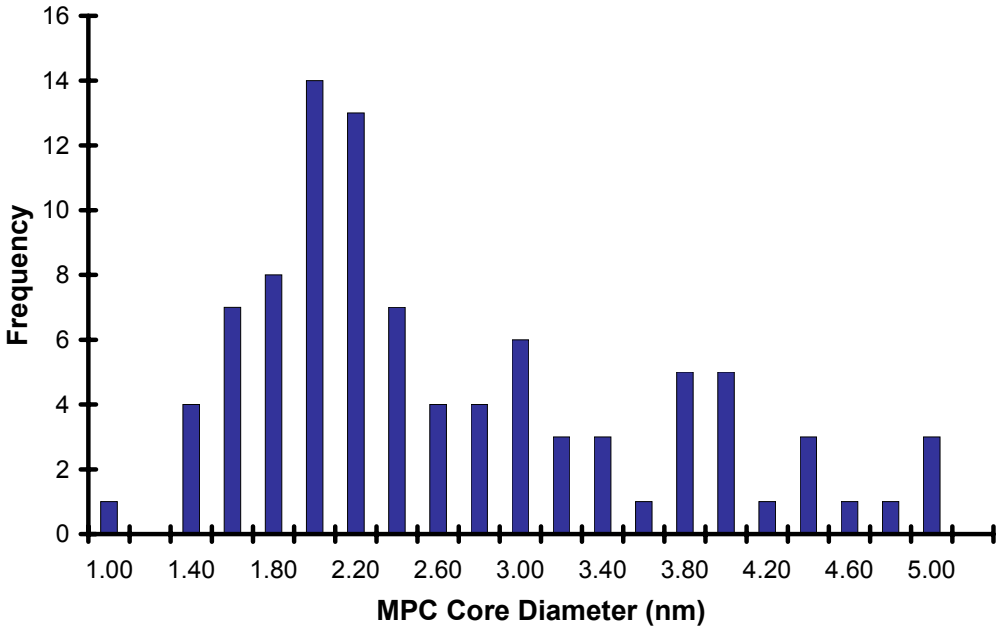

Figure 6.6 Histogram showing the particle size distribution of the unfractionated tiopronin MPCs resulting from the TEM analysis.

Table 6.1 MPC particle diameters found from the TEM analysis of the unfractionated and fractionated tiopronin MPCs (Method 2). Multiple TEMs were used in determining of the particle diameters of the analyzed MPC samples.

Sample	Mean (nm)	Standard Deviation (nm)	Number of MPCs	Standard Error (nm)
5	1.90	0.34	123	0.03
10	2.09	0.36	132	0.03
15	2.16	0.34	90	0.03
20	2.29	0.29	98	0.03
25	2.41	0.31	101	0.03
30	2.59	0.32	108	0.03
Unfractionated	2.56	0.98	94	0.10

The measurement of the monodispersity of a sample is limited by the resolving power of the technique used. In TEM, the uncertainty in particle size is a combination of TEM resolution and actual size dispersity. The typical particle dispersity of the CFE fractionated MPC was found to be ≤ 0.36 nm. This is nearly equal to the resolving power of 0.29 nm for the TEM under the best conditions. It is possible that the actual dispersity of these samples is less than that able to be resolved by conventional TEM. The increased dispersity for the smaller particles stems from the increased difficulty in focusing the image at high enough resolution. This indicates that the CFE fractionation technique resulted in MPCs samples very close to monodisperse samples of MPCs. This shows once again that the CFE fractionation was successful in isolating more monodisperse samples of MPCs and is an excellent technique to be used to fractionate MPCs on a large scale for further characterization tests.

As expected, the collected mass distribution from Figure 6.4 roughly correlated with the particle diameter distribution of the unfractionated tiopronin MPCs from Figure 6.6 and the TEM analysis shown in Table 6.1. Figure 6.4 shows that vial 15 contained a large mass of collected particles and therefore the mass of vial 15 was expected to correlate with the more frequent MPC core diameters in Figure 6.6. The particle diameter of the MPCs in vial 15 was found to be 2.16 ± 0.34 nm. This diameter correlated with the most frequent particle diameter of 2.2 nm in the unfractionated MPCs. This further signifies that the CFE fractionation technique was successful in isolating more monodisperse samples of the MPCs.

6.2.4 UV-visible Spectrophotometry of Fractionated MPCs

The UV-vis spectra shown in Figure 6.7 confirmed the visual observation and TEM analysis of the CFE fractionation. The samples fractionated using the optimized conditions were not diluted due to the very small amount of particles in some of the collection vials. The UV-vis spectra from the undiluted MPCs could not be normalized to the same scale. Samples 10 through 15 exhibited no observable SPR band indicating an MPC particle diameter of less than 2.5 nm. Samples 16-20 had a very small SPR band indicating particles around 2.5 nm. Samples 24-27 showed a substantial SPR band that indicated larger MPC particle diameters and had a deep burgundy color that faded as the particles settled with time. Fractions 27 and up showed reduced solubility within a week which also indicated that they consisted of MPCs with a large diameter. The observed SPR bands correlate well with the TEM analysis shown in Table 6.1 and verify that the CFE fractionation technique resulted in the isolation of more monodisperse MPC samples increasing particle diameter. The decreased absorbances for samples 24-27 resulted from the small number of particles collected in these vials. This confirms the mass distribution shown in Figure 6.4 that indicated very few of the MPCs resulting from this synthesis were larger than 3 nm. The UV-vis analysis of the separated MPCs substantiates that the CFE fractionation was successful in isolating fractions with smaller dispersity fractions as well as fractions of increasing particle diameters.

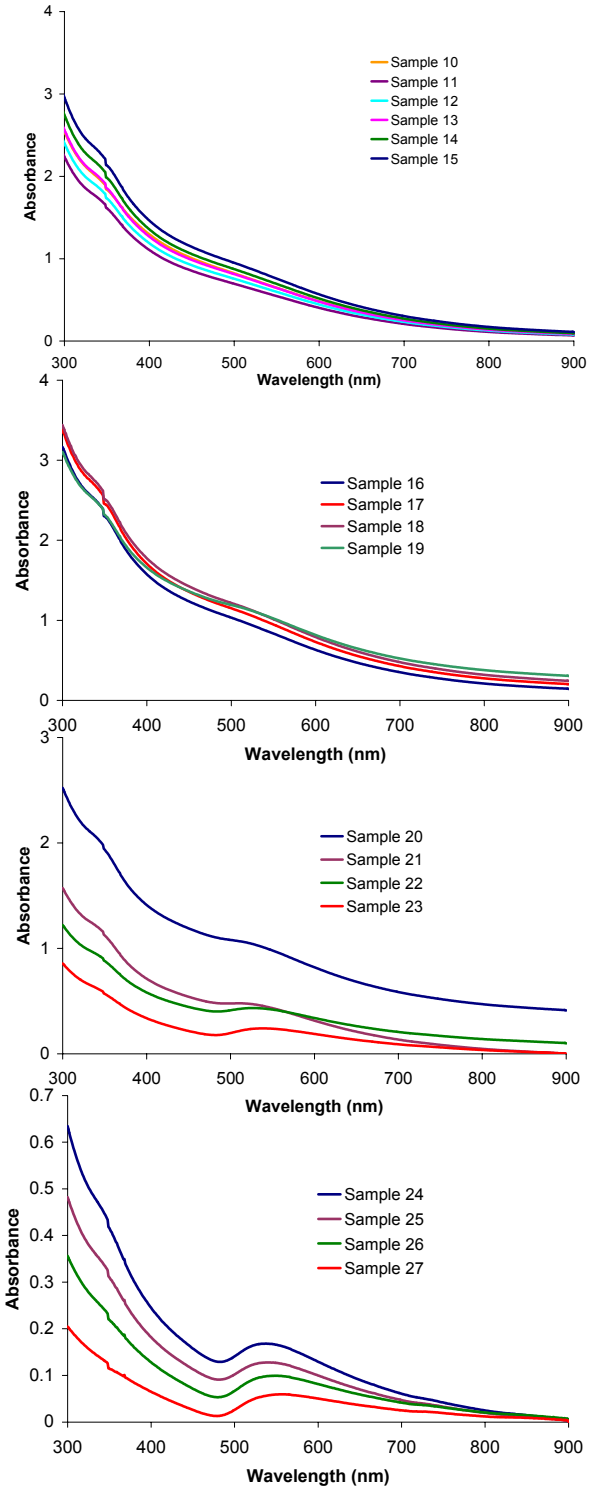

Figure 6.7 UV-Vis analysis of the CFE fractionated tiopronin protected MPC samples during Method 2. The spectra were not normalized due to the different number of particles contained in each sample.

6.3 Conclusions

In conclusion, we demonstrate that CFE is a successful method for fractionating water-soluble MPCs into more monodisperse samples. This monodispersity was determined through visible inspection, TEM, and UV-vis spectrophotometry of the isolated MPC samples. The use of CFE to fractionate MPCs resulted in a complete recovery of the nanoparticle. Additionally, the use of continuous flow fractionation resulted in larger quantities of MPCs with less dispersity than most previous methodologies, and could prove useful in generating bulk quantities of monodisperse nanoparticles for future applications. It was also shown that the MPCs were isolated into fractions whose particle dispersity was very narrow and neared the resolving power of the TEM. Further optimization of CFE fractionation should result in the fractionation of MPCs into specific sizes on the gram scale that exhibit useful properties for specialized applications.

CHAPTER VII

NOVEL CONTINUOUS FLOW ELECTROPHORESIS INSTRUMENTATION

7.1 Introduction

The development and construction of a novel CFE instrument, shown in Figure 7.1, is discussed in this chapter. The novel CFE instrument was constructed as designed in a patent donated by Boeing invented by David Richman, a Boeing/MacDonald Douglas scientist with over 30 years experience in building CFE instrumentation.

A description of a typical CFE instrument can be found in Chapter 6.1. In general, free-flow electrophoresis operates by introducing a continuously flowing sample into a carrier buffer in the presence of an electric field. The separation chamber is usually rectangular with electrodes at either side and inlet and outlet ports at either end. The electric field is perpendicular to the sample flow inducing migration of charged analytes in the direction of the field. The separated analytes are collected into fractions with outlets positioned laterally into an array of sample collection vials. Typically, an ion exchange membrane is situated between the electrodes and the separation chamber. A separate rinse buffer is employed between the membrane and electrodes to remove any gasses liberated by the electrolysis of the carrier buffer.[140]

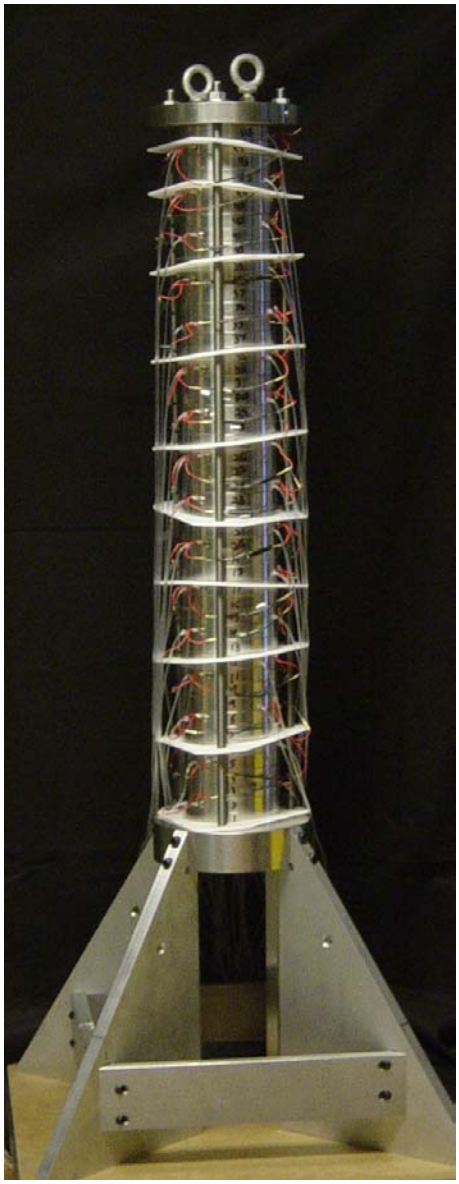

Figure 7.1 Photograph of the novel CFE. The instrument is constructed of stainless steel and consists of an inverted annular separation chamber.

7.2 CFE Innovations

The novel CFE developed in this dissertation contains many innovations that distinguish it from typical commercially available instruments. The instrument is oriented vertically with a cylindrical separation chamber. The inlet ports are at the bottom of the instrument while the stainless steel outlet ports are equally spaced along the separation chamber. The outer part of the separation chamber acts as the cathode while an inner tapered cone acts as the anode. A more detailed description of the instrument is given in Chapter 7.4.

In this instrument, the vertical column allows the analytes to separate according to their size. During the electrophoretic separation, the sample is pumped laterally up the column. The tapered inner cone results in a cross flow carrying the sample to the wall of the separation chamber and through the outlet ports. The flow separator inputs the sample at some arbitrary point from the cathode wall. The sample will travel laterally up the column with the carrier buffer until the cross flow forces the analyte into the outlet ports. The rate at which the sample travels up the column is dependent upon its size. A large sample will travel vertically more slowly due to gravity and exit the column lower than a smaller sample.

The CFE fractionates the analyte by charge via the use of the electric field. The use of a sample with a positive electrophoretic mobility will be attracted to the anode. The cross flow towards the cathode, due to the tapered separation chamber, is stronger than the flow towards the anode, due to the positive electrophoretic mobility, transporting the fractionated analytes to the outlet ports. As a result of the tapered chamber, an analyte with a high electrophoretic mobility will exit near the apex of the chamber while

an analyte with a lower mobility will exit lower along the column. Because the sample and cathode have the same charge there is no deposition of the analyte on the electrode surface.

During the electrophoretic separation, it is important that the electric field remains constant throughout the separation chamber. In a typical CFE, the separation chamber is rectangular resulting in a constant electric field due to the uniform solution resistance. Unfortunately, the tapered separation column of this novel instrument results in a decrease in the solution resistance as the analyte advances up the column. Compensation of the decreasing solution resistance is attained through the application of decreasing voltages to the cathode via an array of resistors. The resistance increases up the column to compensate for the decreased solution resistance, thus, keeping the electric field constant.

The separation chamber is uniformly tapered with the widest part at the bottom of the vertical column. The tapered chamber results in a constant centerline velocity allowing the instrument to be more resistant to convective disturbances than a rectangular chamber. Additionally, the use of a tapered separation chamber with the outlet ports distributed along the length of the chamber allows a higher resistance to gravity. Gravity, which acts perpendicularly to direction of the buffer flow, causes partially soluble analytes soluble analytes to separate out depending on the length of the column resulting in analytes slowly falling out of solution. Because this instrument is capable of high throughput, it is particularly useful for the large-scale separation of MPCs allowing for their characterization and therefore their implementation in nanotechnology.

7.3 CFE Fractionation Goals

This novel CFE will be used to fractionate MPCs into more monodisperse samples. Three of the water-soluble monolayer-protected clusters have ionic charges incorporated into their thiol structures. These three thiol groups are glutathione, TMA, and tiopronin. Using our preliminary results with tiopronin MPCs as our guide, the CFE will be used to recreate the Alpha Two fractionation. The CFE will then be used to separate the previously synthesized glutathione and TMA Au MPCs. Platinum and palladium core MPCs with these last two ligands have also been synthesized. The CFE will be used to fractionate these nanoparticles to demonstrate its utility for multiple metal cluster compositions.

Although no work has been done with CFE in non-aqueous polar solvents, as long as the conductivity of the electrophoresis elutant is kept near that of the aqueous CFE experiments, it should be possible to fractionate alkylthiol MPCs with a few charged groups exchanged onto the cluster to provide the charge. Thus, it may be possible to separate exchanged MPCs with one TMA ligand from those with two, and three and so on, which would result in more monodisperse samples of alkylthiol MPCs.

7.4 Novel CFE Description

As described previously, the novel CFE instrument contains many innovations. The bottom of the instrument begins with a stainless steel (SS) base that supports the rest of the instrument as shown in Figure 7.2. The removable inlet is inset into the bottom of the base. 48 SS rings are stacked on top of the base. These rings act as the cathode for the electrophoresis instrument. An inner tapered cylinder or cone acts as the anode for

the CFE. The widest part of the inner cone is at the top of the instrument resulting in the widest part of the separation chamber oriented at the bottom of the instrument. The inner cone is attached to the SS top, which is then bolted to the SS base by three threaded rods. Because a small displacement or tilt of the cone at the top results in a large displacement of the cone at the bottom, the position of the inner cone within the instrument is adjustable via a SS plate between the rings and the top. Six screws or bolts can be adjusted to center the cone. Eyebolts are attached to the top of the instrument, allowing easier movement of the instrument if needed.

The electrodes for the CFE were constructed using stainless steel, as the use of a relatively non-reactive material for the electrode reduces the complexity of the apparatus and eliminates pH changes near the electrodes. The gas liberated by electrolysis is then absorbed into the degassed carrier buffer. The use of a limited voltage will reduce the amount of gas produced. Because the novel instrument does not rely upon a membrane to separate the electrodes from the buffer solution, which would dissolve in organic solvents, the CFE can be used to fractionate organic soluble nanoparticles.

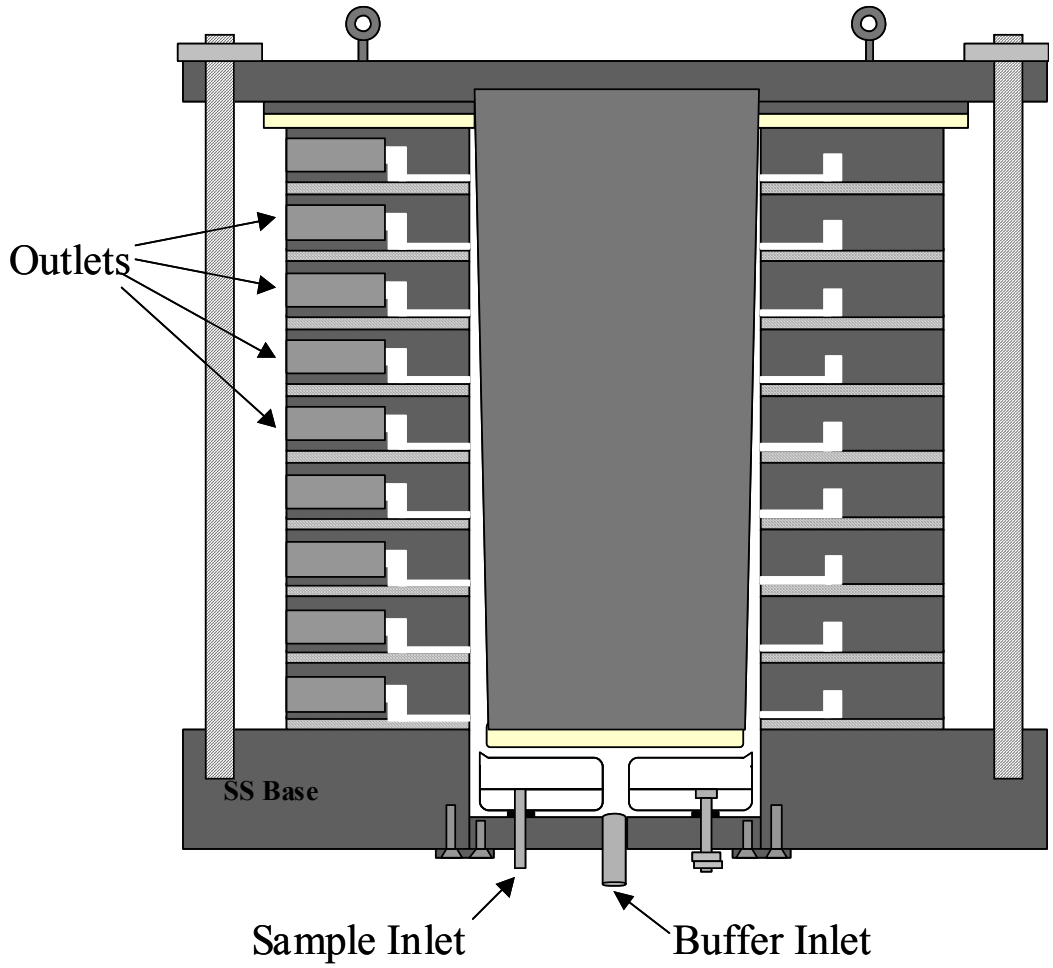

Figure 7.2 Simplified diagram of the interior of the novel CFE instrument. The actual CFE instrument contains 48 outlets. The outlets are each contained in a ring. The inlet base containing the sample and buffer inlets is removable.

The carrier buffer is pumped into the instrument by a single port while the sample is pumped in using three inlets situated 120° from each other as shown in Figure 7.3. The inlets are inset into a flow separator constructed from two pieces of acrylic joined by a double-sided adhesive film. The flow separator splits the carrier buffer into two paths as shown in Figure 7.4 and inputs the sample into one plane of the carrier buffer. The flow separator allows the analyte to be placed in one laminar phase of the carrier buffer in almost 360°.

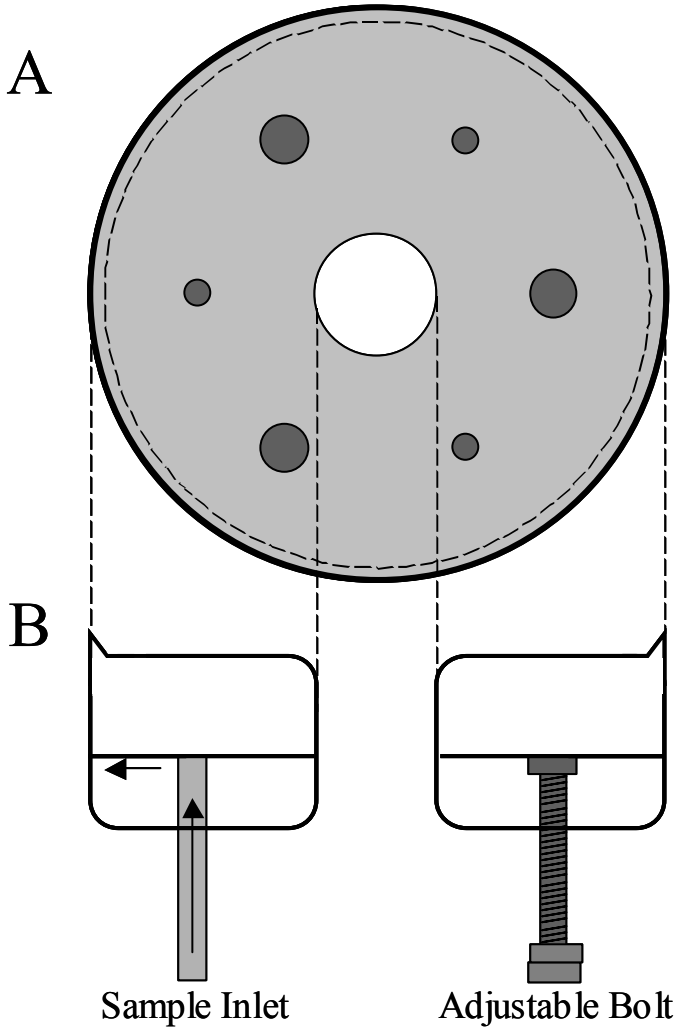

Figure 7.3 A) Top view of the flow separator with the three sample inlets set at 120° and the three adjustable bolts also set 120° from each other. B) Side view of the flow separator showing the sample inlet and adjustable bolt. The sample flows into the flow separator and then to the outside.

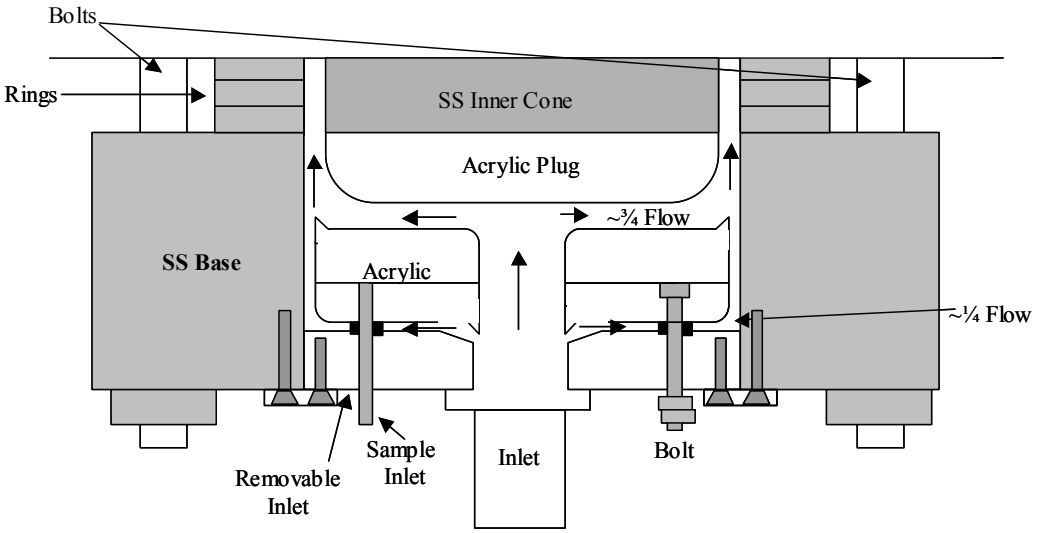

Figure 7.4 A diagram of the removable inlet with the inner SS cone and SS rings. The carrier buffer is split into two paths with the one-quarter of the flow going through the bottom path and three quarters of the flow going through the upper path.

Three adjustable bolts are also inset into the flow separator. These adjustable bolts allow the height of the flow separator to be controlled from outside the instrument. Because the flow separator inputs the sample into the carrier buffer, the bolts can be used to direct the analyte to the desired buffer plane. For example, if the analyte is placed at the outside of the first quarter of the buffer flow as shown in Figure 7.4, in the absence of an electric field, the analyte should exit the instrument one quarter of the way up the column or at approximately ring 12 due to the tapered inner cone which results in an overall cross flow towards the outlet ports. If the flow separator is positioned higher, the sample should exit further up the column.

The 48 outlets of the instrument are inset into the SS rings that act as the cathode. As shown in Figure 7.5, a slot or channel is inset into the rings with the outlet positioned at the bottom of the channel. These rings are then inverted so the channel is at the bottom

of the ring and stacked on top of the base of the instrument. The rings are attached to one another via a double-sided adhesive film. The film is removed from the channel and inner lip. The absence of the film on the inner lip allows the fractionated analyte to exit the separation chamber and enter into the ring channels. When a channel is full, the analyte then exits the instrument and flows through a tube into a collection vial. In order for the flow to travel around the channel and out the outlet port, the pressure must decrease as the sample nears the outlets. To do this the channel is deepest at the outlet port and offset so that the outlet is positioned at the furthest point from the separation chamber. The rings are oriented approximately 120° from each other along the circumference of the column because the sample inlets are also oriented 120° from each other. This orientation of the outlets allows for the flow and pressure of the column to be equalized.

As stated previously, the inner tapered cylinder or cone acts as the anode for the separation chamber. The anode is tapered to equalize the flow of the analyte. The anode is hollow to allow for a method of cooling the chamber from the inside if there is too much joule heating during separation. The bottom of the inner cone is capped at the bottom via an acrylic stopper in order to prevent leaking.

Tubes are attached to the outlet ports and lead to a box holding the collection vials. The collection vials are located above the instrument in order to obtain a constant pressure for each of the outlet ports. The constant pressure results in each of the outlets flowing at the same rate. This is essential for the instrument as the lack of a constant pressure will result in the outlets operating at different rates and could result in the inability to fill the separation chamber.

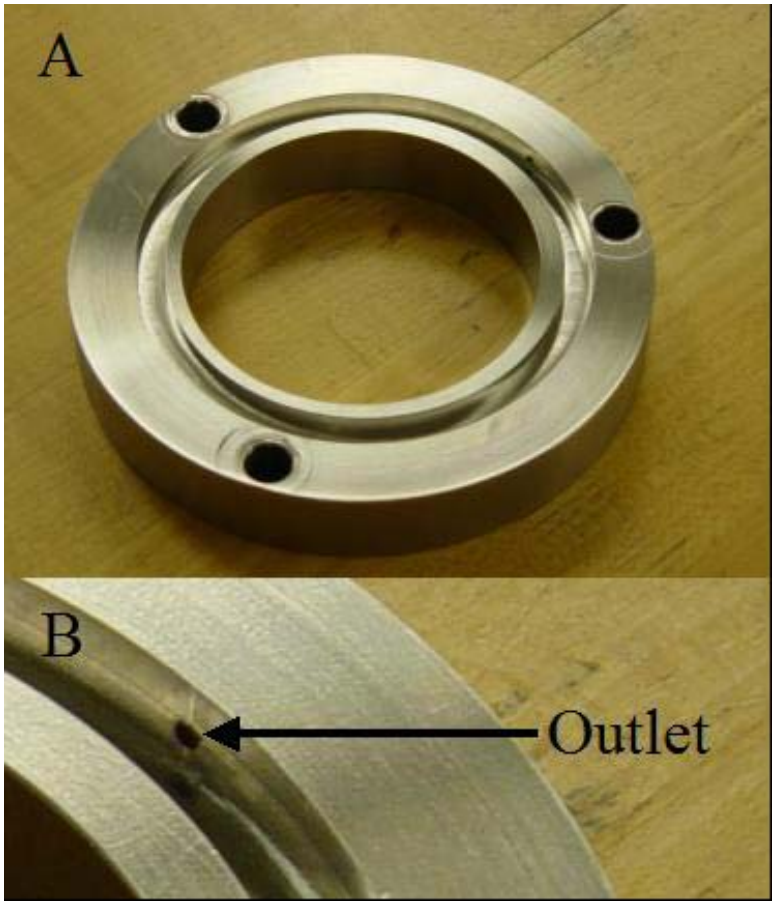

Figure 7.5 Photograph of an example ring of the CFE. This ring was an early version that was not used in the construction of the instrument. This ring has three holes that were not included in the final version and the outlet is not positioned at the bottom of the channel as in the rings used.

7.5 CFE Specifications

The detailed measurements of the base and inlet of the instrument are given in Figure 7.6. The base of the instrument is free of an electric field. The base is composed of a SS ring that is 5.07 cm in height and thickness while the outer diameter is 12.57 cm while the inner diameter is 7.80 cm.

The removable inlet consists of an inlet base, the flow separator, three sample inlet ports, three adjustable bolts, and a single carrier buffer inlet port. The inlet base is

inset into the base of the instrument as previously described. An o-ring is used to seal the inlet base to the instrument base. The inlet base is 1.27 cm in height and 7.96 cm in diameter. There are three holes through the inlet base to allow for the sample inlet ports and three threaded holes for the adjustable bolts. The carrier buffer inlet port, which has an inner diameter of 0.635 cm (1/4″), is press fitted into the inlet base with an epoxy seal.

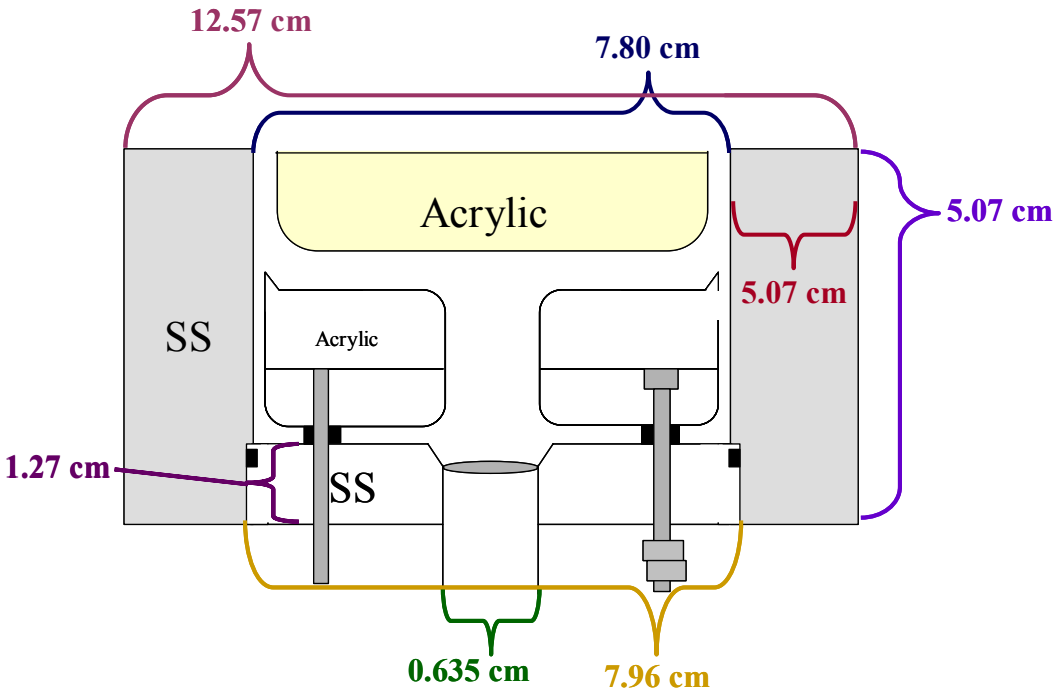

Figure 7.6 A diagram showing specific measurements of the SS base and SS removable inlet base.

The flow separator is 2.30 cm in height and 7.46 cm in diameter with a 0.635 cm inner diameter as shown in Figure 7.7. There is a lip around the top of the flow separator which is 0.19 cm in height. The three sample inlet ports and adjustable bolts are inset at the halfway point of the flow separator and go through the inlet base. The inlet ports have a 0.24 cm inner diameter and are designed for insertion of tubing with a 0.24 cm

(3/32″) outer diameter tubing with an inner diameter of 0.079 cm (1/32″). O-rings are positioned around the sample inlet ports and the adjustable bolts between the flow separator and inlet base. These o-rings prevent the inlet base from leaking at the inlets and bolts.

As described previously, the adjustable bolts allow the height of the flow separator to be positioned at the desired height for the input of the sample. Therefore, the space between the flow separator and inner cone (A) and the space between the flow separator and inlet base (B) is variable but always totals to 0.40 cm. The height of the flow separator lip is subtracted from the flow separator height.

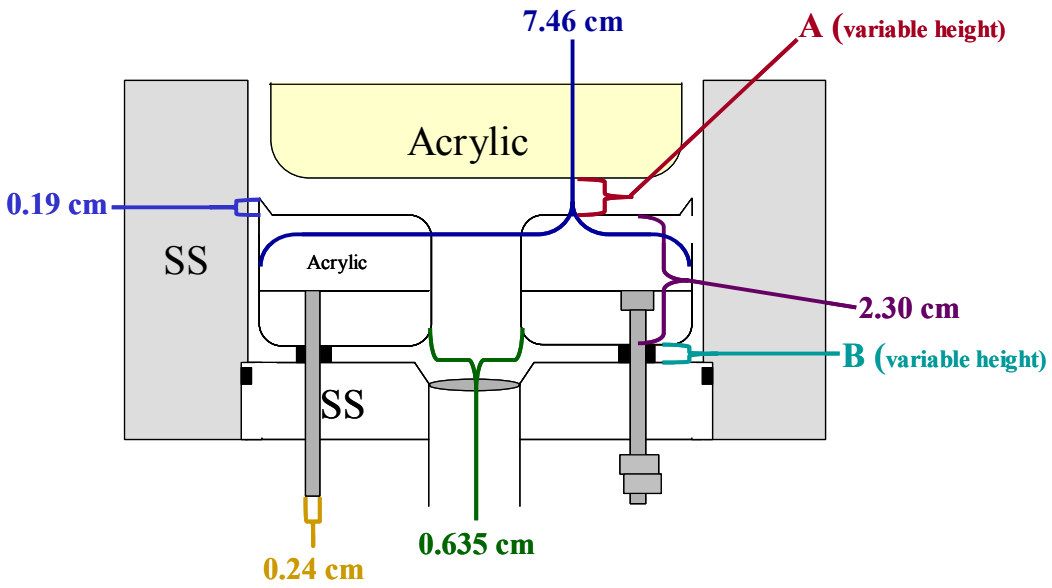

Figure 7.7 A diagram showing the dimensions of the flow separator. A and B can be adjusted to control the amount of flow above and below the flow separator with a total height of 0.40 cm. The lip at the top of the acrylic flow separator is 0.19 cm and must be included when setting the height of B but subtracted out when determining A.

A top view diagram of the rings is shown in Figure 7.8. The outer diameter of the 48 rings is 12.57 cm and the inner diameter is 7.80 cm. The slot or channel has an outer diameter of 9.77 cm while the inner diameter is 8.73 cm. The center of the channel is offset from the center of the ring by 0.022 cm. Figure 7.9 shows a side view cut away of the rings. The height of each ring is 1.84 cm while the width is 2.39 cm. The channel is deepest near the outlet with a maximum depth of 0.64 cm and a minimum depth of 0.43 cm. The outlet, having a diameter of 0.24 cm, is positioned at the deepest part of the channel and is fitted with the same tubing used for the inlet ports. The double-sided adhesive film between the rings had a 4.0 mil film coated with two 2.0 mil layers of acrylic adhesive.

The inner SS cone has a length of 89.85 cm with an inner diameter of 5.71 cm as shown in Figure 7.10. The cone has an outer diameter of 7.78 cm at the top and 6.80 cm at the bottom. The bottom of the inner cone is capped with an acrylic plug as described earlier. This plug is 1.30 cm in height. The total height of the separation column is 86.84 cm.

The carrier buffer is pumped with a gear pump, a Cole Parmer model A-74014-00, capable of a flow rate of 4.6 to 331 mL/min at a maximum pressure of 300 psi and maximum pressure differential of 75 psi. Two different syringe pumps are use to input the sample. The first, a Kd Scientific Model 100, is capable of 0.1 μL/hr to 426 mL/hr and can fit syringes from 10 μL to 60 mL. The second, a Harvard Apparatus PHD 2000, is capable of 0.1 nL/hr to 220 mL/min and can fit syringes from 0.5 μL to 140 mL. The power supply, a Sorensen DCS 33-333, can produce 0 to 33 V and 0 to 33 A. An inline degassing filter was provided by Allen Leduc of Minntech.

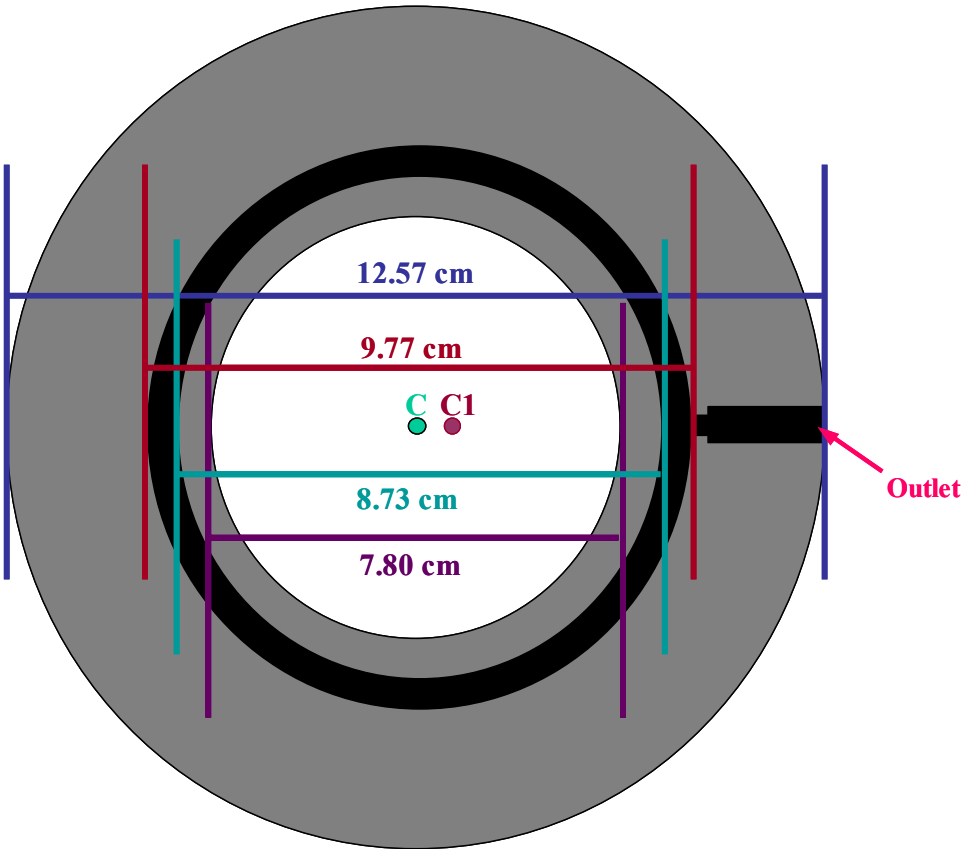

Figure 7.8 Diagram of the CFE ring including the channel and outlet. The channel is offset from the center of the ring (C) by 0.022 cm (C1).

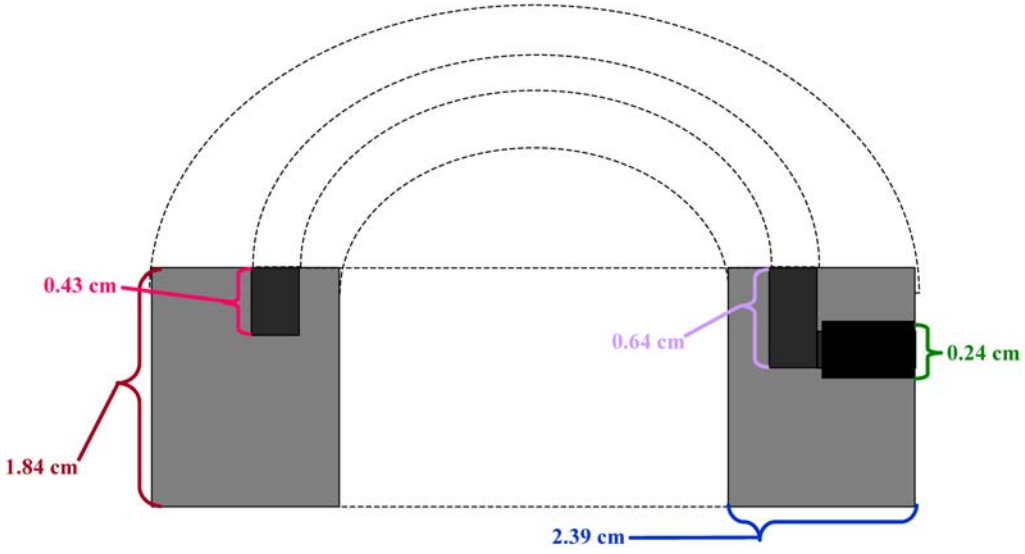

Figure 7.9 A side view of a CFE ring.

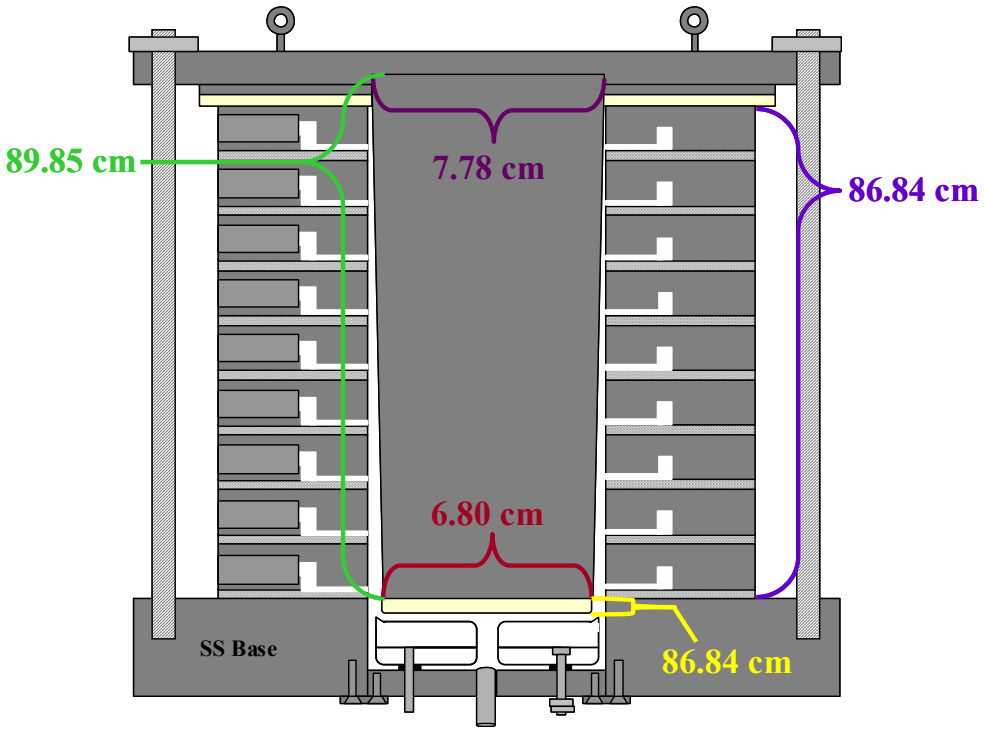

Figure 7.10 Dimensions of the separation column.

7.6 Unexpected Challenges

There have been several unexpected challenges to the operation of the novel CFE. During repeated flow tests, the ability of the gear pump to input the specified volume has declined. Initially the actual flow rate of the pump was almost 100% of the programmed flow rate. The final flow test resulted in a 50% or more drop in actual flow rate. For example, a programmed flow rate of 70 mL/min resulted in an actual flow rate of 35.8 mL/min. At lower programmed flow rates the difference was more profound where 35 mL/min resulted in an actual flow rate of 5.8 mL/min. In fact, the use of a programmed flow rate of 30 mL/min or less resulted in no flow. This decrease in flow rate is believed to be due to an overloading pressure on the system. A new pump must be purchased before the instrument can be used to fractionate MPCs. Additionally, an in-line pressure

gauge must be implemented with the new pump to ensure the system pressure does not exceed that of the pump.

It is important that the carrier buffer and sample be degassed in order for the gasses produced from the electrolysis of the buffer at the electrodes to be absorbed into the carrier buffer. An in-line degassing filter was placed between the pump and the instrument. A water aspirator vacuum was used to remove the dissolved gasses during operation. Mr. Leduc, who donated the in-line degassing filter, stated that the pressure on the filter should not exceed 35 psi and recommended the use of an oxygen sensor to determine the effectiveness of the filter. In order to ensure the pressure on the in-line filter not exceed 35 psi, an in-line pressure gauge must be implemented.

The flow tests were conducted at different flow rates and ratios of the flow separator. The flow tests resulted in the majority of the test solution exiting in outlets 1-5. At this point it is not clear whether the flow rate or the flow separator position dominates the position the test solution exits the column. In each of the flow tests, the flow separator was positioned with the larger portion of the carrier buffer flow above the separator. Additional tests with the flow separator at different positions, including with a larger portion of carrier buffer below the flow separator, are needed in order optimize the operation of the instrument.

The flow tests revealed some additional problems with the instrumental setup. It was found that it is essential that the sample and carrier buffer have a laminar flow, which is difficult given the current setup for the sample input. Initially, a Kd Scientific syringe pump capable of using syringes up to 60 mL in volume was used to input the sample. While the syringe pump can hold a 60 mL syringe, due to the pressure on the

syringe, the pump failed to hold the 50 mL syringe used during the flow tests. A Harvard Apparatus syringe pump was then borrowed to inject the sample. A better syringe pump capable of withstanding larger pressures must be purchased for the long-term use of the instrument.

The sample must be continuously injected for at least two column volumes before any fractions can be collected in order to allow the flow to stabilize. The volume of the sample is 1/48 that of the carrier buffer. The column volume is approximately 750 mL therefore, the sample volume is 31 mL for 2 column volumes. Previously, the syringe was refilled to allow for longer operation. This refilling caused a large flow distortion in the separation column in which the sample was recovered from all of the outlet ports. Additionally, the sample input during the first 2 column volumes and the filling of the instrument is lost, which could be costly. Presently, the carrier buffer is injected in place of the sample during the initial filling of the instrument. A syringe flow splitter is used to which from the carrier buffer to the actual sample. This flow splitter does not appreciably distort the flow if operated correctly. It is also important to change back to the carrier buffer after the complete injection of the sample in order to collect the entire separated sample.

The samples are collected above the instrument in 15 mL Falcon tubes in a standard test tube rack (48 tubes). With the present system, the outlet rack must be exchanged often. During one flow test, the outlet rack was exchanged 8 times or every 8 minutes. The flow rate for this test was only 35.8 mL/min. If the tubes were filled to capacity the tubes would have to be exchanged every 20 minutes. If faster flow rates are

to be employed a better outlet collection setup must be devised with the capability of holding larger volumes.

7.7 Conclusions

In conclusion, the novel CFE was designed and then constructed for the separation of additional varieties of MPCs. The instrument consists of an inverted annular separation chamber decreasing the effect of convection and gravity on the apparatus. The use of stainless steel to construct the instrument decreases the complexity and eliminates the need for a membrane separating the electrodes from the carrier buffer allowing the instrument to be employed to fractionate organic soluble MPCs unable to be fractionated by conventional CFE. The novel CFE requires optimization before it can be employed for the fractionation of MPCs.

BIBLIOGRAPHY

(1) Stix, G. *Sci. Am.* **2001**, *285*, 32-37.

(2) Jianrong, C.; Yuging, M.; Nongyue, H.; Xiaohua, W.; Sijiao, L. *Biotechnol. Adv.* **2004**, *22*, 505-518.

(3) Fortina, P.; Kircka, L. J.; Surrey, S.; Grodzinski, P. *Trends in Biotechnology* **2005**, *23*, 168-173.

(4) Alivisatos, A. P. *Sci. Am.* **2001**, *285*, 67-73.

(5) McCreery, R. *The Electrochemical Society Interface* **2004**, *Spring*, 25.

(6) Martin, C. R.; Baker, L. A. *Science* **2005**, *309*, 67-68.

(7) Whitesides, G. M.; Love, J. C. *Sci. Am.* **2001**, *285*, 39-47.

(8) Mijatovic, D.; Ekjkel, J. C. T.; van den Berg, A. *Lab Chip* **2005**, *5*, 492-500.

(9) Osaka, T. *The Chemical Record* **2004**, *4*, 346-362.

(10) Smorodin, T.; Beierlein, U.; Kotthaus, J. P. *Nanotechnology* **2005**, *16*, 1123-1125.

(11) Lieber, C. M. *Sci. Am.* **2001**, *285*, 59-64.

(12) Reed, M. A.; Tour, J. M. *Sci. Am.* **2000**, *282*, 28-37.

(13) Gubin, S. P.; Gulayev, Y. V.; Khomutov, G. B.; Kislov, V. V.; Kolesov, V. V.; Soldatov, E. S.; Sulaimankulov, K. S.; Trifonov, A. S. *Nanotechnology* **2002**, *13*, 185-194.

(14) Kuhr, W. G. *The Electrochemical Society Interface* **2004**, *Spring*, 34-38.

(15) Paul, S.; Pearson, C.; Molloy, A.; Cousins, M. A.; Green, M.; Kolliopoulou, S.; Dimitrakis, P.; Normand, P.; Tsoukalas, D.; Petty, M. C. *Nano Letters* **2003**, *3*, 533-536.

(16) Metzger, R. M. *The Electrochemical Society Interface* **2004**, *Spring*, 40-44.

(17) Lindsay, S. M. *The Electrochemical Society Interface* **2004**, *Spring*, 26-30.

(18) Burghard, M.; Fischer, C. M.; Roth, S.; Schlick, U.; Hanack, M. *Synth. Met.* **1996**, *76*, 241-244.

(19) Datta, S.; Tian, W.; Hong, S.; Reifenberger, R.; Henderson, J. I.; Kubiak, C. P. *Phys. Rev. Lett.* **1997**, *79*, 2530-2533.

(20) Wold, D. J.; Frisbie, C. D. *J. Am. Chem. Soc.* **2000**, *122*, 2970-2971.

(21) Dunlap, D. D.; Garcia, R.; Schabtach, E.; Bustamante, C. *Proc. Natl. Acad. Sci. USA* **1993**, *90*, 7652-7655.

(22) Porath, D.; Bezryadin, A.; de Vries, S.; Dekker, C. *Nature* **2000**, *403*, 635-638.

(23) Fink, H.-W.; Schonenberger, C. *Nature* **1999**, *398*, 407-410.

(24) Kasumov, A. Y.; Kociak, M.; Gueron, S.; Reulet, B.; Volkov, V. T.; Klinov, D. V.; Bouchiat, H. *Science* **2001**, *291*, 280-282.

(25) Park, H.; Lim, A. K. L.; Alivisatos, A. P.; Park, J.; McEuen, P. L. *Appl. Phys. Lett.* **1999**, *75*.

(26) McCreery, R. *The Electrochemical Society Interface* **2004**, *Spring*, 46-51.

(27) Alvarez, M. M.; Khoury, J. T.; Schaaff, T. G.; Shafigullin, M. N.; Vezmar, I.; Whetten, R. L. *J. Phys. Chem. B* **1997**, *101*, 3706-3712.

(28) Logunov, S. L.; Ahmadi, T. S.; El-Sayed, M. A.; Khoury, J. T.; Whetten, R. L. *J. Phys. Chem. B* **1997**, *101*, 3713-3719.

(29) Schaaff, T. G.; Shafigullin, M. N.; Khoury, J. T.; Vezmar, I.; Whetten, R. L.; Cullen, W. G.; First, P. N.; Gutierrez-Wing, C.; Ascensio, J.; Jose-Yacaman, M. J. *J. Phys. Chem. B* **1997**, *101*, 7885-7891.

(30) Brust, M.; Bethell, D.; Kelly, C. J.; Schiffrin, D. J. *Langmuir* **1998**, *14*, 5425-5429.

(31) Templeton, A. C.; Pietron, J. J.; Murray, R. W.; Mulvaney, P. *J. Phys. Chem. B* **2000**, *104*, 564-570.

(32) Templeton, A. C.; Wuelfing, W. P.; Murray, R. W. *Accounts Chem. Res.* **2000**, *33*, 27-36.

(33) Hostetler, M. J.; Wingate, J. E.; Zhong, C.-J.; Harris, J. E.; Vachet, R. W.; Clark, M. R.; Londono, J. D.; Green, S. J.; Stokes, J. J.; Wingnall, G. D.; Glish, G. L.; Porter, M. D.; Evans, N. D.; Murray, R. W. *Langmuir* **1998**, *14*, 17-30.

(34) Collier, C. P.; Shiang, R. J.; Henrichs, S. E.; Heath, J. R. *Science* **1997**, *277*, 1978-1995.

(35) Mayya, K. S.; Sastry, M. *Langmuir* **1998**, *14*, 74-78.

(36) Schon, G.; Simon, U. *Colloid Polym. Sci.* **1995**, *273*, 202-218.

(37) Zamborini, F. P.; Gross, S. M.; Murray, R. W. *Langmuir* **2001**, *17*, 481-488.

(38) Terrill, R. H.; Postlewaite, T. A.; Chen, C.-h.; Poon, C.-D.; Terzis, A.; Chen, A.; Hutchison, J. E.; Clark, M. R.; Wingnall, G.; Londono, J. D.; Superfine, R.; Falvo, M.; Jr., C. S. J.; Samulski, E. T.; Murray, R. W. *J. Am. Chem. Soc.* **1995**, *117*, 12537-12548.

(39) Wuelfing, W. P.; Green, S. J.; Pietron, J. J.; Cliffel, D. E.; Murray, R. W. *J. Am. Chem. Soc.* **2000**, *122*, 11465-11472.

(40) Zamborini, F. P.; Hicks, J. F.; Murray, R. W. *J. Am. Chem. Soc.* **2000**, *122*, 4514-4515.

(41) Ingram, R. S.; Hostetler, M. J.; Murray, R. W.; Schaaff, T. G.; Khoury, J. T.; Whetten, R. L.; Bigioni, T. P.; Guthrie, D. K.; First, P. N. *J. Am. Chem. Soc.* **1997**, *119*, 9279-9280.

(42) Templeton, A. C.; Cliffel, D. E.; Murray, R. W. *J. Am. Chem. Soc.* **1999**, *121*, 7081-7089.

(43) Hicks, J. F.; Templton, A. C.; Chen, S.; Sheran, K. M.; Jasti, R.; Murray, R. W.; Debord, J.; Schaaff, T. G.; Whetten, R. L. *Anal. Chem.* **1999**, *71*, 3703-3711.

(44) Green, S. J.; Stokes, J. J.; Hostetler, M. J.; Pietron, J. J.; Murray, R. W. *J. Phys. Chem. B* **1997**, *101*, 2663-2668.

(45) Chen, S.; Murray, R. W. *J. Phys. Chem. B* **1999**, *103*, 9996-10000.

(46) Chen, S.; Ingram, R. S.; Harris, J. E.; Pietron, J. J.; Murray, R. W.; Schaaff, T. G.; Khoury, J. T.; Alvarez, M. M.; Whetten, R. L. *Science* **1998**, *280*, 2098-9104.

(47) Brust, M.; Walker, M.; Bethell, D.; Schiffrin, D. J.; Whyman, R. *J. Chem. Soc., Chem. Comm.* **1994**, 801-802.

(48) Yee, C.; Scotti, M.; Ulman, A.; White, H.; Rafailovich, M.; Sokolov, J. *Langmuir* **1999**, *15*, 4314-4316.

(49) Brousseau, L. C.; Zhao, Q.; Shultz, D. A.; Feldheim, D. L. *J. Am. Chem. Soc.* **1998**, *120*, 7645-7646.

(50) Chen, S. *J. Phys. Chem. B* **2000**, *104*, 663-667.

(51) Chen, S. *J. Am. Chem. Soc.* **2000**, *122*, 7420-7421.

(52) Cliffel, D. E.; Zamborini, F. P.; Gross, S. M.; Murray, R. W. *Langmuir* **2000**, *16*, 9699-9702.

(53) Badia, A.; Gao, W.; Singh, S.; Demers, L.; Cuccia, L.; Reven, L. *Langmuir* **1996**, *12*, 1262-1269.

(54) Schmid, G. *Chemical Reviews* **1992**, *92*, 1709-1727.

(55) Chen, S.; Summers, J. M. *J. Phys. Chem. B* **2001**, *105*, 8816-8820.

(56) Eklund, S. E.; Cliffel, D. E. *Langmuir* **2004**, *20*, 6012-6018.

(57) Hostetler, M. J.; Zhong, C.-J.; Yen, B. K. H.; Anderegg, J.; Gross, S. M.; evans, N. D.; Porter, M.; Murray, R. W. *J. Am. Chem. Soc.* **1998**, *120*, 9396-9397.

(58) Templeton, A. C.; Chen, S.; Gross, S. M.; Murray, R. W. *Langmuir* **1999**, *15*, 66-76.

(59) Chen, S.; Murray, R. W. *Langmuir* **1999**, *15*, 682-689.

(60) Ingram, R. S.; Hostetler, M. J.; Murray, R. W. *J. Am. Chem. Soc.* **1997**, *119*, 9175-9178.

(61) Hostetler, M. J.; Templeton, A. C.; Murray, R. W. *Langmuir* **1999**, *15*, 3782-3789.

(62) Alivisatos, A. P. *Science* **1996**, *271*, 933-937.

(63) Hanna, A. E.; Tinkham, M. *Phys. Rev. B* **1991**, *44*, 5919-5922.

(64) Amman, M.; Wilkins, R.; Ben-Jacob, E.; Maker, P. D.; Jaklevic, R. C. *Phys. Rev. B* **1991**, *43*, 1146-1149.

(65) Wuelfing, W. P.; Murray, R. W. *J. Phys. Chem. B* **2002**, *106*, 3139-3145.

(66) Hicks, J. F.; Zamborini, F. P.; Osisek, A. J.; Murray, R. W. *J. Am. Chem. Soc.* **2001**, *123*, 7048-7053.

(67) Zamborini, F. P.; Leopold, M. C.; Hicks, J. F.; Kulesza, P. J.; Malik, M. A.; Murray, R. W. *J. Am. Chem. Soc.* **2002**, *124*, 8958-8964.

(68) Brennan, J. L.; Branham, M. R.; Hicks, J. F.; Osisek, A. J.; Donkers, R. L.; Georganopoulou, D. G.; Murray, R. W. *Anal. Chem.* **2004**, *76*, 5611-5619.

(69) Wang, W.; Lee, T.; Reed, M. A. *Reports on Progress in Physics* **2003**, *68*, 523-544.

(70) Reed, M. A.; Zhou, C.; Muller, C. J.; Burgin, T. P.; Tour, J. M. *Science* **1997**, *278*, 252-254.

(71) Chen, J.; Reed, M. A.; Rawlett, A. M.; Tour, J. M. *Science* **1999**, *286*, 1550-1552.

(72) Bigioni, T. P.; Harrell, L. E.; Cullen, W. G.; Guthrie, D. K.; Whetten, R. L.; First, P. N. *The European Physical Journal D* **1999**, *6*, 355-364.

(73) Bard, A. J.; Fan, F.-R. F.; Mirkin, M. V. In *Electroanalytical Chemistry: A Series of Advances*; Bard, A. J., Ed.; Marcel Dekker, Inc.: New York, 1994; Vol. 18, pp 243-373.

(74) Bard, A. J.; Fan, F.-R. F.; Kwak, J.; Lev, O. *Anal. Chem.* **1989**, *61*, 132-138.

(75) Bard, A. J.; Mirkin, M. V.; Unwin, P. R.; Wipf, D. O. *J. Phys. Chem. B* **1992**, *96*, 1861-1868.

(76) Liu, B.; Bard, A. J.; Mirkin, M. V.; Creager, S. E. *J. Am. Chem. Soc.* **2004**, *126*, 1485-1492.

(77) Liu, B.; Mirkin, M. V. *J. Am. Chem. Soc.* **1999**, *121*, 8352-8355.

(78) Zhang, Z.; Yuan, Y.; Sun, P.; Guo, J.; Shao, Y.; Girault, H. H. *J. Phys. Chem. B* **2002**, *106*, 6713-6717.

(79) Zhang, J.; Slevin, C. J.; Morton, C.; Scott, P.; Walton, D. J.; Unwin, P. R. *J. Phys. Chem. B* **2001**, *105*, 11120-11130.

(80) Tsionsky, M.; Bard, A. J.; Dini, D.; Decker, F. *Chem. Mater.* **1998**, *10*, 2120-2126.

(81) Pierce, D. T.; Unwin, P. R.; Bard, A. J. *Anal. Chem.* **1992**, *64*, 1795-1804.

(82) Selzer, Y.; YTuryan, I.; Mandler, D. *J. Phys. Chem. B* **1999**, *103*, 1509-1517.

(83) Quinn, B. M.; Liljeroth, P.; Kontturi, K. *J. Am. Chem. Soc.* **2002**, *124*, 12915-12921.

(84) Georganopoulou, D. G.; Mirkin, M. V.; Murray, R. W. *Nano Letters* **2004**, *4*, 1763-1767.

(85) Ding, Z.; Quinn, B. M.; Bard, A. J. *J. Phys. Chem. B* **2001**, *105*, 6367-6374.

(86) Macpherson, J. V.; Unwin, P. R. *J. Phys. Chem.* **1995**, *99*, 3338-3351.

(87) Selvin, C. J.; Ryley, S.; Walton, D. J.; Unwin, P. R. *Langmuir* **1998**, *14*, 5331-5334.

(88) Selvin, C. J.; Unwin, P. R. *J. Am. Chem. Soc.* **2000**, *122*, 2597-2602.

(89) Wilhelm, T.; Wittstock, G. *Electrochimica Acta* **2001**, *47*, 275-281.

(90) Nowall, W. B.; Dontha, N.; Kuhr, W. G. *Biosens. Bioelectron.* **1998**, *13*, 1237-1244.

(91) Niculescu, M.; Gaspar, S.; schulte, A.; Csoregi, E.; Schuhmann, W. *Biosens. Bioelectron.* **2004**, *19*, 1175-1184.

(92) Ciobanu, M.; Kincaid, H. A.; Jennings, G. K.; Cliffel, D. E. *Langmuir* **2005**, *21*, 692-698.

(93) Lister, T. E.; Pinhero, P. J. *Anal. Chem.* **2005**, *77*, 2601-2607.

(94) Mirkin, M. V.; Bard, A. J. *Analytical Chemistry* **1992**, *64*, 2293-2302.

(95) Williams, M. E.; Stevenson, K. J.; Massari, A. M.; Hupp, J. T. *Anal. Chem.* **2000**, *72*, 3122-3128.

(96) Pietron, J. J.; Hicks, J. F.; Murray, R. W. *J. Am. Chem. Soc.* **1999**, *121*, 5565-5570.

(97) Heath, J. R.; Knobler, C. M.; Leff, D. V. *J. Phys. Chem. B* **1997**, *101*, 189-197.

(98) Devenish, R. W.; Goulding, T.; Heaton, B. T.; Whyman, R. *J. Chem. Soc., Dalton Trans.* **1996**, *5*, 673-679.

(99) Schaaff, T. G.; Whetten, R. L. *J. Phys. Chem. B* **1999**, *103*, 9394-9396.

(100) Hicks, J. F.; Miles, D. T.; Murray, R. W. *J. Am. Chem. Soc.* **2002**, *124*, 13322-13328.

(101) Whetten, R. L.; Khoury, J. T.; Alvarez, M. M.; Murthy, S.; Vezmar, I.; Wang, Z. L.; Stephens, P. W.; Cleveland, C. L.; Luedtke, W. D.; Landman, U. *Adv. Mater.* **1996**, *8*, 428-433.

(102) Wilcoxon, J. P.; Martin, J. E.; Provencio, P. *Langmuir* **2000**, *16*, 9912-9920.

(103) Jimenez, V. L.; Leopold, M. C.; Mazzitelli, C.; Jorgenson, J. W.; Murray, R. W. *Anal. Chem.* **2003**, *75*, 199-206.

(104) Song, Y.; Jimenez, V.; McKinney, C.; Donkers, R.; Murray, R. W. *Anal. Chem.* **2003**, *75*, 5088-5096.

(105) Parak, W. J.; Pellegrino, T.; Micheel, C. M.; Gerion, D.; Williams, S. C.; Alivisatos, A. P. *Nano Letters* **2003**, *3*, 33-36.

(106) Brauer, G. *Handbook of Preparative Inorganic Chemistry*; 2 ed.; Academic Press: New York, 1963.

(107) Forouzan, F.; Bard, A. J.; Mirkin, M. V. *Israel J. Chem.* **1997**, *37*, 155-163.

(108) Tien, J.; Terfort, A.; Whitesides, G. M. *Langmuir* **1997**, *13*, 5349-5355.

(109) Fan, F.-R. F.; Demaile, C. In *Scanning Electrochemical Microscopy*; Bard, A. J., Mirkin, M. V., Eds.; Marcel Dekker: New York, 2001, p 75.

(110) Bard, A. J.; Faulkner, L. R. In *Electrochemical Methods: Fundamentals and Applications*; 2 ed.; John Wiley & Sons, INC.: New York, 2001, pp 569-571.

(111) Sandhyarani, N.; Resmi, M. R.; Unnikrishnan, R.; Vidyasagar, K.; Ma, S.; Antony, M. P.; Selvam, G. P.; Visalakshi, V.; Chandrakumar, N.; Pandian, K.; Tao, Y.-T.; Pradeep, T. *Chem. Mater.* **2000**, *12*, 104-113.

(112) Schaaff, T. G.; Shafigullin, M. N.; Khoury, J. T.; Vezmar, I.; Whetten, R. L. *Journal of Physical Chemistry B* **2001**, *105*, 8785-8796.

(113) Schaaff, T. G.; Knight, G.; Shafigullin, M. N.; Borkman, R. F.; Whetten, R. L. *J. Phys. Chem. B* **1998**, *102*, 10643-10645.

(114) Mulvaney, P. *Langmuir* **1996**, *12*, 788-800.

(115) Sandhyarani, N.; Pradeep, T. *Chem. Mater.* **2000**, *12*, 1755-1761.

(116) Spence, J. C. H. *High-Resolution Electron Microscopy*; Third ed.; University Press: Oxford, 2003.

(117) Schaaff, T. G.; Whetten, R. L. *J. Phys. Chem. B* **2000**, *104*, 2630-2641.

(118) Schoonveld, W. A.; Wildeman, J.; Fichou, D.; Bobbert, P. A.; van Wees, B. J.; Klapwijk *Nature* **2000**, *404*, 977-980.

(119) Hofstetter, W.; Zwerger, W. *Phys. Rev. Lett.* **1997**, *78*, 3737-3740.

(120) Weaver, M. J.; Gao, X. *J. Phys. Chem.* **1993**, *97*, 332-338.

(121) Chen, S.; Murray, R. W.; Feldberg, S. W. *J. Phys. Chem. B* **1998**, *102*, 9898-9907.

(122) McCreery, R. *Chem. Mater.* **2004**, *16*, 4477-4496.

(123) Kwak, J.; Bard, A. J. *Anal. Chem.* **1989**, *61*, 1221-1227.

(124) Amemiya, S.; Ding, Z.; Zhou, J.; Bard, A. J. *J. Electroanal. Chem.* **2000**, *483*, 7-17.

(125) Cliffel, D. E.; Bard, A. J. *Anal. Chem.* **1998**, *70*, 1993-1998.

(126) Wuelfing, W. P.; Templeton, A. C.; Hicks, J. F.; Murray, R. W. *Anal. Chem.* **1999**, *71*, 4069-4974.

(127) Creager, S.; Yu, C. J.; Bamdad, C.; O'Connor, S.; MacLean, T.; Lam, E.; Cong, Y.; Olsen, G. T.; Luo, J.; Cozin, M.; Kayyem, J. F. *J. Am. Chem. Soc.* **1999**, *121*, 1059-1064.

(128) Laibinis, P. E.; Whitesides, G. M.; Allara, D. L.; Tao, Y.-T.; Parikh, A. N.; Nuzzo, R. G. *J. Am. Chem. Soc.* **1991**, *113*, 7152-7167.

(129) Schreiber, F. *Prog. Surf. Sci.* **2000**, *65*, 151-256.

(130) Gerdon, A. E.; Wright, D. W.; Cliffel, D. E. *Biomacromolecules* **2005**, *ASAP*.

(131) Peterson, R. R.; Cliffel, D. E. *Anal. Chem.* **2005**, *77*, 4348-4353.

(132) Cliffel, D. E.; Amin, P.; Murray, R. W. *In progress for submission to Langmuir*.

(133) The kinetically limited electron rates were calculated using the equation IT(adj) = $[I_T((4D/(\pi a)) + k_{et})]/[(4D/(\pi a))I_T + k_{et}]$ which was derived previously by this researcher.

(134) McConnell, W. P.; Novak, J. P.; Brousseau, L. C.; Fuierer, R. R.; Tenent, R. C.; Feldheim, D. L. *J. Phys. Chem. B* **2000**, *104*, 8925-8930.

(135) Sengelov, H.; Borregaard, N. *J. Immunol. Methods* **1999**, *232*, 145-152.

(136) Mazereeuw, M.; Best, C. M. d.; Tjaden, U. R.; Irth, H.; Greef, J. v. d. *Anal. Chem.* **2000**, *72*, 3881-3886.

(137) Hoffman, P.; Ji, H.; Moritz, R. L.; Connolly, L. M.; Frecklington, D. F.; Layton, M. J.; Edds, J. S.; Simpson, R. J. *Proteomics* **2001**, *1*, 807-818.

(138) Richman, D. W.; McDonnell Douglas Corporation: United States, 1999.

(139) Lao, A. L. K.; Trau, D.; Hsing, I.-M. *Anal. Chem.* **2002**, *74*, 5364-5369.

(140) Roman, M. C.; Brown, P. R. *Anal. Chem.* **1994**, *66*, 86A-94A.